Sheffield Hallam University | Materials and Engineering Research Institute

FESTIVAL OF INNOVATION 2021

MERI Research Symposium Proceedings 2021

www.shu.ac.uk/meri

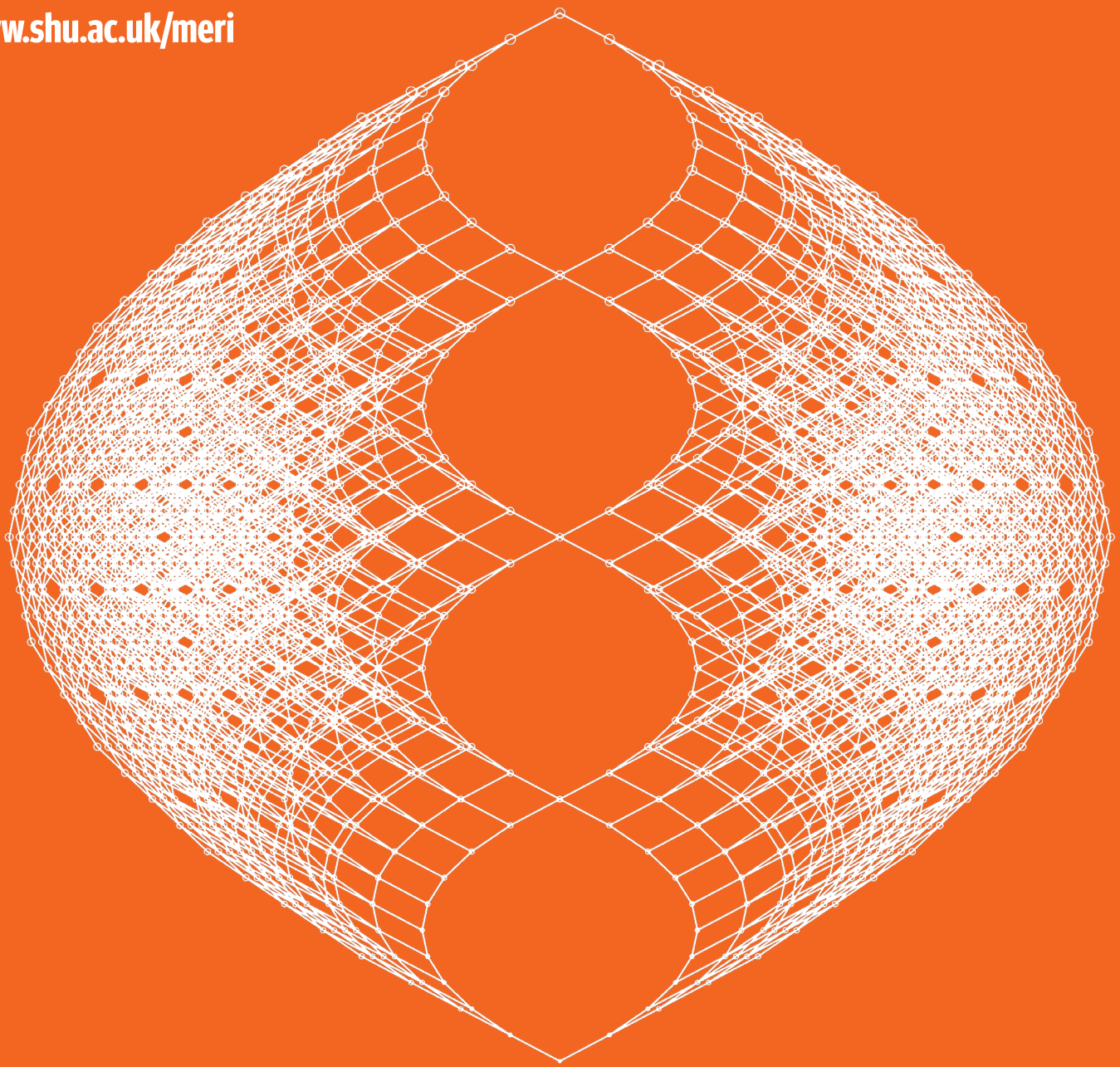

Welcome

It is with great pleasure that I welcome you to the 10th annual *Materials and Engineering Research Institute (MERI) Symposium*. This year our Symposium is a key event in the Festival of Innovation and we have opened up the Symposium to an external audience for the first time - so an especially warm welcome to friends, colleagues and new acquaintances from outside the University. I am confident you will find a vibrant programme and look forward to fruitful discussions during and following the event.

As a consequence of the cancellation of last year's event due to the pandemic, we have an especially strong and packed programme of oral and poster presentations this year, showcasing the diverse range of highly collaborative and multidisciplinary research undertaken by our talented staff and students within MERI, within the Department of Engineering and Mathematics, across the University and with external partners. You will see and hear how we are addressing genuine real-world issues of significance to enable MERI to deliver on the development needs of industries that rely upon materials and engineering. In doing this, our work promotes healthy, independent living and is developing technology platforms underpinning and enabling the economies of the future.

This year's inaugural Professorial lecture will be delivered by Antonio Feteira, Professor of Advanced Functional Materials. Explaining the importance of ceramics in the modern world, particularly in the field of electronic ceramics, Antonio will ask *What have ceramics ever done for us*?

As is customary, panels will judge the student poster and oral presentations and we will be presenting the Chris Breen memorial prize for the best student presentation.

On behalf of the MERI Symposium Organising Committee, I thank all contributors for their time in preparing, delivering and discussing the presentations of their recent work and wish you all an enjoyable and stimulating Symposium.

Professor Andrew Alderson
Director, Materials and Engineering Research Institute

Front page image: Mathematical object made as part of a spin-off algorithm designed by Ocean Wong (MERI PhD student).

Sheffield Hallam University | Materials and Engineering Research Institute

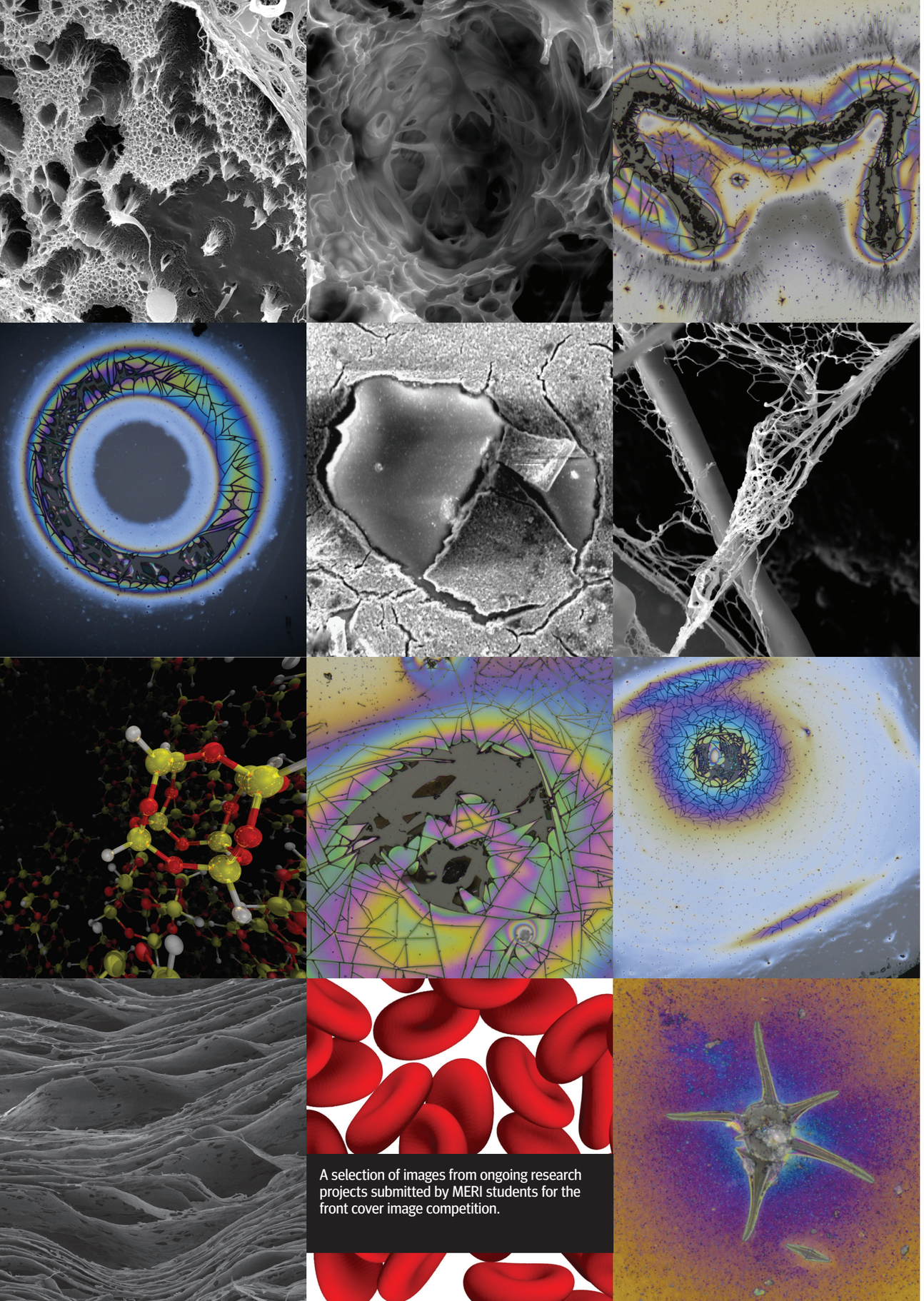

A selection of images from ongoing research projects submitted by MERI students for the front cover image competition.

Contents

A smart sleep apnoea detection service

Ragab Barika[1] , Alex Shenfield[1] , Hajar Razaghi[1] , Oliver Faust[1]

[1] Sheffield Hallam University, Sheffield, United Kingdom, S1 1WB, UK

Abstract

Over the last decades, sleep apnea has become a pressing healthcare problem. Diagnosis and treatment monitoring are key elements when it comes to addressing this public health crisis. Currently, both diagnosis and treatment monitoring are hampered by a chronic lack of specialized lab facilities which results in long waiting times or the absence of such services. This can delay appropriate treatment which might prolong living with sleep apnoea and thereby leading to health issues due to poor sleep. We address this problem with a smart sleep apnoea detection service based on Heart Rate Variably (HRV) analysis. The service incorporates Internet of Medical Things (IoMT), mobile technology (MT), and advanced Artificial Intelligence (AI). The measured signals are relayed by a smart phone into a cloud server via IoMT protocols. Once the data is stored in the cloud server, a deep learning (DL) algorithm is used to detect sleep apnoea events. Detecting these events can trigger a warning message which is sent to care givers. The smart sleep apnoea detection service is beneficial for patients who find it difficult to access specialized lab facilities for diagnosis or treatment monitoring.

Introduction

Sleep apnoea is a significant public health concern with an estimated 62.5% to 91.2% rise in global prevalence [1]. Both prevalence and incidence of sleep apnoea increases with age [2]. Recent US and European estimates show that approximately 14% to 49% of middle-aged people are affected by sleep apnoea [3]. In 2003, about 4% of the US population suffered from sleep apnoea. In 2008, the global prevalence was calculated to be at 6% [4] Demographics indicate that up to 24% of the adult population suffer from daily sleep problems [5]. Sleep apnoea is a kind of sleep disruption that can dramatically reduce quality of life [6]. The American Academy of Sleep Medicine (AASM) defines the condition as a delay in respiratory flow for more than 10s [7]. Haoyu et al., estimated that undiagnosed sleep apnoea costs the United States economy $70 billion in losses and $11.1 billion in damage, and leading to 980 deaths per year [8]. These figures suggest that sleep apnoea affects a large proportion of the population.

In the US, only 25% of sleep apnoea sufferers were aware of their condition [9] and 70% to 80% lacked a formal diagnosis [10]. Even if patients are aware of their condition, the waiting times for clinical tests range from 2 to 10 months in the UK to 7 to 60 months in the US [11]. The combination of high prevalence together with a low awareness and long waiting times suggests that current diagnostic procedures fail to protect patients [12]. A more effective system for diagnosis and treatment monitoring is required. Many physicians still diagnose sleep apnoea only by recording disruptive, noisy snoring [12]. The Polysomnography (PSG) method incorporates a wide range of measurements which reduces the subjectivity of the analysis [13]. However, PSG signals are acquired with heavy sensors and an expert technician must do the analysis, which is known as scoring [13]. PSG tools are expensive, with costs ranging up to 10,000 dollars [14]. With this paper we introduce a smart sleep apnoea detection service for sleep monitoring in the home environment.

The proposed service platform is illustrated in Figure 1. The smart sleep apnoea detection service can be conducted in the home setting with an electrode connected to the body during sleep.

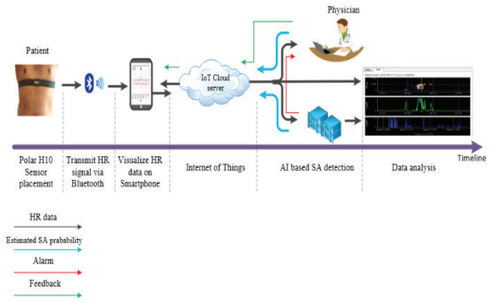

Figure 1 The diagnostic system architecture.

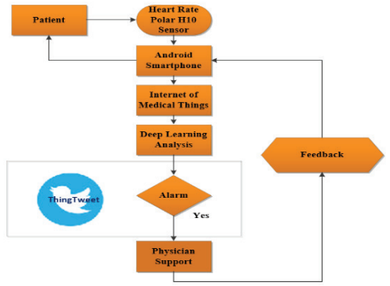

Figure 2 The Program flowchart service.

Method

In this paper, we propose a hybrid scheme for detecting sleep apnoea by combining a Polar H10 sensor with AI technology. The main goal of the smart apnoea detection service is to monitor sleep health in real time and report the results through a smartphone-based application. Figure 2 depicts the six implementation phases. The implementation incorporates IoMT, MT, and advanced AI. A DL algorithm is used for sleep apnoea detection. The measurement environment, which includes the Polar H10 sensor, is extended by the DL algorithm. The heart beats are picked up in real time using a Polar H10 sensor and the data is communicated via low power Bluetooth to a smart phone. The smart phone technology relays the data via WiFi to an IoT cloud server. Physicians will receive automatically generated alerts in the event of an emergency or if any abnormalities are discovered.

The Polar H10 sensor is a chest strap that is connected to the patient's body, as shown in Figure 3. The Polar H10 sensor has the following advantages: it is simple to use, lightweight, and there are no technical limitations to the observation time. Not only would such a scheme benefit the elderly and chronically ill, but it would also assist families in providing high-quality treatment.

Figure 3 The Polar H10 sensor is placed on the body.

Discussion

In this paper, we propose a cost-effective service framework that can be used to detect and monitor sleep apnoea in the home environment. The sleep apnoea detection service might even improve both diagnosis and treatment monitoring by extending the observation duration. Sleep disorders currently have distinct diagnosis and treatment tracking processes. Measurements taken in a clinical setting are used to diagnose sleep apnoea. As a result, if measurements are needed, the patient must travel to a clinic. These measurements are analysed by doctors to establish a diagnosis. For the patient, this procedure is inconvenient, and the cost is high. The proposed service platform incorporates a DL algorithm which can distinguish between disease and non-disease in real time. This study indicates that when applied to the diagnosis and monitoring of sleep apnoea cases, a state-of-the-art smart sleep service will attain expert human output. The most important contribution of the methods which underpin the apnoea detection service is the ability to generate an alarm message. This property is necessary if the doctors are to alert the patients and their relatives. Methods of monitoring and detecting sleep apnoea by incorporating an IoMT, MT and advanced AI tend to offer a scalable, efficient, and, at least potentially, better solution than most other methods of sleep apnoea recording. Besides, the combination of using an IoMT, MT and Advanced AI helps to improve detection performance and thereby reduce case risk. Such solutions may extend the independent life of individuals in their home environment and they may provide more protection.

Conclusions

Sleep apnoea affects a large portion of the world's population. Unfortunately, many people are not aware of its symptoms which extends the time needed for diagnosis and treatment. Developing high quality sleep apnoea equipment is critical because such equipment provides useful feedback to patients, clinicians, and researchers. We aim to improve existing technologies and create new wearable devices that provide valuable input and help sleepers to increase their sleep quality. The proposed smart sleep apnoea detection service translates laboratory sleep research findings into the patient's home environment. Through this paper, a new intelligent service is introduced which detects sleep apnoea automatically. This functionality has the potential to aide physicians during sleep apnoea diagnosis. The proposed service is based on a combination of IoMT, MT, and Advanced AI for detecting sleep apnoea. The service might also be useful in emergency situations because it can be tracked, registered, and processed in real time. This service allows the doctor to keep track of important parameters, such as the heart rate, while the patient is away from the hospital. If any parameter becomes abnormal, the machine can alert physicians and other caregivers.

References

1. J. K. Huhtakangas, J. Huhtakangas, R. Bloigu, and T. Saaresranta, "Unattended sleep study in screening for sleep apnea in the acute phase of ischemic stroke," *Sleep Med.*, vol. 65, pp. 121–126, 2020, doi: 10.1016/j.sleep.2019.08.002.
2. B. Mohit and E. M. Wickwire, "The Health Economics of Sleep Disorders Among Older Adults," *Curr. Sleep Med. Reports*, vol. 6(1), pp. 21–31, 2020.
3. F. Baty *et al.*, "Classification of sleep apnea severity by electrocardiogram monitoring using a novel wearable device," *Sensors (Switzerland)*, vol. 20, no. 1, pp. 1–12, 2020, doi: 10.3390/s20010286.
4. O. Faust, R. Barika, A. Shenfield, E. J. Ciaccio, and U. R. Acharya, "Accurate detection of sleep apnea with long short-term memory network based on RR interval signals," *Knowledge-Based Syst.*, vol. 212, no. xxxx, p. 106591, 2021, doi: 10.1016/j.knosys.2020.106591.
5. O. Faust, H. Razaghi, R. Barika, E. J. Ciaccio, and U. R. Acharya, "A review of automated sleep stage scoring based on physiological signals for the new millennia," *Comput. Methods Programs Biomed.*, vol. 176, pp. 81–91, 2019, doi: 10.1016/j.cmpb.2019.04.032.
6. S. Taran, "Sleep Apnea Detection Using Artificial Bee Colony Optimize Hermite Basis Functions for EEG Signals," *IEEE Trans. Instrum. Meas.*, vol. 69, no. 2, pp. 608–616, 2020.
7. S. S. Mostafa, F. Mendonça, A. G. Ravelo-García, and F. Morgado-Dias, "A systematic review of detecting sleep apnea using deep learning," *Sensors*, vol. 19, no. 22. MDPI AG, Nov. 02, 2019, doi: 10.3390/s19224934.
8. L. Haoyu, L. Jianxing, N. Arunkumar, A. Faeq, and M. Musa, "An IoMT cloud-based real time sleep apnea detection scheme by using the SpO2 estimation supported by heart rate variability," *Futur. Gener. Comput. Syst.*, vol. 98, pp. 69–77, 2019, doi: 10.1016/j.future.2018.12.001.
9. D. M. Bravata, N. Lightner, H. K. Y. Mph, and E. J. M. Edd, "Economic Assessment of 4 Approaches to the Diagnosis and Initial Treatment of Sleep Apnea," *Respir. Care*, pp. 50–61, 2018, doi: 10.4187/respcare.05355.
10. T. Van Steenkiste, W. Groenendaal, D. Deschrijver, and T. Dhaene, "Automated Sleep Apnea Detection in Raw Respiratory Signals Using Long Short-Term Memory Neural Networks," vol. 23, no. 6, pp. 2354–2364, 2019.
11. J. Lee, J. H. Choi, and S. Kim, "Prevalence and Characteristics of Subjects with Obstructive Sleep Apnea among Adults with Insomnia Disorder," *Sleep Med. Res.*, no. 10(2), pp. 108–112, 2019.
12. R. Jen *et al.*, "Accuracy of WatchPAT for the Diagnosis of Obstructive Sleep Apnea in Patients with Chronic Obstructive Pulmonary Disease," *J. Chronic Obstr. Pulm. Dis.*, vol. 2555, 2020, doi: 10.1080/15412555.2019.1707789.
13. V. Thorey, A. B. Hernandez, P. J. Arnal, and E. H. During, "AI vs Humans for the diagnosis of sleep apnea," *2019 41st Annu. Int. Conf. IEEE Eng. Med. Biol. Soc.*, pp. 1596–1600, 2019.
14. A. H. Yüzer, H. Sümbül, and K. Polat, "A Novel Wearable Real-Time Sleep Apnea Detection System Based on the Acceleration Sensor," *Irbm*, vol. 41, no. 1, pp. 39–47, 2020, doi: 10.1016/j.irbm.2019.10.007.

Investigation into the influence of Friction Stir Welding in thick section aluminium alloys

G. Brooks [a, b], S. Magowan [a], S. Cater [b], Q. Luo [a]

[a] Sheffield Hallam University, Sheffield, S1 1WB
[b] TWI Ltd, Wallis Way, Catcliffe, Rotherham, S60 5TZ

Abstract

Friction stir welding (FSW) is a solid state joining technology with a wide range of applications. However, there is a limited pool of published knowledge relating to the process variants that make FSW of thick section materials possible – a result of requiring specialist equipment to do so.

The primary aim of this project is to investigate the influence of three FSW techniques on weld quality when joining a range of 50mm thick aluminium alloys. Each has a different thermo-mechanical input and effect on the weld zone which has yet to be extensively investigated and quantified.

Introduction

Friction Stir Welding (FSW) is a solid-state joining process that in its simplest form, uses a non-consumable tool with a specially designed shoulder and probe to stir material softened by friction to form a joint [1], such as demonstrated in Figure 1.

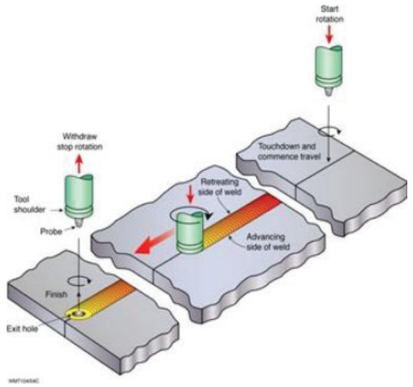

Figure 1 - Schematic of the FSW process [2].

The primary aim of the research project is to investigate the influence of welding variables on the microstructural and mechanical properties of welds created in 50mm thick aluminium and, thereby, enhance the technical and commercial benefits of the FSW process.

Experimental Method

Plates of 900x130x50mm AA5083-H111, AA6082-T651 and AA7050-T7451 were welded to the same grade of alloy by Weld-Flip-Weld (WFW-FSW) and Simultaneous Double Sided (SDS-FSW) and subsequently tested. The composition of the alloys is presented in Table 1. Further plates of 500x130x50mm were welded using Supported Stationary Shoulder (SSS-FSW). As this technique was untested in the thickness of material, investigation into tool life was first necessary. All welds were produced using the PowerStir™ available at TWI Ltd.

Wt. %	AA5083	AA6082	AA7050
Al	94.200	97.5	90.600
Cr	0.110	0.011	0.008
Cu	0.070	0.016	1.850
Fe	0.350	0.19	0.120
Mg	4.430	0.74	1.830
Mn	0.480	0.53	0.010
Other	0.028	0.076	0.04
Si	0.240	0.92	0.054
Ti	0.017	0.010	0.058
Zn	0.075	0.007	5.290
Zr	–	–	0.140

Table 1 - Composition of alloys.

Microstructural analysis of the material included Optical Emission Spectroscopy, Energy Dispersive X-Ray Spectroscopy (EDX) and Optical Light Spectroscopy (OLM). Mechanical testing focused on micro-hardness and tensile testing. In addition, energy input and swept volume of each weld were calculated.

Results and Discussion

Results for the WFW-FSW in AA7050-T7451 are presented in Figures 3-5. The weld was produced using traverse and spindle speeds of 130mm/min and 130rpm respectively. Figure 2 and Figure 3 show the macrograph and microstructure. Within the stir zone (Figure 3d, e & f) the grains are equiaxed and particles appear intergranular. Where the probes overlapped and produced a double processed region, e, the grains are much smaller. Whereas in the Heat Affected Zone (HAZ), the grain structure is bimodal and similar to that of the parent material.

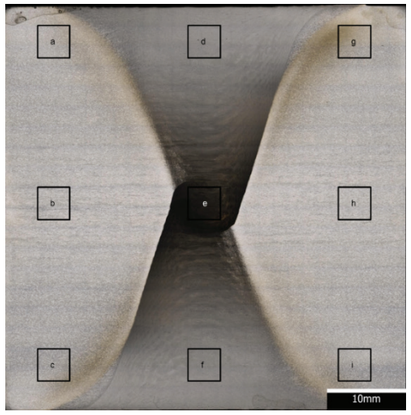

Figure 2 - Macrograph of G03/04 identifying regions of microstructural analysis.

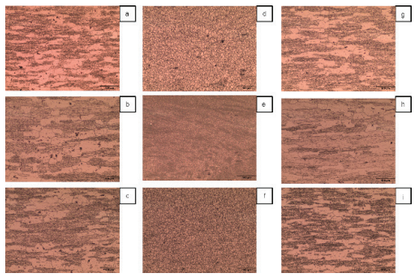

The hardness of the weld, shown in Figure 4, suggests that where the Thermo-Mechanical Affected Zone (TMAZ) meets the HAZ the material retains 55% of the hardness of the Parent material (PM). This relates to the larger grains shown in Figure 3, which were influenced by the heat from the weld. However in the stir zone there is a 70% retention in hardness compared to the PM. Although this region is hotter than the HAZ, the mechanical deformation of the grain structure by the rotating probes produces grains that are a factor of 10x small than the PM and equiaxed. This reduces the effect of the heat input by forming more grain boundaries for the dislocations to pass through.

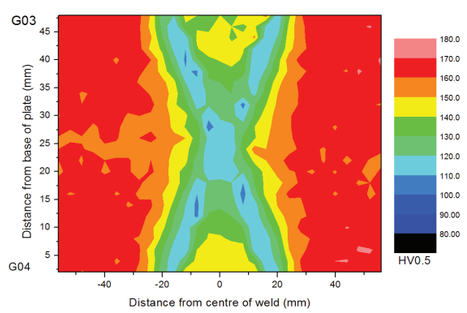

Figure 4 - Micro-hardness contour map of G03/04.

Conclusion

Welds have been produced using Friction Stir Welding (FSW) variants; WFW-FSW, SDS-FSW and SSS-FSW. The following observations have been made with regards to the microstructural and mechanical properties of the welded materials:

- Retention of ~70% hardness is observed in the stir zone but only 55% at the TMAZ/HAZ transition.
- The HAZ extends only 10mm wider than the shoulder of the tool in WFW.
- The macrograph of WFW-FSW shows a clear hourglass shape to the stir zone.

Future Work

Future work on this project will continue the investigation into the microstructure of the welded material by measuring average grain size and continuing EDX analysis.

References

[1] Mishra, Rajiv S, and M. Komarasamy. 2016. *Friction Stir Welding of High Strength 7XXX Aluminium Alloys.*

[2] S. Cater, D. Andrews, and TWI Ltd. 2014. *Fundamentals of Friction Stir Welding.*

Distributed Swarm Robot Formation

J. Chen [a,†], N. Lei [a], J. Penders [a], L. Alboul [a]

[a] Centre for Automation and Robotics Research, Sheffield Hallam University, Sheffield, S1 1WB

Abstract

This short paper presents some results related to multi-robot's formation patterns. Stability of the robots' formation and effectiveness of the program were tested using MATLAB to simulate the movement of the robots in the workspace. Meanwhile, a new control interface has been created to control the leader robots, and their current states have been displayed in the control interface.

Keywords—AI, simulation, control interface, swarm robotics.

Introduction

This work-in-progress paper describes some initial results of a research project that focuses on the collective decision-making of swarm robots during their interactions. Research on controlling robot swarms as well as multi-robot and mixed human-robot teams and interaction among the team agents has witnessed a significant progress in the last two decades [1]. A single robot is very limited in terms of information acquisition and complicated events processing, and these shortcomings will be highlighted in complex working environments. Therefore, researchers started organising multiple robots into groups, and the robots in the group (referred often as a team) have to communicate and cooperate with each other to perform tasks that a single robot cannot complete. Compared with a single robot, the importance of swarm robots is that they can interact and make collective decisions, thereby simplifying complex problems, saving working time, and improving work efficiency [2]. Different behaviours can emerge when the swarm operates because different swarm members are in different physical locations and potentially receive different inputs, so they have the characteristics of spatial distribution and functional distribution [3]. This means that the research of swarm robot systems is an inevitable trend in the development of robot technology, and it may bring epoch-making changes to the development of robot technology.

In real life, there are many jobs that are either directly or potentially dangerous; for example, jobs of traffic police, fire-fighters, industrial inspectors, etc. The events that they have to deal with, are relatively complex and generally require the cooperation of multiple people to complete [4]. If robots are used to perform the required tasks instead of humans, it is not only beneficial to avoid potential dangers, but also to ensure the accuracy and efficiency of the work. The purpose of this research project is to use swarm robots instead of humans to complete dangerous and complex tasks. There are many unpredictable obstacles and dangers in unknown environments. Robots can use cameras and sensors to better explore and understand the entire environment around them.

The development of swarm robots requires not only hardware technology but also software. Robots are devices that automatically execute programs set by humans. In order to plan and control the path of swarm robots, artificial potential field method is commonly used [5]. Although the research has not yet completed, some preliminary research results are described in the next section.

Experimental instruments and analysis

A. E-puck

This project uses e-puck robots as an experimental platform. E-puck's small size has the advantage of more flexible movements, and it is also equipped with a 640 x 480 pixel camera and 8 proximity sensors. Three microphones can be used to receive sound signals in the working space, and two DC stepper motors control the speed of the robot and make it reach the predetermined location accurately [6].

At the initial stages of our research, we simulate e-puck's functionalities, namely its capability to determine obstacles in front of it using proximity sensors, recognized colors by its camera and estimate distances.

B. Artificial Potential Field & Machine Vision

The artificial potential field method is based on 'the analogy of the magnetic field structure' in a potential field or on the analogy with the electrical charges concept [8] [9]. The workspace can be regarded as a potential field plane, in which the robot can be regarded as a positively charged point, and the target point is negatively charged. Like poles repel each other, whereas opposites attract, so the robot moves towards the target under the action of the resultant force of repulsion and gravitation while avoiding obstacles with positive charges [7].

MATLAB was chosen to study the formation of robots in a simulated environment. Multiple robots are scattered in the working space, which is flat and barrier-free. A maximum of 25 robots can be applied and are divided into five groups, each group has five robots, which are discretely distributed on site. Since the experimental results obtained by dividing 25 robots into 5 groups are clearer and less messy, the number of robots in the simulation is set to 25. Therefore, a group of robots is regarded as a moving obstacle for other groups of robots. Though the experiment uses 25 robots, the simulation environment allows application of a variable number of robots.

When robots are randomly placed in the field, the robots will be assembled according to their own attributes (different colours). This is the first part of the experimental test. The experimental steps are as follows.

Experimental steps

1. Place 25 robots randomly and arrange them into five groups according to colours.
2. Set one robot in a group as the primary robot, and the remaining four as secondary robots, which are moving towards the main robot to form a group.
3. Observe whether the obstacle avoidance function of the robot runs successfully according to the movement path of the robot.

The results of the simulation experiment are shown in Figure 1. The primary robot has been highlighted and circled to facilitate distinction from the other robots.

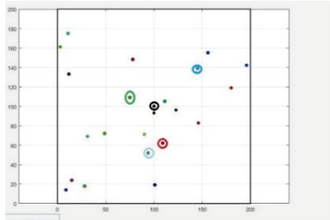

Figure 1 The layout of primary robots

Figure 2 shows the robots' paths and when the robot moves in an obstacle-free workspace, it will face different groups of robots (indicated here as black, red and green dots). When encountering other robots, the robot analyses the data obtained by the sensors and avoids other groups of robots to prevent collision. This experiment simulates the response when a robot encounters a randomly moving obstacle in an unknown environment, which is detected from the sensors surrounding the robot [6]. Regardless of the trajectory of the obstacle that moves randomly, the robot will move toward the target and avoid obstacles.

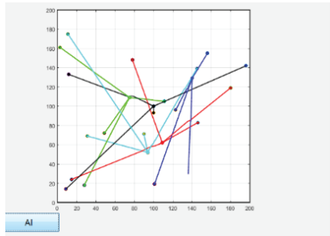

Figure 2 Robots' formation paths

Since the default setting of the first part of the experiment is an obstacle-free field, the second part of the experiment will randomly place obstacles to test the function of the robot.

In addition to signals obtained from proximity sensors, robots also use machine vision to distinguish the same or different groups of robots. As mentioned above, robots are divided into five groups, and the robots determine the groups according to the colours captured by the camera during the movement.

There are many restrictions on this method of identification. Due to factors such as the robot moving too fast and low camera resolution, most of the pictures captured by the camera are very blurry. Figure 3 shows two clearer pictures captured by the camera.

Figure 3 Pictures captured by the camera (colour blue & green)

C. Robot control interface

There exist many different types of robot controllers and control interfaces. In this project, a prototype of the related control interface was developed to monitor the current state of each robot in operation. Every robot usually responds to its own control interface uniquely, but this new robot control interface is designed to use only one interface to control multiple robots.

This control interface was originally used to monitor the position of the robot under simulated conditions. It allows to manually enter the desired number of simulated robots. The primary robot can be selected in the drop-down menu.

The working environment is a square of 200 x 200 units. The unit can be chosen by the user. In the next column under the robot selection, the coordinate data are displayed relevant to the current state of the selected robot and updated in real time. In the next two columns, the user can manually set the robot's running speed and control the selected robot to move. The robot can also operate according to the default optional formation shapes.

Result & Further work

The next step in the project will focus on implementing machine learning algorithms to a swarm of robots. Whilst machine learning has been successfully used for development of certain behaviours of a single robot, its application to a group of robots has been very scarce. This experiment tests the application of artificial potential fields and machine vision, and the experimental conditions are very limited. In a complex environment, the distribution of obstacles and robots will be more complicated. After the robots explore the entire space, they merge the environmental information they obtained through mutual communication between the robots to obtain more complete data. Machine learning can be applied to calculate faster and more convenient paths based on existing data. Incomplete information will cause many errors, so this is very important for swarm robots to make the next collective decision. At the same time, the control interface can also display the status of the robot in real time and can intervene and adjust the decision-making artificially if necessary.

References

[1] M. C. Gombolay, R. A. Gutierrez, S. G. Clarke, G. F. Sturla, and J. A. Shah, "Decision-making authority, team efficiency and human worker satisfaction in mixed human–robot teams," Autonomous robots, vol. 39, no. 3, pp. 293–312, 2015, doi: 10.1007/s10514-015-9457-9.

[2] Q. Tang, F. Yu, Z. Xu, and P. Eberhard, "Swarm Robots Search for Multiple Targets," IEEE access, vol. 8, pp. 92814–92826, 2020, doi: 10.1109/ACCESS.2020.2994151.

[3] H. Hamann, Swarm Robotics: A Formal Approach, 1st ed. 2018. Cham: Springer International Publishing, 2018.

[4] J. Saez-Pons, L. Alboul, J. Penders, and L. Nomdedeu, "Multi-robot team formation control in the GUARDIANS project," Industrial robot, vol. 37, no. 4, pp. 372–383, 2010, doi: 10.1108/01439911011044831.

[5] T. Zhang, Y. Zhu, and J. Song, "Real-time motion planning for mobile robots by means of artificial potential field method in unknown environment," Industrial Robot: An International Journal, vol. 37, no. 4, pp. 384–400, Jun. 2010, doi: 10.1108/01439911011044840.

[6] Mondada, Francesco, et al. "The e-puck, a robot designed for education in engineering." Proceeding of the 9th conference on antonomous robot systems and competitions. Vol. 1. No. CONF. IPCB: Instituto Politecnico de Castelo Branco, 2009: https://infoscience.epfl.ch/record/135236

[7] J. Yuan and H. Shen, "Research on Local Path Planning of Mobile Robot Based on Artificial Potential Field Method," Oct. 2019, pp. 785–789, doi: 10.1109/IMCEC46724.2019.8984146.

[8] B. Zhang, Y. Wang, X. Zhang, and B. Zhang, "Mobile Robot Path Planning Based on Artificial Potential Field Method," Applied Mechanics and Materials, vol. 577, no. Applied Decisions in Area of Mechanical Engineering and Industrial Manufacturing, pp. 350-353, Jul. 2014

[9] Y. Zhang and H. L, "Research on Mobile Robot Path Planning Based on Improved Artificial Potential Field," 2017, 3 Mathematical Models in Engineering 135

Investigation of erosion-corrosion performance of Tantalum (Ta) - Tungsten (W) material

J.S. Chouhan[a], B.D. Jana[b], Y.P. Purandare[a], P.Eh. Hovsepian[a], A. Dey[c]

[a] Materials and Engineering Research Institute, Sheffield Hallam University, Sheffield S1 1WB, United Kingdom
[b] Department of Engineering and Mathematics, Sheffield Hallam University, Sheffield S1 1WB, United Kingdom
[c] ISIS, STFC Rutherford Appleton Laboratory, Didcot OX11 0QX, United Kingdom

Abstract

In this study, the erosion-corrosion response of pure tantalum and tantalum-tungsten clad material will be investigated using both laboratory experiments and analytical modelling techniques. The work is of interest to Rutherford Appleton Laboratory (RAL), particularly with extending the life of their ISIS Ta-W spallation source (target) that experiences erosion-corrosion damage due to a flow of cooling water.

The work is currently at an early stage, and has completed pilot erosion experiments on pure aluminium samples and a preliminary study on pure tantalum samples. The pilot experiments identified a suitable method for measuring wear scar volume loss using stylus profilometry. The preliminary erosion studies on tantalum revealed erosion damage mechanisms with interesting features which are significantly different from those observed for pure aluminium.

Introduction

The erosion-corrosion phenomenon gained much interest in recent years with material loss in various flow handing industrial components such as pipes, pumps, impellers, and turbines [1]. Erosion-corrosion can be termed as a process of wear involving progressive loss of material due to combined processes of mechanical erosion and chemical corrosion. In erosion-corrosion, there is a complex interplay between erosion and corrosion which results in an additive effect when erosion enhances corrosion or a synergistic effect when corrosion enhances erosion [2][3].

Several studies in the past have reported various mechanisms of material removal, for solid particle erosion of both ductile and brittle materials. It is reported [4] that, irrespective of the shape and the size of the impacting abrasive (erodent) particles, the mechanism of material removal depends on the erodent impact angle. The reported mechanism of material removal at normal impact angles is plastic deformation [5] [6]. At oblique impact angles, based on particle shape, three different types of material removal mechanisms are reported [7]: these are Ploughing, Type I cutting, and Type II cutting. In brittle materials, the main mechanism of material removal is the propagation and intersection of cracks.

Currently, for Ta and Ta-W, no literature exists on the erosion/erosion-corrosion performance or its mechanisms of material removal. Some information is available on the corrosion of Tantalum [8] and Tungsten [9].

This Ph.D. study aims to identify the material loss mechanisms of erosion-corrosion of Ta-W materials using laboratory experiments and then establish an analytical model to predict the degradation rate. The research work is currently at an early stage and has completed pilot erosion experiments on pure aluminium samples and a preliminary study on pure tantalum samples. These results have been reported here.

Experimental Method

The slurry erosion experiments were performed using an Impinging Jet Aqueous Erosion Corrosion apparatus based in MERI. The rig is based on the design of an impinging slurry jet apparatus by Zu et.al. [10]. The rig has been modified to incorporate corrosion experiments. Initially pilot experiments were conducted on pure aluminium (30 mm diameter and 5 mm thickness) polished to 1-µm surface finish and was evaluated for erosive wear volume loss using impinging jet apparatus, IFM, and stylus profilometry to establish the methodology. In this volumetric evaluation, the sample wear scar (obtained after each erosion experiment using impinging jet apparatus) volumes were determined through exporting IFM/Profilometer data into excel, solving 4th order polynomial equations and integrating these equations to obtain scar areas and volumes subsequently.

Aluminium was chosen as it has been researched thoroughly, wherein the results from the literature could be used as a reference for cross-checking. The slurry impact angle was set at 45° and 90°, with constant velocity of 5 ms^{-1}. The slurry was composed of 9 wt.% SiC particles (9 wt.% particles to 91% solution) of size range 500-700 µm prepared in deionized water.

Following the pilot experiment, erosion experiments on as received tantalum sample (30 mm diameter and 5 mm thickness; polished to 0.02-µm surface finish) were performed using the Impinging Jet Aqueous Erosion Corrosion apparatus. These experiments were carried out in successive time intervals of 15 minutes for over an hour on the same sample spot at impact angles of 45° and 90° using SiC-deionized water slurry (9 wt.% SiC; 500-700 µm). In total 8 erosion experiments were conducted: 4 experiments, each of 15 minutes duration under impact angle of 45°; 4 experiments, each with duration of 15 minutes under impact angle of 90°. After each erosion interval of 15 minutes, the eroded surface was analyzed by scanning electron microscope (Quanta 650) to understand erosion mechanism. One experiment was carried out for an hour with only deionized water at 90° impact angle. These experiments were conducted to investigate the erosion behaviour of tantalum and the underlying material removal mechanism.

Results-Discussion

In the volumetric analysis of pilot erosion experiments (Aluminium samples), it is found that impinging jet apparatus determined volumetric loss for all wear scars is best matched with volumetric loss data determined through Profilometer (mean difference of 0.0331 mm^3) as compared to determined volume loss data through IFM (mean difference of 0.0372 mm^3). The results from the pilot erosion experiments on the aluminium sample showed higher erosion* (1.76 x 10^{-8} kgkg^{-1}) at oblique impact angle (i.e. at 45° angle) as compared to the erosion rate (0.51 x 10^{-8} kgkg^{-1}) at normal impact angle. The material removal mechanism as identified through the electron microscopy is shown in the SEM micrographs (Fig. 1). These findings correlated well with the experimental study in the literature [4][6].

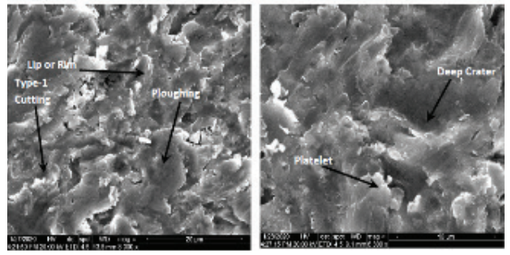

(a) (b)

Figure 1. SEM micrographs of aluminium eroded surface by 500-700 microns SiC slurry (5 ms^{-1}) at (a) 45° (b) 90° impact angle.

*Erosion unit kgkg-1 signifies ratio of mass loss rate of eroding material (Aluminium) to the mass flow rate of erodent (SiC)

In preliminary erosion experiments of tantalum sample, the average cumulative mass loss (0.0006 gm) was found to be higher under oblique impact (45°) as compared to the cumulative mass loss (0.0002 gm) obtained during normal impact (90°). The material removal mechanism at oblique impact angle (i.e. at 45°) consists of both cutting and plastic deformation as evidenced (Figures 1a and 2a) by lip or rim formation, angular (Type-1) cutting, and true machining without lip (ploughing). In contrast at normal impact, the material removal mechanism is plastic deformation only as evidenced (Figures 1b and 2b) by features such as formation of deep craters and platelets. Further scrutiny of the SEM micrographs (Fig. 2) reveals an abundance of porosity/dents on the wear scar surfaces of the Ta samples, which is unlike the Al sample (Fig. 1). This may be linked to how the Ta and Al samples were manufactured – the manufacturing route for Ta was powder metallurgy, whereas that for Al was melting and casting. A more detailed understanding of the erosion of Ta has been planned in this Ph.D. study.

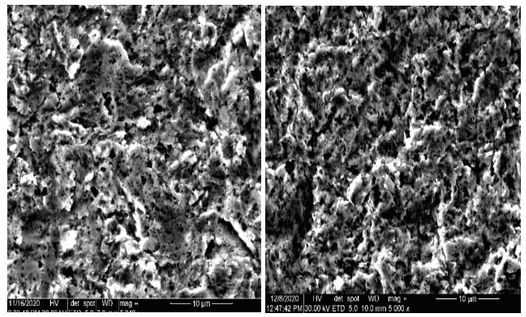

(a) (b)

Figure 2. SEM micrographs of eroded tantalum surface by 500-700 microns SiC slurry (5 ms^{-1}) with erosion on same spot in successive time intervals of 15 min. for 1 hr. at (a) 45° (b) 90° impact angle.

The impact on tantalum with only deionized water for over an hour did not result in any erosion or any changes to its surface features.

Conclusions

Based on the pilot erosion experiments of aluminium and the preliminary experimental investigation on tantalum, the following conclusions are drawn:

1. The pilot erosion experiments of aluminium samples identified a suitable method for measuring erosion volume loss through stylus profilometry (VeecoDektak 150).
2. The SEM micrographs (of both aluminium and tantalum samples) confirmed that the impinging jet aqueous erosion apparatus is operating successfully for the set conditions and delivering results which are consistent with the literature.
3. The preliminary experimental investigation of aqueous SiC slurry erosion on Tantalum sample does indicate ductile erosion behaviour with higher mass loss under oblique impact as compared to the mass loss under normal impact.

References

[1] G.T. Burstein, K. Sasaki, The birth of corrosion pits as stimulated by slurry erosion, Corros. Sci. 42 (2000) 841–860. https://doi.org/10.1016/S0010-938X(99)00100-6.

[2] M.M. Stack, B.D. Jana, S.M. Abdelrahman, Models and mechanisms of erosion-corrosion in metals, Tribocorrosion Passiv. Met. Coatings. (2011) 153–186. https://doi.org/10.1016/B978-1-84569-966-6.50006-3.

[3] M.M. Stack, S.M. Abdelrahman, B.D. Jana, A new methodology for modelling erosion-corrosion regimes on real surfaces: Gliding down the galvanic series for a range of metal-corrosion systems, Wear. 268 (2010) 533–542. https://doi.org/10.1016/j.wear.2009.09.013.

[4] I. Finnie, The mechanism of erosion of ductile metals, in: 3rd US Natl. Congr. Appl. Mech., ASME, 1958: pp. 527–532. https://doi.org/10.1016/0043-1648(60)90193-9.

[5] J.G.A. Bitter, a Study of Erosion Phenomena Part I, Wear. 6 (1963) 5–21.

[6] J.G.A. Bitter, A study of erosion phenomena. Part II, Wear. 6 (1963) 169–190. https://doi.org/10.1016/0043-1648(63)90073-5.

[7] Ian Hutchings and Philip Shipway, Tribology: Friction and Wear of Engineering Materials, 2nd ed., Elsevier Ltd., 2017. https://doi.org/10.1016/S0301-679X(98)00079-6.

[8] F.R. Attarzadeh, N. Attarzadeh, S. Vafaeian, A. Fattah-Alhosseini, Effect of pH on the Electrochemical Behavior of Tantalum in Borate Buffer Solutions, J. Mater. Eng. Perform. 25 (2016) 4199–4209. https://doi.org/10.1007/s11665-016-2295-x.

[9] M. Pourbaix, Atlas of Electrochemical Equilibria in Aqueous Solutions, Second, NACE, 1974. https://doi.org/10.1016/0022-0728(67)80059-7.

[10] J.B. Zu, I.M. Hutchings, G.T. Burstein, Design of a slurry erosion test rig, Wear. 140 (1990) 331–344. https://doi.org/10.1016/0043-1648(90)90093-P.

The characterisation, development and optimisation of peracid-based disinfectant formulations for infection control

J. Derham [a,†], F. Clegg [a], S. Turega [b]

[a] Materials and Engineering Research Institute, Sheffield Hallam University, Sheffield, S1 1WB
[b] Biomolecular Sciences Research Centre, Sheffield Hallam University, Sheffield, S1 1WB

Abstract

Utilisation of a high-level disinfectant, in healthcare sectors, is an essential asset for combating healthcare-associated infections (HAIs). For a disinfectant to be deemed 'high-level' it must be effective at killing a wide range of pathogenic microbes, peracetic acid (PAA) fulfils this role. Peracetic acid can be stored in two forms; a solution-based formulation, colloquially called 'pre-formed', or a solid form that is able to dissolve in aqueous solution whereby generating PAA in situ. The advantage of the latter form allows for safe and easy transportation and storage of the disinfectant. An additional advantage of PAA is that it degrades into environmentally friendly by-products; this unfortunately plays a role in the main drawback of PAA as a disinfectant because, it happens naturally and can only be slowed down. The stability of PAA is affected by pH and this is investigated herein. It is clear from this research that pH has an impact on the stability of PAA, with the highest level of protection at acidic pH values.

Introduction

'In the UK, ~300 000 patients a year contract healthcare associated infections (HAIs). In 2007, methicillin-resistant Staphylococcus aureus (MRSA) bloodstream and Clostridium difficile (C. diff) infections were classed as the underlying cause/ contributory factor in ~9000 deaths in England. The annual cost of HAIs to the NHS in the UK is ~£1 billion (£56 million of this is after the patients are discharged from hospital).' - National Institute for Health and Care Excellence (NICE), 2012.

'Annually it is estimated that, HAIs have a financial burden of €7 billion in Europe and $6.5 billion in the USA.' - World Health Organisation (WHO).

There is currently a need for a high-level disinfectant; that is effective against a wide spectrum of pathogenic microbes, whilst also requiring shorter contact times, to enable rapid turnover during cleaning procedures.

This research concentrates on peracid-based disinfectants; with a focus on peracetic acid (PAA). This biocidal agent can kill one of the main antagonists of the healthcare sector; C. difficile, this bacterium is able to form an endospore which provides a level of immunity against harsh conditions, many commonplace disinfectants included [1]. The efficacy of PAA is due to its innately high redox potential, 1.748 V in acidic medium. This aids PAA to have the added benefit of being efficacious at shorter contact times and lower concentrations than conventional chlorine based disinfectant products. This means it has the proclivity to 'rip' electrons from other compounds, whereby oxidising them and becoming reduced themselves as a result. The mode of action of peracids is thought to be through oxidative damage of different cellular components; such as cell membrane phospholipids (causing increased permeability, cell swelling and eventual cell rupture) and denaturing of proteins, through oxidising sulfhydryl and disulphide bonds [2,3].

(1) Spontaneous Decomposition:

$$CH_3CO_3H + CH_3CO_3 \rightarrow 2\ CH_3CO_2^- + O_2 + H^+$$

(2) Hydrolysis Decomposition:

$$CH_3CO_3H + H_2O \leftrightarrow CH_3CO_2H + HOOH$$

(3) Transition Metal Catalysed Decomposition:

$$CH_3CO_3H \xrightarrow{M^{n+}} CH_3CO_2H + \tfrac{1}{2}\ O_2$$

The reactions above outline an overview of the different decomposition pathways that PAA can take. With reactions (1) and (3) resulting in an overall, irreversible loss of PAA from solution and therefore having a direct effect on the efficacy [4,5,6].

Spontaneous Decomposition

The so-called spontaneous decomposition pathway detailed in Reaction (1) is reliant on the pH of the solution, where it is most prevalent at pH 8.2, which coincides with the pKa value of PAA. This is rationalised, because the reaction mechanism requires the presence of both peracetic acid and its conjugate base, the peracetate anion, to take place. To mitigate the effects of this decomposition pathway the formation can be buffered towards a pH < 8 [4,5,6].

Hydrolysis Decomposition

The main issue with PAA is that it undergoes hydrolysis reactions in acidic and alkali mediums. This reaction is analogous to the acid- and base-catalysed hydrolysis of esters. At acidic pH, the reaction can be reversible, whereas at alkali pH the reaction tends to be irreversible, this is a consequence of the pKa values of both acetic acid and peracetic acid [4,5,6].

Transition Metal Catalysed Decomposition

Transition metal ions that facilitate decomposition of PAA are iron, copper, cobalt, and manganese. Decomposition pathways can be circumvented through the introduction of a sequestrant, which negates their catalytic effect [4,5,6].

Aims and Objectives

The research being conducted has the goal of producing an easy-to-use disinfectant tablet formulation, which can be used to clean surfaces and reduce the risk of HAIs. The formulation is based on an already existing product, Peracide™, which has been developed and patented by a local Sheffield based company Sky Chemicals. This collaboration provides the opportunity to further the understanding of the chemistry which leads to the improves, the efficiency and practicality of the product.

Methodology

Twenty five hour kinetics profiles of; PAA and HOOH, are produced through a high throughput titration method, which utilises iodometry and cerimetry techniques.

Results and Discussion

To assess the influence of pH on the stability of PAA over 25 hrs, the buffer system presents in the original formulation used to create differing 'end' pH environments was adjusted. The chosen pH values were: 5, 6, 7, 7.5, 8.4, 9.7 and 10.5. To ensure that the addition of different amounts of adipic acid did not influence the maximum initial concentration of PAA formed, the acid was added in a delayed fashion after 30 minutes.

Figure 1 demonstrates the impact that pH has on the stability of PAA over 25 hrs. The general trend of the data seems to be that as the pH of the solution, moves away from the pKa value of PAA (negatively or positively), the more stable PAA becomes. This trend is more obviously shown in Figure 2; which divides the data into 3 categories: change in PAA concentration in blue, change in hydrogen peroxide concentration (analogous to decomposition of PAA by hydrolysis) in orange and spontaneous decomposition in grey.

Both Figures 1 and 2 also highlights that pH 10.5 can produce a relatively stable solution of PAA, this would make a convenient formulation, because the buffer system would no longer be required (reducing the cost of each disinfectant tablet).

The main highlight of the data is that, at pH 8.4 the stability of PAA is heavily impacted, with nearly a 50% decrease in the concentration. Coincidentally, this is the buffered pH of the Peracide™ formulation. The loss of PAA from solution is mainly attributed to the spontaneous decomposition reaction pathway; as highlighted in Figure 2.

Interestingly Figure 2 displays the trend (previously mentioned above) that links pH to the degree to which the spontaneous decomposition reaction of PAA occurs. The trend is such; as you approach the pKa value of PAA (which is 8.2) the spontaneous decomposition reaction becomes more prevalent, then as you exceed the pKa value the spontaneous decomposition reaction begins to lose its prevalence, with alkali hydrolysis becoming the more prominent cause for PAA loss.

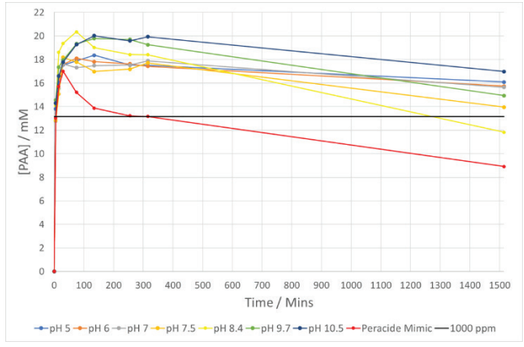

Figure 1: Kinetic profiles of peracetic acid, at different pH values, over a 25-hour period.

Figure 2: Concentration changes of peracetic acid, from the 5-hr interval and 25-hr, at different pH values.

Conclusions

There are two roles that pH plays in the formulation; firstly, a moderately alkali pH is required for the initial generation of PAA [4] and then secondly, a near neutral (7), acidic pH is more appropriate to increase the stability of PAA in solution and for reducing corrosiveness of the solution. The data gathered so far is of value because it allows for progression to be made on how to precisely improve the formulation, and thereby increasing the efficiency and practicality of a disinfectant product overall.

References

[1] Evaluation of the sporicidal activity of different chemical disinfectants used in hospitals against Clostridium difficile; S. Speight et al; 2011.

[2] Mode of action of hydrogen peroxide and other oxidizing agents: differences between liquid and gas forms; M. Finnigan et al; 2010.

[3] Mechanism of Sporicidal Activity for the Synergistic Combination of Peracetic Acid and Hydrogen Peroxide; M.J. Leggett et al; 2016.

[4] Kinetics and Mechanism of the Spontaneous Decompositions of Some Peroxoacids, Hydrogen Peroxide and f-Butyl Hydroperoxide; E. Koubek et al; 1963.

[5] Kinetics of Peracetic Acid Decomposition Part I & II: Spontaneous Decomposition at Typical Pulp Bleaching Conditions; Z. Yuan et al; 1997.

[6] Kinetics of the Hydrolysis and Perhydrolysis of Tetraacetylethylenediamine, a Peroxide Bleach Activator; M. Davies et al; 1991.

Structural changes in borosilicate glasses with varying Fe_2O_3 contents – a multi-spectroscopic approach

J. D. Eales [a,†], K. M. Fox [b], A. A. Kruger [c], A Goel [d], D. P. Guillen [e], J. S. McCloy [f], J. D. Vienna [g], S. Aminorroaya-Yamini [a], P. A. Bingham [a]

[a] Materials and Engineering Research Institute, Sheffield Hallam University, Sheffield, S1 1WB
[b] Savannah River National Laboratory, Savannah River Site, Aiken, SC 29808, USA
[c] Office of River Protection, Hanford Site, Richland, WA 99354, USA
[d] Department of Materials Science and Engineering, Rutgers, The State University of New Jersey, Piscataway, NJ 08854, USA
[e] Idaho National Laboratory, Idaho Falls, ID 83415, USA
[f] School of Mechanical and Materials Engineering, Washington State University, WA 99164-2920, USA
[g] Pacific Northwest National Laboratory, Richland, WA 99352, USA

Abstract

Two series of borosilicate glasses relevant to US radioactive waste vitrification were incrementally doped on a pro-rata basis with iron(III) oxide. Raman, Mössbauer, and X-ray absorption spectroscopies were carried out to investigate the changes in the glass structure as a function of nominal iron oxide concentration. Mössbauer spectroscopy showed that the iron exists as Fe^{3+} tetrahedral units, while Raman Difference Spectra (RDS) showed significant changes to both the borate and borosilicate ring structures. These changes were further investigated using boron K-edge X-ray Absorption - Near Edge Structure (XANES) which showed a gradual change to the [3]B/[4]B ratio as iron oxide concentrations increased.

Introduction

There is presently ~55M US gallons of radioactive waste stored in steel tanks at the Hanford site, USA [1]. This waste exists in mixed solid-liquid phases [2] and poses a massive environmental risk to the immediate area and nearby settlements. The US Dept. of Energy has proposed the waste be vitrified into borosilicate glass using “direct feed” vitrification to minimise further environmental risk [3]. A consequence of the “direct feed” approach, is that the final waste forms will be highly complex, and the effects of these complexities must be better understood prior to the commencement of the large-scale vitrification efforts. One such complexity is high concentrations of Fe within the waste. This is due to the various Pu and U extraction processes that used Fe-bearing chemicals as a reducing agent, as well as corrosion products from the degradation of the steel tanks [2]. The effects of high concentrations of Fe within borosilicate glasses have been researched extensively in the context of secondary phase stabilisation, particularly spinel and nepheline feldspar crystalline phases [4], as well in the context of chemical stability. The nature of how high Fe concentrations integrate within a borosilicate glass network, remains open for discussion. The impact on the structural, chemical, and thermal properties of the final glass form is largely dependent on the wider composition of the glass due its ability to act as both a glass network former and glass network modifier [5].

To investigate the structural impacts of high-Fe concentrations in borosilicate glass, a multi-spectroscopic approach is needed. Iron(III) oxide has been incrementally doped in a pro-rata basis into borosilicate glass series of increasing complexity. Series 1 (named the SCFe series) is a three-component sodium borosilicate, while series 2 (named the CCFe series) also contains lithium oxide, aluminium oxide, and calcium oxide to provide a closer approximation to real-world vitreous wasteforms.

Experimental Method

Sample Generation

The two compositions of borosilicate glass were derived from existing compositional data of glasses investigated at the Pacific Northwest National Laboratory and the Office of River Protection. The exact compositions can be seen in tables 1&2.

Sample ID	Nominal Oxide Composition(mol%)			
	SiO_2	B_2O_3	Na_2O	Fe_2O_3
SCFe000.0	55.81	16.28	27.91	0.0
SCFe000.1	55.76	16.26	27.88	0.1
SCFe000.2	55.70	16.25	27.85	0.2
SCFe000.5	55.53	16.20	27.77	0.5
SCFe001.0	55.26	16.12	27.63	1.0
SCFe002.0	54.70	15.95	27.35	2.0
SCFe003.0	54.14	15.79	27.07	3.0
SCFe004.0	53.58	15.63	26.79	4.0
SCFe005.0	53.02	15.47	26.51	5.0
SCFe007.5	51.63	15.06	25.81	7.5
SCFe010.0	50.23	14.65	25.12	10.0
SCFe014.0	48.00	14.00	24.00	14.0

Table 1 Nominal oxide composition in mol% of the 3-4 component glass composition

Sample ID	Nominal Oxide Composition(mol%)						
	SiO_2	B_2O_3	Na_2O	CaO	Li_2O	Al_2O_3	Fe_2O_3
CCFe000.0	44.12	12.84	22.01	5.36	8.23	7.45	0.0
CCFe001.0	43.68	12.71	21.79	5.30	8.15	7.37	1.0
CCFe003.0	42.79	12.45	21.35	5.20	7.99	7.22	3.0
CCFe005.0	41.91	12.20	20.91	5.09	7.82	7.07	5.0
CCFe007.5	40.81	11.86	20.36	4.96	7.62	6.89	7.5
CCFe010.0	39.71	11.55	19.81	4.82	7.41	6.70	10.0

Table 2 Nominal oxide composition in mol% of the 6-7 component glass composition.

The samples were melted in Pt/Rh crucibles for one hour at 1150°C, before being ground into a frit using a tungsten carbide mechanical mill. The frit was melted for a further hour at 1150°C before being poured and annealed at 470°C.

Raman Spectroscopy

For each sample made, a small bulk piece of glass was cut to 10 x 10 x 5 mm dimensions and polished using SiC paper of varying grades (P120 grade to P1200 grade) to achieve a flat and smooth surface for Raman Spectroscopy. The Raman spectra were acquired using a Thermo DXR2 Raman spectrometer with a 532 nm laser. A 600 lines/mm grated monochromator was used with a 50 µm slit with x10 magnification. The spectra were acquired across the full range of the spectrometer (50 – 3500 cm^{-1}) with 8 mW laser power, averaged over 200 exposures with an exposure time of 10 seconds.

Mössbauer Spectroscopy

Room-temperature ^{57}Fe Mössbauer spectroscopy was acquired relative to an α-Fe standard over a velocity range of ±4 mm s^{-1}. This was done over constant acceleration using gamma rays from a ^{57}Co source.

B K-edge XANES

Powdered glass samples were pressed into pellets of 200 mg, in which 20 mg of sample was mixed with 180 mg of cellulose acetate flux. These pellets were sent over to the BEAR beamline at the Elletra Synchrotron in Trieste, Italy. The samples were exposed to X-rays with an energy range of 175 – 220 eV with an energy step size of 0.1 eV under vacuum conditions to generate a spectrum across the boron K-edge (~195 eV). The detectors were calibrated using the C K-edge (285.2 eV) and the Al K-edge (1559.0 eV).

Results and Discussion

Raman Spectroscopy

All Raman spectra had a fluorescence correction applied using a polynomial correction patented to Thermo, while also being corrected for temperature and frequency dependant scattering using the Long Correction [6]. Each spectrum was normalised using the vector normalisation method before being plotted in a stack plot.

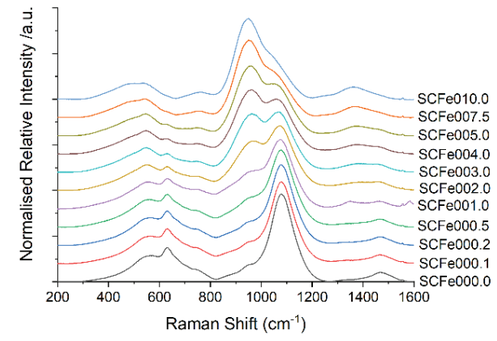

Figure 1 The Raman stack plot for the SCFe series.

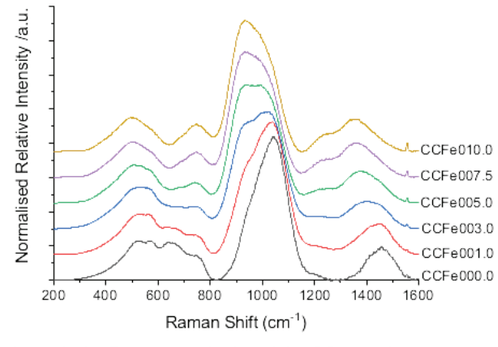

Figure 2 The Raman stack plot of the CCFe series.

Both the SCFe and CCFe spectra showed significant changes to the bands associated with borosilicate ring structures (~630 cm-1), the silicate tetrahedral stretching (800 – 1200 cm-1), and the mixed borate vibrations (1300 – 1600 cm-1) [7]. The band at 630 cm-1 decreases in both sets of spectra as the iron concentration increases, which suggests the borosilicate bonds within the samples are decreasing in concentration. The change in the mixed borate region suggests that there is change in the valency of the boron, with the boron going from B(IV) to B(III). These two changes are linked by the notion that boron in borosilicate structures, (for example, danburite crystals), typically exist as charge compensated B(IV) cation, with the charge compensated by group 1 alkali metal cations such as sodium.

Mössbauer Spectroscopy

The Mössbauer spectra showed that the iron exists predominantly as Fe(III) in predominantly 4-cooridnated structures. This coordination is typically associated with iron behaving as a glass network former. However, to exist in 4-coordinated structures with a valency of 3, the Fe cation must be charge compensated to remain charge neutral with the four oxygen anionsin the structure. Typically, this is provided by a single charged cation from the alkaline groups. In the case of the SCFe series, this would be provided by Na+ cations.

B K-edge XANES

The XANES spectra for both series showed the presence of both B(IV) and B(III) in all samples. However, as the concentrations of iron oxide increased, there appeared to be shift in the B(IV)/B(III) ratio towards the B(III) side. This appears to confirm the qualitative conclusions drawn from the Raman spectra. These trends, paired with the conclusions from Mössbauer spectra, would suggest that as the iron oxide concentrations increase, the sodium that would otherwise charge compensate the boron, is preferentially charge compensating the iron instead. This is leading to a breakdown of borosilicate bonds.

Conclusions

The combined spectroscopic data has provided key insights into how higher concentrations of iron oxide integrate within borosilicate glass. As the iron oxide concentration increases in both sample series, the borate groups within the glass undergo significant changes, which in turn, affects the borosilicate groups. It is suspected that the change is linked to the sodium potentially preferentially charge compensating the ferrate groups over the borate groups.

References

[1] R. E. Gephart, Phys. Chem. Earth **35**, 298-306 (2010)(DOI: 10.1016/j.pce.2010.03.032)

[2] R. A. Peterson, *et al*., Environ. Sci. Technol. **52**, 381-396 (2018)(DOI: 10.2021/acs.est.7b04077)

[3] J. D. Vienna, Int. J. Appl. Glass Sci. **1**, 309-321 (2010)(DOI: 10.1111/j.20411294.2010.00023.x)

[4] C. M. Jantzen & K. G. Brown, J. Am. Ceram. Soc. **90**, 1866-1879 (2007)(DOI: 10.1111/j.1551-2916.2006.01027.x)

[5] N. J. Cassingham *et al*., Eur. J. Glass Sci. Technol. A **49**, 21-26(2008)

[6] D. A. Long, *Raman Spectroscopy* (1970), McGraw-Hill.

[7] D. Manara *et al*., Am. Mineral., **94**, 777-784(2009)(DOI: 10.2138/am.2009.3027)

Molecular Dynamics Simulation of Organically Functionalised Nanoparticles Applicable to Polymer Nanocomposite Materials

J.K. Earnshaw [a,†], A. Hamilton [a], M. Krompiec [b], D. Cleaver [a]

[a] Materials and Engineering Research Institute, Sheffield Hallam University, Sheffield, S1 1WB
[b] Merck Group,

Abstract

Organically functionalised polyhedral oligomeric silsesquioxanes (POSS) are nanoparticles which offer a fascinating combination of organic and inorganic behaviours. POSS systems can exhibit a wide range of behaviours through variation of the geometry of their central inorganic cores and the choice of functional ligands. This makes them ideal candidates for achieving numerous thermomechanical, optical and barrier properties.

Here, we use molecular simulation to systematically examine POSS cubes with a range of ligands. From this, we identify the key molecular degrees of freedom which freeze in at Tg, thereby providing insight for synthetic control of this property. We also present steps towards more ambitious systems of functionalised POSS cubes incorporated into polymeric matrices.

Introduction

Polyhedral Oligomeric Silsesquioxanes (POSS) are nanoscale silica structures of chemical formula RSiO1.5 typically functionalised with a variety of organic 'R' moieties (Figure 1). The cubic conformation (T8) is the most widely studied species and is the focus of our work. POSS cubes may be synthesised with a wide range of and mixture of functional groups with different chemical properties, resulting in a rich chemistry. POSS molecules may be integrated into polymeric matrices to form nanocomposites through discrete molecular blending, pendant grafting or crosslinking. The organic-inorganic nature of this system has contributed to the development of materials with improved thermal and mechanical properties.[1,2]

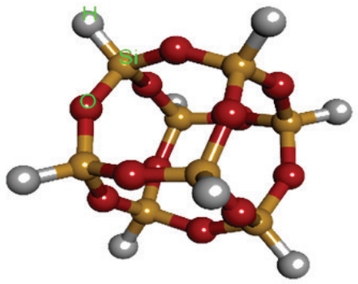

Figure 1 Illustration of cubic T8 POSS species with Hydrogen terminating functional groups.

Within this work, we utilise atomistic molecular dynamics (MD) simulations to investigate the molecular mechanisms by which the POSS species can contribute to and alter the macroscale properties of materials. In the first case we consider the efficacy of available force-fields for producing results that are representative of real-world POSS systems. Following this, we investigate the sensitivity of the simulated POSS systems to changes in the organic functional groups. Finally, we probe the effects of POSS nanoparticles when they are incorporated into polymer matrices.

Experimental Method

Simulations have been carried out using the MD package DL_POLY.[3] Molecular systems are first annealed at high temperatures before being passed to a cooling sequence of 10K intervals from 400 to 130 K in the Nose-Hoover Isothermal-Isobaric (npt) ensemble. Atomic charges are derived from the restrained electrostatic potential (RESP) method implemented in the software multiwfn.[4] Each interval has 500,000 timesteps of size 0.001 pico seconds, with approximately 30,000 atoms considered in each simulation.

Principally, the polymer consistent force-field (PCFF) has been used throughout this work.[5] for all intra and inter molecular interactions. Bond length (r) and angle (θ) fluctuations are thus contingent on harmonic bond potentials,

$$V_b(r) = \sum_{i=2}^{4} k_i^b (r - r_0)^i \qquad (1)$$

$$V_a(\theta) = \sum_{i=2}^{4} k_i^a (\theta - \theta_0)^i \qquad (2)$$

where r_0 and θ_0 are the equilibrium bond length and angle, respectively. The functional form used to describe the dihedral torsion (ϕ) potential is as follows,

$$V_t(\Phi) = \sum_{i=1}^{4} k_i^t (1 - \cos i\Phi) \qquad (3)$$

For equations 1-3, k represents the associated elastic constant for the given potential. Van der Waals nonbonded interactions are described through the Lennard-Jones 9-6 potential where ε is the potential well depth and σ represents the distance at which the energy is 0.

$$V_{VDW}(r_{ij}) = \varepsilon_{ij}\left[2\left(\frac{\sigma_{ij}}{r_{ij}}\right)^9 - 3\left(\frac{\sigma_{ij}}{r_{ij}}\right)^6\right] \qquad (4)$$

Coulombic interactions are determined from the Ewald approach.

Results and Discussion

Initially, we were concerned with ensuring our simulations were representative of real POSS systems. Cooling sequences of Octa-phenethyl POSS (OPEP) and Octa Vinyl POSS (OVP) (Figure 2) have been carried out as these systems have significantly different experimental glass transition temperature (Tg) values of 260 K and 401 K respectively. [6,7] We determine that PCFF outperforms Consistent Valent Force-Field (CVFF) for this purpose and that atomic charge consideration is crucial.

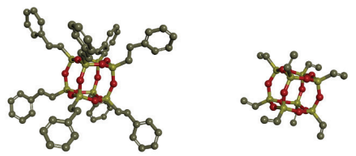

Figure 2 Schematics of OPEP and OVP respectively (Hydrogens have been omitted for clarity)

From radial distribution analysis (g(r)), we identified that the POSS molecules are conformationally locked, meaning movement of molecules ceases significantly above Tg. We then considered how the overall shapes of individual POSS molecules may change during simulation. By calculating the moment of inertia (MOI) tensor and plotting its standard deviation as a function of temperature, we have found that the POSS molecules exhibit a breathing mode of energy dissipation. Our simulations show that this breathing mode is arrested as the systems are cooled through Tg and, so, gives a specific molecular-level signature of the glass transition.

This type of analysis has then been systematically applied to methacrylate functionalised POSS systems with varying linker lengths (Figure 3). From Figure 4, we can see that, as this length is increased, Tg decreases linearly. This Figure also highlights that the molecular "breathing-mode" approach to identifying Tg has much less scatter than the traditional approach based on system-wide volume.

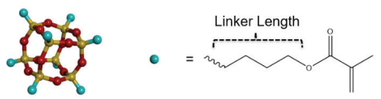

Figure 3 Structure of octa-functionalised methacrylate POSS. Butyl linker is shown and subject to change during separate simulations.

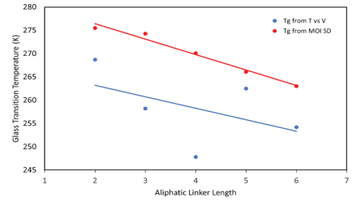

Figure 4 Reported Tgs from the moment of inertia (MOI(t)) and specific volume (V(t)) methods.

In recent work we have been interested in the effect of grafted POSS cubes on polymeric systems. In previous work, we have studied the Hydroxy-terminated polybutadiene (HTPB) polymer and identified that the dihedral rotational freedom of single C-C bond adjacent to trans C=C groups located within the backbone of these molecules is crucial for the expressed low Tg (191 K) within certain conformations.

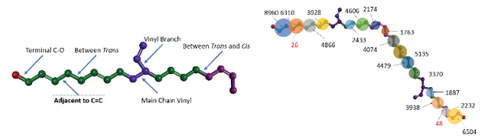

Figure 5 Depiction of HTPB repeat unit (Left) and illustration of the un HTPB molecule with a heat map of dihedral rotations.

We have grafted POSS cubes onto otherwise equivalent HTPB molecules and carried out analysis regarding dihedral rotation. From this, we identify that the POSS group acts as an effective anchor for this species and vastly decreases the freedom of this rotation, resulting in an increased predicted Tg of 262K. From Figure 6, we can specifically see that the grafting of the POSS groups dramatically reduces the number of dihedral rotations occurring during simulation.

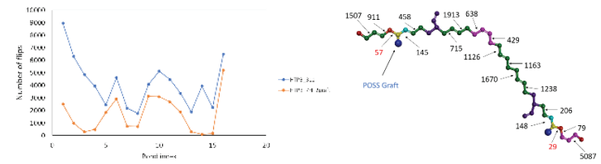

Figure 6 A graph to compare the number of flips for each dihedral on the HTPB backbone (Left) with a heat map (Right) displaying the locations of dihedral flips on the grafted HTPB.

Conclusions

We have identified important molecular-level features exhibited by POSS species both pure simulations and described their effect when bonded to a polymeric system. From this, we can rationalise the influence POSS systems on observed macroscale properties. We draw particular attention to the breathing mode of POSS nanoparticles as an important observable for identifying the macroscopic glass transition. In future work we plan to investigate the effects of asymmetric functionalisation on POSS systems and the behaviours of discrete mixed systems.

References

[1] A. Striolo, C. McCabe and P. T. Cummings, 'Thermodynamic and Transport Properties of Polyhedral Oligomeric Silsesquioxanes in Poly(dimethylsiloxane)', J. Phys. Chem. B, vol. 109, p. 14300, 2005.

[2] T. C Ionescu, F. Qi, C. McCabe, A. Striolo, J. Kieffer and P. T. Cummings, 'Evaluation of Force Fields for Molecular Simulation of Polyhedral Oligomeric Silsesquioxanes', J. Phys. Chem. B, Vol. 110, p. 2502-2510, 2006

[3] I. T. Todorov, W. Smith, K. Trachenko and M. T. Dove, 'DL_POLY_3: new dimensions in molecular dynamics simulation via massive parallelism', Journal of Materials Chemistry, vol. 16, p. 1911-1918, 2006

[4] L. Tian and C. Feiwu, 'Multiwfn: a Multifunctional Wavefunction Analyzer', J. Comput. Chem, vo. 33, p. 580-592, 2012

[5 H. Sun, S. J. Mumby, J. R. Maple, A. T. Hagler, 'An ab Initio CFF93 All-Atom Force Field for Polycarbonates' J. American Chemical Society, vol. 116, p. 2978-2987, 1994

[6] X. H. Yang, T. Giovenzana, B. Field, G. E. Jabbour, A. Sellinger, 'Solution processeable organic-inorganic hybrids based on pyrene functionalized mixed cubic silsesquioxanes as emitters in OLEDs', J. Mater. Chem, Vol 22, p. 12689-12694, 2012

[7] N. Hao, M. Bohning and A. Schonhals, ' Dielecctric Properties of Nanocomposites Based on Polystrene and Polyhedral Oligomeric Phenethyl-Silsesquioxane', Macromolecules, vol 40, p. 9672, 2007

Laser Beam Direct Energy Deposition – Effect of Process Parameters on Metallurgical and Mechanical Properties of Inconel 718

H. Elkington [a,†], S. Magowan [a], Q. Luo [a], C. Hauser [b]

[a] Materials and Engineering Research Institute, Sheffield Hallam University, Sheffield, S1 1WB
[b] TWI Technology Centre, Catcliffe, Rotherham, S60 5TZ

Abstract

Laser Beam Direct Energy Deposition (DED-LB) uses a laser as a heat source to create features or components from molten metal powder. Numerous process parameters are involved in DED-LB – including laser power, scan speed and powder feed rate. Complex relationships exist between these process parameters, ultimately dictating the properties of the deposited material. This work uses a Taguchi Design of Experiments to investigate laser power, scan speed and powder feed rate. Each combination of process parameters was used to build two sizes of samples. These were then subject to a range of metallurgical and mechanical testing. Samples were analysed in their as-deposited state. Analysis included Optical Light Microscopy, Scanning Electron Microscopy, tensile testing, and Vickers hardness and microhardness testing. Different results were obtained from the two sample sizes. The results indicate that the relationships which are present between the three process parameters should be considered when building components using DED-LB.

Introduction

Laser Beam Direct Energy Deposition (DED-LB) is an Additive Manufacturing (AM) process that utilises a laser to create a molten pool in a metallic substrate. An inert gas is used to blow metal powder into the melt pool via a nozzle [1]. Upon interaction with the laser beam the powder melts and binds to the substrate or previously deposited material. As the laser continues to move along its projected toolpath the deposited material cools and solidifies. Figure 1 shows a schematic of the DED-LB process.

Process parameters are variables which can be changed, altering the process. In DED-LB these include those related to the laser such as power, scan speed and laser profile, and others such as powder feed rate and gas flow rate. Due to the relationships between DED-LB process parameters and the properties of the deposited material, small variations to parameters can cause large changes to the microstructure and material properties [2].

Three key process parameters include laser power, scan speed and powder feed rate. These are defined as follows:

- Laser power (W) – the optical power output of a laser beam or average power of a pulsed or modulated laser.
- Scan speed (mm/s)– the speed at which the laser moves along the tool path.
- Powder feed rate (g/s) – the amount of powder per unit time exiting the nozzle.

These DED-LB process parameters have been identified to be key due to their significant effect on the heat input – a factor which is crucial to microstructure formation and thus final mechanical properties.

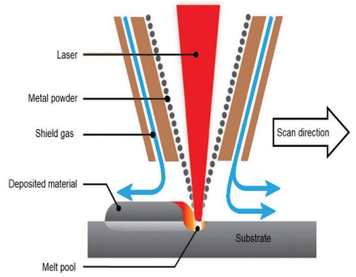

Figure 1 Schematic of the DED-LB process.

Experimental Method

A Trumpf DMD 505 system was used to manufacture samples using Inconel 718 powder (particle size 25-45 µm). Process parameters from previous work on this system were used to determine process parameter values, and the range examined for laser power, scan speed and powder feed rate.

A Taguchi Design of Experiments (DOE) using 3 levels of the 3 process parameters (LP, SS, PFR) was utilised. This generated 9 combinations of the process parameters. These were used to manufacture sample blocks of two sizes (large and small). The highest levels of each process parameter were also used to build a 10th set. Samples were analysed in their as-deposited state, using Optical Light Microscopy (OLM), Scanning Electron Microscopy (SEM), Vickers macro/microhardness, and tensile testing (larger block only).

Results and Discussion

Of the 9 Taguchi DOE generated process parameter combinations only 3 could be completed. Thus, despite choosing a range of process parameter values that have been used successfully previously, building all Taguchi DOE combinations was not feasible in practice. Therefore, the inputs are not appropriate for this Taguchi DOE approach. This suggests that this DOE approach may not be entirely suitable for the DED-LB process unless very narrow ranges of process parameter values are being investigated.

OLM found samples to be similar. Regions which had undergone re-melting as subsequent tracks and layers were deposited were clearly distinct. Heat-affected regions containing refined phases were noted. SEM observed 4 phases present in samples. This included a white globular phase, identified as Laves phase (Figure 2). This phase was greater in volume within the small blocks. Other phases included the γ-matrix, an unknown phase (pending further investigation) surrounding the Laves phase and Al-oxides.

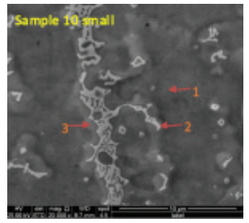

Element	wt. %
Ni	38.7
Nb	23.2
Cr	16.0
Fe	15.2
Ti	3.4
Mo	2.8
Ai	0.6

Figure 2 SEM image showing γ-matrix (1), Laves (2) and unknown phase (3).

Tensile specimens were taken in two orientations from the large blocks (horizontal and vertical). Horizontal and vertical tensile values differed significantly (Figure 3). This difference occurs due to the orientation of grains with regards to the tensile specimens – grains lie perpendicular to horizontal tensile specimens and parallel to vertical tensile specimens. No significant difference was observed between the process parameter combinations. All values were below the standard for untreated Inconel 718 [3]

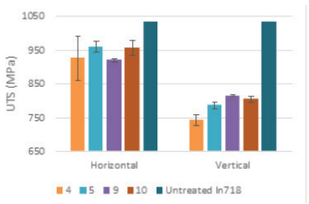

Figure 3 Ultimate Tensile Strength (UTS) values for tensile specimens machined from four of the built large blocks in two orientations. UTS standard untreated Inconel 718 is shown [3].

Macrohardness did not vary significantly in small or large blocks. Variation between small block microhardness was observed. No significant difference was present between large block microhardness. Vickers hardness were greater in small blocks when compared to large blocks, except for one set of process parameters (no. 5) whose small block value was akin to microhardness of large blocks (Figure 4).

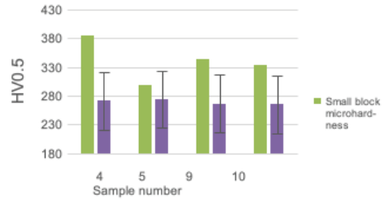

Figure 4 Microhardness values for small and large blocks. Standard deviation error bars are shown.

The increased volume of the white globular phase seen in small samples may be linked to their greater microhardness. Surrounding this phase is another unknown phase, this may also link to the greater microhardness observed. These phases are distributed heterogeneously throughout samples, caused by the variation in thermal cycling during the build. This heterogenous distribution may cause the difference between micro and macrohardness as the area tested in macrohardness is greater in size, hence the Inconel 718 matrix surrounding the white and unknown phase plays a greater role in affecting macro measurements.

These results show that the different combinations of process parameters result in property variation at a micro-scale in the small blocks. However, when looking at larger areas of a deposited part the differences decrease, and in the large blocks, differences are negligible. This indicates that the greater heat input during building the larger blocks, and the increased time that the larger blocks are at higher temperatures may deteriorate properties, causing them to decline until reaching a certain range of values (in this case for microhardness between 257 $HV_{0.5}$ to 287 $HV_{0.5}$).

Ongoing work is looking at the relationships between laser power, scan speed and powder feed rate, and how these process parameters can be linked mathematically. Other work has also been carried out during this research. This has included investigation into anisotropy within a single part, the effect of build direction with regards to the laser, and the impact of incorporating an interface into a DED-LB built part.

Conclusions

Differences between process parameter combinations were noted at a micro-scale in small blocks. No significant difference could be seen at a macro scale, or in large blocks. The interactions between laser power, scan speed and powder feed rate should be considered when determining what values to use for process parameters. The complex relationships between these mean that common DOE's may not be suitable for optimising the DED-LB process unless narrow parameter ranges are chosen. Identical process parameters for different geometries can result in significantly different properties, meaning process parameters are not interchangeable between geometries.

References

[1] Gu, D. (2015). Laser additive manufacturing of high-performance materials. Springer.

[2] Segerstark, A., Andersson, J., & Svensson, L. (2014). Review of laser deposited superalloys using powder as an additive. 8th International symposium on superalloy 718 and derivatives, 393-408.

[3] SAE International. (2016). Nickel Alloy, Corrosion and Heat Resistant, Sheet, Strip, and Plate, 52.5Ni - 19Cr - 3.0Mo - 5.1Cb (Nb) - 0.90Ti - 0.50Al - 18Fe, Consumable Electrode or Vacuum Induction Melted, 1950 °F (1066 °C) Solution Heat Treated AMS5597. Aerospace Material Specification.

Ultrasonic thermometer for measuring aggregate temperatures in dwellings.

A. Elyounsi [a], A. Holloway [a], A.N. Kalashnikov [a]

[a] Materials and Engineering Research Institute, Sheffield Hallam University, Sheffield, S1 1WB

Abstract

Temperature sensors are ubiquitous to science, medicine, industry and our daily lives. Conventional ones feature undesirable time lag and respond to temperature changes at a single localised point. Contrary to that, ultrasonic temperature sensors allow for responsive estimates and the temperature is sensed across the whole ultrasonic pathway. Ultrasonic Oscillating Temperature Sensors (UOTSes) produce sustained oscillations at a frequency that relates to the temperature of the medium between the transducers. This research aims to develop UOTSes operating in air at the distances of several meters, which will allow assessing aggregate temperature in dwellings (human habitable buildings) using a single sensor.

Introduction

Temperature sensors surround us in our life and their market share has been projected to reach £5.2 billion USD by 2022 [1]. These sensors found applications in science, medicine, and industry. For example, temperature measurements are crucial for ensuring safe and efficient operation of nuclear reactors and aircraft engines, for checking healthy state of different tissues of human body, for monitoring thermal change during chemical reactions, etc. There are various kinds of temperature sensors; among them infrared temperature sensors, resistance temperature detectors, thermistors, and thermocouples, are the most widely used.

Conventional temperature sensors have shown some shortcomings because of their operating principles. As they consist of an encased sensing element, they are only able to sense temperature at a single localised point and need to reach thermal equilibrium with the environment before taking any measurement. This results in an undesirable time lag when monitoring processes of interest. Therefore, several sensors need to be installed and interrogated if the average temperature needs to be monitored, as a result, their cost escalates very quickly with enhancing the accuracy. For example, control temperature at a comfortable level in a dwelling using conventional sensors this require for a network of sensors installed in several locations. The more accurate data to be collected the more expensive network to be installed and to maintained [2]. Additionally, conventional sensors feature typical settling time or response time in the range of several seconds, which limits their ability to respond to any sudden changes in the environmental temperature (e.g., opened window or door in a dwelling).

Ultrasonic thermometry is based on the relationship between the velocity of ultrasound and the properties of the medium, the most influential of which is the temperature. In turn, ultrasound velocity can be determined by conducting accurate measurement of the ultrasonic time-of-flight between two fixed points located at a known distance. Ultrasound waves are excited by applying an AC voltage to an ultrasonic transducer, typically made of piezoceramic material.

The waves either reach an ultrasonic receiver (this is called through transmission mode) or are reflected by an object which acoustic impedance substantially differs from that of the environment (the object is called a reflector). Before the reflected waves reach the transducer, it is switched to the receive mode to register the echo, saving on the separate receiver transducer (pulse-echo mode).

The aggregate temperature along its travel path could be then assessed from the obtained ultrasound velocity. Compared to conventional temperature sensors, ultrasonic temperature sensors (a) allow for responsive estimates and (b) the temperature is sensed across the whole ultrasonic pathway. Therefore, they can potentially replace several conventional sensors that may be difficult to place inside the object of interest (e.g., in the living area of a dwelling where temperature monitoring is required. However, ultrasonic sensors that measure the transit time (time of flight) directly can be quite expensive.

To minimise the high cost of existed ultrasonic instrumentation, the ultrasonic oscillating temperature sensors (UOTSes) were developed in our research group (Fig.1). An UOTS produces sustained oscillations at a frequency that relates to the temperature of the medium between the transducers (Fig.2 [3]). An UOTS requires a pair of ultrasonic transducers and driving electronics with supervisory control and output reporting [4] with the overall components cost below £20.

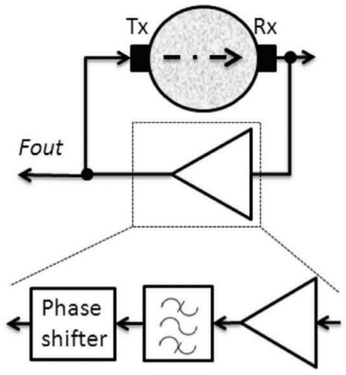

Figure 1 Operating principle of an UOTS that utilises positive feedback to produce sustained oscillations at the frequency that is related to temperature.

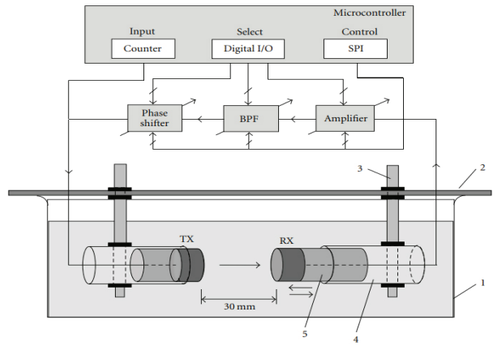

Figure 2 Block diagram of a complete UOTS, operated at the distance of ~30 mm in water (BPF – band pass filter, SPI – microcontroller's interface to adjust the parameters) [3].

Aim and objectives

This research aims to develop, fully prototype, and verify an ultrasonic sensor for measuring aggregate temperature in dwellings (human habitable buildings).

The aim is to be achieved by completing the following objectives.

1. Commissioning of a climate chamber that will enable keeping air temperature inside stable for the purposes of calibration and verification of the developed and industry standard temperature sensors.
2. Developing a test rig for the oscillating temperature sensors that can be isolated from any air movement inside the room to fully develop the electronics and characterise the sensor, equipped with calibrated conventional temperature sensors placed along the ultrasonic pathway;
3. Designing an electronic driver with MCU control and frequency reporting, and a suitable low-cost frequency reference oscillator based on a temperature compensated crystal oscillator (OCXO).
4. Verification of operation of the developed sensor against conventional temperature sensors.
5. Testing operation of the developed sensor for various real-world scenarios.

Progress to date

The progress was severely hindered by the very limited access to the lab since 18 March 2020 due to national, regional, and institutional restrictions.

Here is the list of accomplishment that relate to the research's objectives:

– A domestic chiller based on Peltier effect was acquired to be used as a controlled climate chamber (1);

– A low voltage safe to use power supply and transistor driver were acquired for controlling the box (1);

– Arduino PID control studied for the purpose to control the chamber (1);

– Several conventional temperature sensors were experimented with in order to provide feedback to the PID controller (1);

– Firmware was developed to use several conventional temperature sensors in groups in order to enable relating ultrasonic measurements to a temperature profile along the ultrasonic pathway (2);

– Suitable reference oscillators (Oven Controlled Crystal Oscillators – OCXOs), and temperature compensated crystal oscillators TCXO were identified and procured (3);

– C language & Arduino programming were learned for firmware development (3);

– Soldering of electronic components was learned (3);

– Literature review of previously developed UOTSes was completed (3).

Conclusions

It is expected that this research will result in

– Development of electronics, firmware, and mechanical settings to enable operation of UOTSes in air over distances of several meters.

– Development of novel temperature sensors for dwellings that will enable more economical heating or cooling of the latter.

– Reduce the cost of using of similar system in dwelling either using ultrasonic sensors or installation of network of conventional sensors.

– Improvement of the output reporting by using a web server that will enable reading the temperature of the dwelling over the internet.

References

[1] Temperature Sensors Market by Type (Bimetallic, Thermistor, IC, RTD, Thermocouple, IR, Fibre Optics, Others (MEMS, USB, Wi-Fi, ZigBee, Bluetooth, RFID)), End User (Process Industries & Discrete Industries), & Geography – Global Forecast to 2023, summary available online at : http://tinyurl.com/jrpj9dr (accessed May 2021).

[2] A. Afaneh, S. Alzebda, V. Ivchenko, and A. N. Kalashnikov, Ultrasonic Measurements of Temperature in Aqueous Solutions: Why and How, Physics Research International, Volume 2011, Article ID 156396, 10 pages. doi:10.1155/2011/156396.

[3] S. Alzebda, A. N. Kalashnikov, Ultrasonic Sensing of Temperature of Liquids Using Inexpensive Narrowband Piezoelectric Transducers, IEEE Trans. Ultrason., Ferroel., Freq. Control, vol.57, iss. 12, Dec 2010, pp. 2704- 2711.

[4] A. Hashmi, A.N. Kalashnikov, Sensor data fusion for responsive high-resolution ultrasonic temperature measurement using piezoelectric transducers, Ultrasonics, v.99, 2019, https://doi.org/10.1016/j.ultras.2019.105969 .

Tracking and Balancing Control of the LEGO Two-Wheel Robot with Extended Kalman Filter

S. Kokkrathoke [a], X. Xu [a]

[a] Materials and Engineering Research Institute, Sheffield Hallam University, Sheffield, S1 1WB

Abstract

This paper introduces a nonlinear freezing optimal control (NFOC) technique combined with an extended Kalman filter (EKF) for balancing a two-wheel robot (TWR) using the LEGO EV3 Robot as a prototype. Most traditional controllers are based on linear methods, which need to linearise the system around an operating point. This means that they can only operate in restricted ranges. In this research, the simulation results show the advantages of the stand-alone NFOC and the NFOC with EKF over the linear quadratic regulator (LQR) as they demonstrate wider operation ranges when starting from various ranges of initial pitch angles. In the case of implementation, the addition of EKF removes the signal drift problem in the gyro sensor and generate accurate measurements of the robot pitch angle. Furthermore, the tracking system design presents satisfactory results as the LEGO EV3 robot moves to the reference position while balancing itself.

Introduction

The Two-Wheel Robots (TWR) have been recognised as a benchmarking tool in various research to study and test control theory on underactuated systems. The design of TWR is based on the inverted pendulum on a cart introduced by Grasser and co-workers in [1]. They presented a mobile inverted pendulum robot known as JOE and the pole placement control was applied to balance the robot. More recently, several linear control techniques have been applied to the TWR, e.g., PID controller [2], Linear Quadratic Regulator (LQR) [3], fuzzy logic control [4]. However, these linear controllers [2]-[4] can only provide stabilisation of the TWR system within restricted operating ranges of pitch angles as the linearisation is applied around the equilibrium point when the TWR is in its upright position.

In this paper, a nonlinear control technique, namely, the Nonlinear Freezing Optimal Control (NFOC), is used to improve the operational range of stabilised TWR as the linearisation is not necessary, therefore the operating range of pitch angles is much wider. For instance, the implementation in [5] introduced the balancing of an inverted pendulum on a cart using the NFOC technique and showed excellent results. In this work, the NFOC designed in [6] is implemented using the prototype TWR - the LEGO Mindstorms EV3 robot. However, the LEGO EV3 gyro sensor has a "drift" problem due to noise corruption, resulting in an inaccurate pitch angle measurement during implementation. Hence, the extended Kalman filter (EKF) is utilised to remove the sensor's drifting issue by estimating the pitch angle state variable more accurately, for the NFOC to utilise for feedback.

Mathematical modelling

The system model of LEGO EV3 Robot is constructed from Fig.1, in a side view. The generalised coordinates of the TWR consist of wheel angle θ, robot pitch angle ψ, and robot yaw angle ϕ [3]. To establish the state-space model of the TWR, the Lagrangian technique is applied to analyse the system. Furthermore, a tracking system is designed to enhance the robot's ability of following setpoint changes by reducing steady-state errors in the horizontal displacement of the TWR, related to X_1. By doing this, the wheel angle X_1 is tracked by adding an integrator, which is presented as $X_5+=X_1$. Thus, the nonlinear state-space model of the TWR with tracking feature is written as [6]:

$$\begin{pmatrix}\dot{x}_1\\ \dot{x}_2\\ \dot{x}_3\\ \dot{x}_4\\ \dot{x}_5\end{pmatrix}=\begin{pmatrix}0 & 1 & 0 & 0\\ 0 & \frac{e_{m22}(x_3)}{a+b(x_3)} & \frac{e_{23}(x_3)}{[a+b(x_3)]x_3} & \frac{e_{m24}(x_3,x_4)}{a+b(x_3)}\\ 0 & 0 & 0 & 1\\ 0 & \frac{e_{m42}(x_3)}{a+b(x_3)} & \frac{e_{43}(x_3)}{[a+b(x_3)]x_3} & \frac{e_{m44}(x_3,x_4)}{a+b(x_3)}\\ 1 & 0 & 0 & 0\end{pmatrix}\times\begin{pmatrix}x_1\\ x_2\\ x_3\\ x_4\\ x_5\end{pmatrix}+\begin{pmatrix}0 & 0\\ \frac{f_{m21}(x_3)}{a+b(x_3)} & \frac{f_{m22}(x_3)}{a+b(x_3)}\\ 0 & 0\\ \frac{f_{m41}(x_3)}{a+b(x_3)} & \frac{f_{m42}(x_3)}{a+b(x_3)}\\ 0 & 0\end{pmatrix}\begin{pmatrix}v_1\\ v_2\end{pmatrix}. \quad (1)$$

where the generalised coordinates are defined as:

$X_1=\theta$, $X_2=\dot{\theta}\Rightarrow\dot{X}_2=\ddot{\theta}$, $X_3=\psi$, $X_4=\dot{\psi}\Rightarrow$, $X_4=\ddot{\psi}$.

Noticeably, the yaw angle is neglected in this research.

The V_1 and V_2 are left and right motor voltage and other parameters are defined as in [6]:

$X_1=\theta$ = Average wheel angle (rad), $X_2=\dot{X}_1$ = Average wheel velocity ¿¿

$X_3=\psi$= Body pitch angle (rad),$X_4=\dot{X}_3$ =¿ Body pitch angular velocity (rad ¿¿s) ¿

X5=integral of X1 (Tracking system),

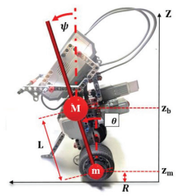

A Fig1. A Two-wheel robot created with LEGO EV3

Control Theory and Simulation Results

Simulation results of the LEGO EV3 robot are obtained using MATLAB as follows. The controllers are designed to stabilise the mathematical model of TWR from different initial pitch angles X_3. Therefore, the nonlinear system can be constructed in the form [7]:

$$\dot{X}=A(x)x+B(x)u(x), \quad (2)$$

where A is the matrix of system, B is the matrix of control, x is state variables vector, and u is control variables vector and the nonlinear feedback control equation is given by Riccati equation as:

$$u=-K_n(x)x=-R^{-1}(x)B^T(x)P(x)x, \quad (3)$$

where K is nonlinear feedback gain, R is weighting matrices, and the P(x) is an algebraic Riccati equation solution.

In case of linear method, the linear feedback control is presented by:

$$u=-K_l x=-R^{-1}B^T P x, \quad (4)$$

where K_l is linear feedback gain.

In this research, the power supply of LEGO EV3 is limited to 8.3 V. Therefore, this constraint is applied to restrict motor voltage in the MATLAB simulation at -8.3 V to 8.3 V. Hence, results of simulation in Fig. 2 indicate that the maximum initial pitch angle X_3 achieved by three controllers is the same: at 20.9° with this voltage constraint. Beyond this angle, the robot model will be unstable and topple over. Moreover, outputs of the three controllers resemble each other because the optimal feedback control gains K of the linear and nonlinear controls have only very minor differences at small pitch angles.

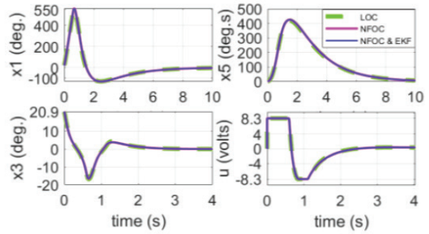

Fig. 2. Stabilisation of the TWR using LOC, NFOC and NFOC with EKF, with a voltage constraint 8.3V at the initial X_3 = 20.9°

It is possible to introduce higher initial pitch angles in the simulation, however, the TWR will demand higher power supply voltage from a high-performance motor. The Maxon motor series EC 45 Flat 30W [8] is selected which has a higher voltage at 36V and a nominal torque of 66 mNm. As a result, the voltage saturation in MATLAB simulation is raised to 36V from 8.3V and the motor torque parameter is also changed. It is clear from Fig. 3 that there are noticeable differences between linear and nonlinear control when the voltage constraint and motor are improved. The LOC presents significant oscillations when the X_3 reaches a new maximum at 60.7°; by contrast, the graphs of NFOC and NFOC with EKF (same as NFOC) are smoother with less oscillations.

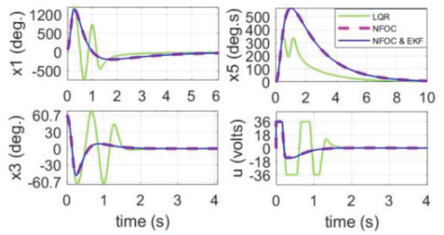

Fig.3. Stabilisation of the TWR using LOC, NFOC and NFOC with EKF, with a voltage constraint 36V of Maxon Motor EC45 Flat at the initial X_3 = 60.7°

Practical Results with EKF Embedded

Next, the three different control designs are implemented on a practical LEGO EV3 robot with limited motor voltage 8.3 V for investigation and analysis, and the drift problems from the gyro sensor will also be examined.

Firstly, the LOC is applied to stabilise the practical LEGO EV3 robot with the maximum initial pitch angle X_3=16°, shown in Fig.4. The state variables X_3, X_3 and X_5 demonstrate non-converging trends, caused by the gyro sensor drift problem.

Furthermore, the stand-alone NFOC and NFOC with EKF demonstrate similar maximum initial pitch angles at X_3=18°, both shown in Fig. 5. This represents a marginally more comprehensive operating range than the LOC as the matrix gain K_n of the nonlinear feedback controls varied depending on the varying state variables and provided more effective control, but the linear control gain K_l was fixed. Significantly, the gyro sensor problem has been solved by applying the EKF as the state variables X_3, X_3 and X_5 converge to their reference positions.

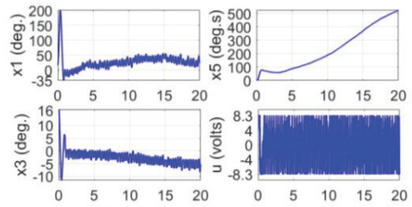

Fig.4. The maximum initial pitch angles of LOC technique at X_3 = 16°, implemented by LEGO EV3 robot

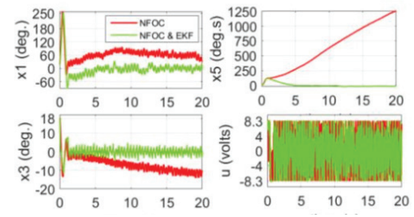

Fig.5. The stabilisation of LEGO EV3 robot at initial pitch angles X_3 = 18°, by NFOC technique and NFOC with EKF (sensor drift removed)

Conclusions and Future Work

In this research, the TWR was simulated and implemented using the NFOC technique with EKF, compared against the stand-alone NFOC and the LOC methods. Results of NFOC with EKF showed that the sensor drift problem was resolved, which the normal NFOC and LOC were unable to achieve. Furthermore, both nonlinear controllers satisfied the stabilisation requirement of the practical TWR, controlling it to stay in the vertical upright position, starting from different initial pitch angles. The nonlinear control methods presented slightly broader operational ranges than the linear controller when implemented using the Lego robot.

Future research will focus on the controllability of the nonlinear system, which depends on the non-unique forms of matrices A and B. Different state-space models from the same physical system will be investigated and analysed using NFOC and NFOC with EKF techniques.

References

[1] F. Grasser, A. D. Arrigo, S. Colombi, and A. . Rufer, "JOE: a mobile, inverted pendulum," IEEE transactions on industrial electronics, vol. 49, no. 1, pp. 107–114, Feb. 2002.

[2] J. K. Ahn and S. Jung, "Development of a two-wheel mobile manipulator: balancing and interaction control," Robotica, vol. 32, no. 7, pp. 1135–1152, January 2014.

[3] Y. Yamamoto, "NXTway-GS (Self-Balancing Two-Wheeled Robot) Controller Design)." Mathwork.com. https://www.mathworks.com/ matlabcentral/fileexchange/19147-nxtway-gs-self-balancing-two-wheeled-robot-controller-design (accessed Feb. 1, 2021).

[4] C. Tao, J. Taur, Tzuen Wuu Hsieh, and C. Tsai, "Design of a Fuzzy Controller With Fuzzy Swing-Up and Parallel Distributed Pole Assignment Schemes for an Inverted Pendulum and Cart System," IEEE transactions on control systems technology, vol. 16, no. 6, pp. 1277–1288, Noember 2008.

[5] X. Xu, H. Zhang, & G. Carbone. "Case studies on nonlinear control theory of the inverted pendulum," In Inverted pendulum: from theory to new innovations in control and robotics. O. Boubaker and R. Iriarte, eds. London, UK: IET, 2017, pp 225-262.

[6] S. Kokkrathoke, A. Rawsthorne, H. Zhang, and X. Xu, "Nonlinear Optimal Stabilising Control of a Two-wheel Robot," under review, International Journal of Modelling, Identification and Control.

[7] S. Banks, & K. Mhana, "Optimal control and stabilisation for nonlinear system," IMA Journal of Mathematical Control and Information, vol. 9, no. 2, pp 179-196, June 1992

[8] Maxon. "Maxon Product Page Range 2020/21."Online. flippingbook. com. https://online.flippingbook.com/view/1042987/285 (accessed Feb. 1, 2021).

Phase separation in sodium borosilicate glasses doped with phosphorus pentoxide (P_2O_5)

K. L. Skerratt-Love[1*], A.M.T. Bell [1], J. George [2], N. Canfield [2], C. Lonergan [2], D. Cutforth [2], A. Kruger [3], P.A. Bingham [1]

[1] Materials and Engineering Research Institute, Sheffield Hallam University, City Campus, Sheffield, South Yorkshire, S1 1WB, UK
[2] Pacific Northwest National Laboratory, PO BOX 999, Richland, WA 99352, USA
[3] Office of River Protection, 2440 Stevens Center Pl, Richland, WA, 99354, USA

Abstract

The aim of this work is to establish the on-set of phase separation in a sodium borosilicate glass system doped with phosphorus pentoxide (P_2O_5) and understand the mechanism by which it has occurred. It is also to understand the effects increasing P_2O_5 has on the structure of the glass and on its properties. A simplified form of borosilicate glass used internationally for radioactive waste vitirifcation is Na_2O – B_2O_3 – SiO_2, and this glass system was chosen to allow for the study of the effects of P_2O_5. The glass thus has the nomenclature of 'NBSP'. X-ray Diffraction (XRD) confirmed a solubility threshold of 4.0 mol% P_2O_5 with the onset of crystallinity by formation of $Na_3P_2O_5$ and $Na_4P_2O_7$. Through Field Emission Gun – Scanning Electron Microscopy (FEG-SEM), it was discovered that there were nucleation sites and evidence of phase separation, however, it was unclear what type of phase separation had occurred and by which mechanism it had arisen in each sample. Differential Thermal Analysis (DTA) and dilatometry were used to determine the midpoint glass transition temperature (T_g) of the samples, where it was found that P_2O_5 had a double effect of either increasing or decreasing the T_g, leading to either the de-polymerisation or re-polymerisation of the glass network. The Raman spectra showed that the increase in the P_2O_5 content resulted in key intensities at 731 cm^{-1}, 936 cm^{-1}, 987 cm^{-1}, 1011 cm^{-1}, 1028 cm^{-1} and 1162 cm^{-1} which were associated with phosphate species. Ultimately, increasing the P_2O_5 content has induced phase separation in the glass system and has caused structural changes, whose effect can be seen in the T_g.

Introduction

Phosphorus pentoxide (P_2O_5) can be a problematic component and is found in the Hanford site defence radioactive wastes that are to be converted to vitrified waste forms. The P_2O_5 in the vitrified waste originates from the Bismuth Phosphate, REDOX (Reduction-Oxidation) and PUREX (plutonium uranium reduction extraction) processes used for plutonium extraction from irradiated uranium [1]. P_2O_5 can be problematic because it is poorly soluble in borosilicate glass systems, with concentrations >4.5 wt% potentially leading to phase separation: this can negatively affect melt viscosity and chemical durability [2]. In some Hanford waste glasses, P_2O_5 will be present at levels that can impact the melter performance and glass properties. Phase separation can be undesirable because it can lead to phases with different chemical and mechanical properties, which may increase the leachability of radionuclides incorporated in the waste glass, and hence reduce the integrity of the glass. Phase separation in glasses is a process where a single-phase system separates into a multi-phase system and is a phenomenon that can arise in many liquid systems and metals [3], [4]. There are two mechanisms by which Phase separation can occur in a glass melt: (i) spinodal decomposition and (ii) nucleation and growth. In alkali and alkaline earth silicate glasses, phosphate units do not fully incorporate into the silicate network, but instead form phosphate-rich regions with low degrees of connectivity, forming orthophosphate (PO_4^{3-}) and pyrophosphate ($P_2O_7^{4-}$) units [5]. P^{5+} has a strong ability to scavenge charge-balancing modifier cations from the silicate network, which increases the degree of silicate network polymerisation [6]. In borate and silicate glass systems the extent of miscibility gaps can be influenced by glass modifiers and can be seen as their polarising power [7]. In general, the greater the polarising power of the metal cation the stronger the attraction between it and non-bridging oxygens (NBOs), and hence the greater the tendency towards clustering of these particles and the occurrence of phase separation [7].

Experimental Method

100 g batches of the NBSP glasses were prepared by using the melting-annealing method using the precursors of SiO_2, Na_2CO_3, H_3BO_3 and $NH_4H_2PO_4$. The mixture was milled before being melted in a Pt-Rh crucible. The crucible was heated to 1150°C for one hour, before being poured into a pre-heated steel mould forming a monolith. The monolith was then annealed at 500°C for one hour with a cooling rate of 1°C/min to 25°C. X-ray diffraction patterns were recorded for the glasses using a CμKα radiation on a Bruker D8 Advance with a scan rate of 0.015° 2θ with a step size of 0.015°, a scan step size of 177 seconds, and were measured between 5° and 70° 2θ. Scanning Electron Microscopy (SEM) images and Electron Dispersion X-ray Spectroscopy (EDS) mapping were achieved using a JOEL JSM-Field emission SEM with JOEL PC-SEM v.2.1.0.9 software to drive the microscope and image the samples. The samples were covered in 2 nm of Iridum because the samples were non-conductive. For Tg, DTA and dilatometry were used to heat the sample up to 625°C and 800°C at a rate of 10°C/min, respectively. An SDT Q600 V20.9 build 20 and NETZSCH DIL 402SE were used. Raman spectroscopy was conducted on a Thermo DXR2 Raman spectrometer with a wavelength of 532nm. The samples had an exposure of 15 seconds at 200 accumulations with a laser of 10mW using a 50μm slit and a magnification of 10x. The samples had readings taken at three different locations so that an average reading could be calculated. The spectra were then corrected for temperature and excitation line effects using the long correction by Neuville and Mysen [8].

Results and Discussion

XRD patterns showed that NBSP0.0 to 3.0 were amorphous with no measurable crystallinity, whilst samples NBSP4.0 to 6.0 had measurable peaks with identifiable crystalline phases amongst the amorphous material. NBSP4.0 had the crystal phase sodium phosphate ($Na_3P_2O_5$, ICDD ref: 01-071-1918) present; NBSP5.0 had sodium phosphate ($Na_3P_2O_5$, ICDD ref: 01-071-1918) and ($Na_4P_2O_7$, ICDD ref: 01-073-5982); NBSP5.5 had sodium phosphate ($Na_3P_2O_5$, ICDD ref: 01-071-1918), ($Na_4P_2O_7$, ICDD ref: 01-073-5982) and cristobalite (SiO_2, ICDD ref: 01-074-9378); and NBSP6.0 had only sodium phosphate ($Na_4P_2O_7$, ICDD ref: 01-073-5982). As the phosphate content increased the glasses became increasingly more crystalline, with a shift in the type of phosphate species present. The increase in phosphate content increases the need for sodium ions to charge compensate the phosphorus and are scavenged from the silicate network resulting in its repolymerisation [9].

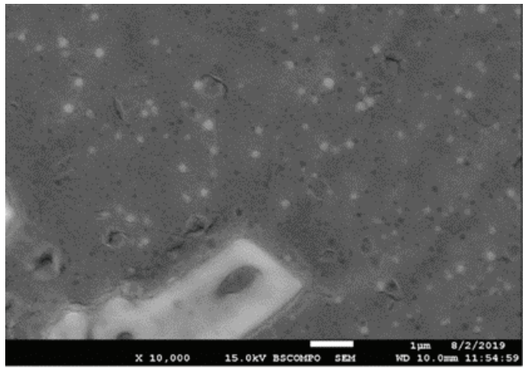

Figure 1 - Backscattered SEM image at x10000 of nucleation sites of sample NBSP6.0

Figure 1 shows nucleation sites where crystals have been growing, with the lighter circles potentially being the sites for sodium phosphate crystals, however, it is unknown what the black droplets are. This mixture of droplets may be indicative of liquid – liquid phase separation that may have occurred upon cooling. One phase may have cooled before the other as the P_2O_5 content increased in the glass system.

Table 1 - DTA and dilatometry Tg midpoints

Sample	DTA Tg midpoint (°C)	Dilatometry Tg midpoint (°C)
NBSP0.0	532 ± 3	532 ± 5
NBSP1.0	537 ± 3	535 ± 5
NBSP2.0	540 ± 3	545 ± 5
NBSP3.0	536 ± 3	539 ± 5
NBSP4.0	540 ± 3	561 ± 5
NBSP5.0	550 ± 3	564 ± 5
NBSP6.0	562 ± 3	569 ± 5

Table 1 contains the T_g midpoints measured by DTA and dilatometry of the NBSP samples. Between 0.0 and 3.0 mol% P_2O_5 in both the DTA and dilatometry data, T_g is the same within error. There is then a drastic increase between 3.0 and 4.0 mol% in the dilatometry data. The decrease in T_g at 3.0 mol% P_2O_5 in both DTA and dilatometry suggests that the network is becoming depolymerised.

Raman spectra showed that as the P_2O_5 content increased, there was a development and reduction of certain peaks at 731 cm^{-1}, 936 cm^{-1}, 987 cm^{-1}, 1011 cm^{-1}, 1028 cm^{-1} and 1162 cm^{-1}. Raman difference spectra were used to isolate potential phosphate specific intensities, with literature used as a guide to deduct causation (Table 2).

Intensity (cm-1)	Association
731	Symmetric stretching of P-O-P
936 - 987	Symmetric stretching of the P-O bond isolated in the PO_4^{3-} tetrahedral
1011	P-O stretching in $P_2O_7$4- or stretching vibration of P-O in the P(Q1) chain
1028	P-O symmetric stretching vibration of the $P_2O_7^{4-}$
1162	Symmetric stretching mode of the terminal oxygen on each tetrahedron, or the Symmetric stretching of P=O

Table 2 - Raman intensities and allocations

Conclusions

In conclusion, as P_2O_5 content increases, the level of crystallinity increases, as shown by XRD patterns. It is unclear by what mechanism phase separation is occurring and what type of phase separation there is without further analysis. However, there is evidence of nucleation sites, as seen in SEM images. Increasing the P_2O_5 content has had a double effect on the T_g of the glass system, increasing and decreasing, with the increase being indicative of the glass network re-polymerising and a decrease being indicative of T_g de-polymerising. Raman spectroscopy is showing a difference in the structure with the additions of P_2O_5, but the speciation of Si, P, B and Na cannot be understood without other structural analysis techniques such as solid-state NMR. However, the Raman difference spectra produced key intensities relating to phosphate species, but they could only be compared to relevant literature to obtain an indication of what may be causing them. These results have aided in the understanding of the effects P_2O_5 has on a borosilicate glass composition derived from relevant Hanford Site waste compositions. This will further inform future work with more complex comparable compositions.

Acknowledgements

Acknowledgements goes to Pacific Northwestern National Lab (PNNL) and the staff there, in particular Jaime George, Charmayne Lonergan, Derek Cutforth, Nathan Canfield, Michaella Swinhart and Naseeha Cardwell.

Acknowledgements goes to Albert Kruger from the Office of River Protection (ORP). Acknowledgements goes to Prof. Paul Bingham, Dr Anthony bell and Dr Wei Deng from Sheffield Hallam University (SHU). Funding acknowledgements goes to Sheffield Hallam University (SHU) and the US Department of Energy (DoE).

References

[1] C. H. Delegard and S. A. Jones, 'Chemical Disposition of Plutonium in Hanford Site Tank Wastes', PNNL-23468-Rev.1, 1233488, May 2015.

[2] J. Vienna, G. Piepel, D. Kim, J. Crum, and C. Lonergan, '2016 Update of Hanford Glass Property Models and Constraints for Use in Estimating the Glass Mass to be Produced at Hanford by Implementing Current Enhanced Glass Formulation Efforts', PNNL-25835, 2016.

[3] J. E. Shelby, *Introduction to Glass Science and Technology*. United Kingdom: Royal Society of Chemistry, 2005.

[4] H. Tanaka, 'Universality of Viscoelastic Phase Separation in Dynamically Asymmetric Fluid Mixtures', *Phys. Rev. Lett.*, vol. 76, no. 5, pp. 787–790, Jan. 1996.

[5] M. J. Plodinec, 'Borosilicate glasses for nuclear waste immobilisation', *Glass Technol.*, vol. 41, no. 6, pp. 186–192, 2000.

[6] P. Taylor, 'A review of phase separation in borosilicate glasses, with reference to nuclear fuel waste immobilization', Atomic Energy of Canada Limited, 1990. Accessed: Jul. 08, 2019. [Online]. Available: https://inis.iaea.org/collection/NCLCollectionStore/_Public/23/002/23002553.pdf?r=1&r=1

[7] D. R. Neuville and B. O. Mysen, 'Role of aluminium in the silicate network: In situ, high-temperature study of glasses and melts on the join SiO2-NaAlO2', *Geochim. Cosmochim. Acta*, vol. 60, no. 10, pp. 1727–1737, 1996.

[8] X. Cheng, R. K. Brow, and G. Chen, 'The dissolution behaviour in alkaline solutions of a borosilicate glass with and without P_2O_5', *J. Am. Ceram. Soc.*, vol. 100, no. 10, pp. 4519–4532, Oct. 2017.

[9] D. O'Donnell, S. J. Watts, R. V. Law, and R. G. Hill, 'Effect of phosphate content in two series of quaternary bio-glasses on structure and properties studied by magic-angle-spinning nuclear magnetic resonance (mas-nmr) spectroscopy - part ii: physical properties', 2008.

Bentonite-Chitosan composites or beads for heavy metal adsorption: design, preparation, and characterisation

Hassan Majiya[1, 2*], Francis Clegg[1], Chris Sammon[1]

[1] Materials and Engineering Research Institute, Sheffield Hallam University, UK
[2] Ibrahim Badamasi Babangida University, Lapai-Nigeria

Abstract

Water contamination with pollutants such as heavy metals is of significant concern because the toxicity exhibited by these metals can pose a severe threat to human health and the environment. Adsorption with the combined use of geological materials (such as clays) and biodegradable polymers seems to be a promising technique for purification of water contaminated with toxic metals. These materials not only provide a cost-benefit but are also materials derived from sustainable sources and are thus environmentally friendly. The current research project focuses on the preparation of functional composites or beads from bentonite clay and chitosan biopolymer. This paper investigates different preparation methods to assess the efficiency of mixing bentonite with chitosan, and the different forms of composites or beads made were investigated for their ability to remove Pb (II) ions from modelled solutions, initial results show that excellent adsorption was observed.

Introduction

Water contamination by toxic metals is a global environmental burden as it affects the quality of drinking water and hence human health. Lead (Pb) is one of the most toxic metals of public concern and even at low concentration, it can cause extended destruction to numerous biological systems [1]. Industrial effluents from manufacturing of lead-acid batteries and mining activities are the major source of Pb contamination in water and other environmental media [2]. Of all the current methods used in remediating metal-contaminated waters, adsorption is currently considered the most efficient and cost-benefit method, especially when functional composites (e.g., obtained from clay and biopolymers) are used as adsorbent [3].

The combination of the biopolymer chitosan with clay (such as bentonite) has been reported to improve their individual chemical and mechanical stability, which in turn also enhances its adsorption capacity. The presence of amine (-NH2) and hydroxyl (-OH) functional groups in the chitosan structure contributes to both polyelectrolyte and chelating properties [4]. Very few studies have been published on the adsorption of Pb (or other heavy metals) by bentonite-chitosan composite [5]. This study aims to more fully understand the contributing factors to heavy metal sorption on these composites.

Experimental Method

Bentonite-Chitosan (Bt-Ch) composites and beads were prepared (in the weight ratios of 90%/10%, 70%/30% and 50%/50%) via solution blending and precipitation methods, respectively. The composites and beads were characterised by thermogravimetric analysis (TGA), X-ray diffraction (XRD), and Fourier transform infraredw spectroscopy (FTIR). Batch adsorption procedures (via statistical design of experiments, DOE) were used to study the removal of Pb (II) ions (from aqueous solutions) by the Bt-Ch composites and beads, and the amounts of Pb (II) ions adsorbed were analysed using inductively coupled plasma optical emission spectrometry (ICP-OES).

Results

TGA curves (Figure 1) show that pristine bentonite has only two major weight loss occurrences, while that of Bt-Ch composites and beads are characterised by three stages. Greater weight loss in beads, compared to composites, is attributed to resulting higher loadings of chitosan in the former.

XRD results (Figure 2) generally show a greater reflection-shift towards lower angle and increases in relative intensity for beads compared to composites at relative initial chitosan loadings. This indicates more chitosan is present in the beads (as supported by TGA) and a higher proportion is intercalated between the clay layers.

FTIR results (Figure 3) show that the N-H deformation band (ranging from 1538 to 1564 cm-1) of chitosan shifts to lower frequencies when complexed in the Bt-Ch composites and beads indicating lower degrees of interaction through the N-H bond. The N-H bands observed in the composites are more intense than those in the beads, even though beads contain more chitosan, indicating a different interaction mechanism.

At optimal conditions of pH, initial concentration, and adsorbent dosage, established through DOE – Figure 4), the Pb (II) adsorption capacity (mg/g) estimated for 90%Bt-10%Ch and 70%Bt-30%Ch beads were higher compared to their corresponding composites. However, 50%Bt-50%Ch composites show a slightly higher adsorption capacity compared to the corresponding beads.

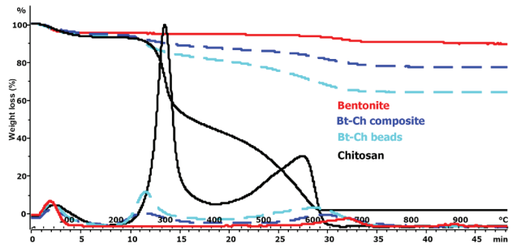

Figure 1 (A) TGA curves and their first derivatives of bentonite, chitosan, and Bt-Ch composites and beads

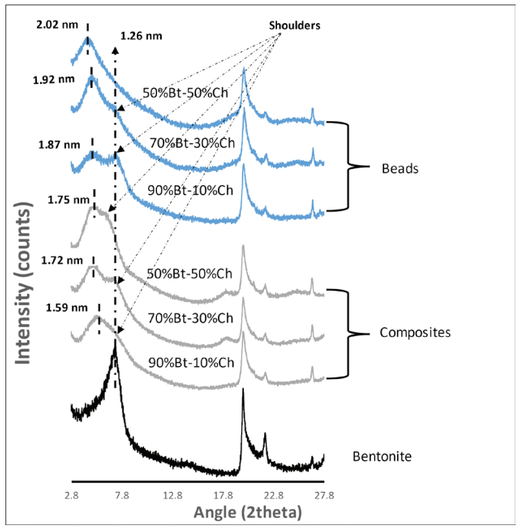

Figure 2 XRD patterns of bentonite, Bt-Ch composites/beads

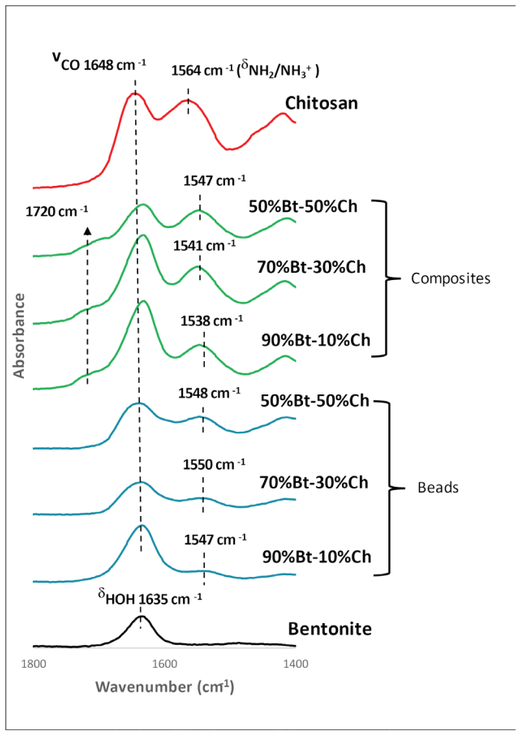

Figure 3 FTIR spectra of bentonite, chitosan, and Bt-Ch composites/beads

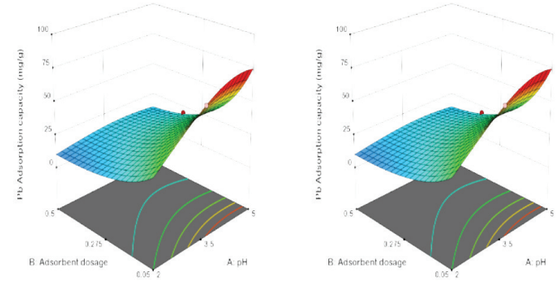

Figure 4 3D response surface plot for the Pb (II) adsorption capacity of Bt-Ch beads (left) and composites (right).

Conclusions

Novel Bt-Ch composites and beads have been synthesised, characterised, and successfully employed for the removal of Pb (II) ions from aqueous solutions. Excellent extents of adsorption were obtained for all the prepared Bt-Ch composites and beads. Thus, indicating the potential for using Bt-Ch beads and composites as cost-effective adsorbents for removal of Pb (II) ions from both drinking and wastewater to minimal and safe levels.

Further work is required to understand the mechanism and equilibrium isotherms concerning the adsorption of Pb (II) by Bt-Ch composites and beads. A column-based study will be investigated to assess the performance of Bt-Ch composites and beads for use in household water purification filter systems and industrial waste-water treatment.

References

[1] R. Deng, D. Huang, G. Zeng, J. Wan, W.Xue, X. Wen, X. Liu, S. Chen, J. Li, C. Liu, Q. Zhang, Decontamination of lead and tetracycline from aqueous solution by a promising carbonaceous nanocomposite: Interaction and mechanisms insight, *Bioresour. Technol*. 283, 277–285, (2019).

[2] W. Liu, B. Ma, F. Li, Y. Fu, J. Tai, Y. Zhou, L. Lei, Reduction of lead dioxide with oxalic acid to prepare lead oxide as the positive electrode material for lead acid batteries, RSC Adv. 6, 108513–108522, (2016).

[3] D.M. Saad, E.M. Cukrowska, H. Tutu, Selective removal of mercury from aqueous solutions using thiolated cross-linked polyethylenimine, *Appl. Water Sci*. 3 527–534, (2013).

[4] C.K.S. Pillai, W. Paul, C.P. Sharma, Chitin and chitosan polymers: Chemistry, solubility and fiber formation, *Prog. Polym. Sci.* 34, 641–678, (2009).

[5] J. Liu, L. Zheng, Y. Li, M. Free, M. Yang, Adsorptive recovery of palladium(II) from aqueous solutionontocross-linked chitosan/montmorillonite membrane, RSC Adv. 6 51757–51767, (2016).

Can pre-course anxiety and attitudes predict grade?

E.M. Marshall[1], P. Rowlett[1], D. Verrier[1] and T. Hunt[2]

[1] Sheffield Hallam University
[2] University of Derby

Abstract

Students often have preconceived ideas and anxiety about a course before they start which may impact on learning behaviour and even performance. This is particularly true for statistics modules which are compulsory but often unpopular components of many degrees. This paper investigates how academic constructs such as self-concept, anxiety, task value and performance relate to each other using data from Maths and Psychology UK undergraduate statistics courses. Maths based predictors and statistics self-concept were strong predictors of anxiety about performing statistical tasks at the start of a statistics course but were less related to year end performance. Although prior literature suggests that anxiety impacts negatively on performance this paper shows that relationships between intrinsic motivational beliefs and performance are moderated by statistics anxiety. How much a student values the learning of statistics impacts strongly on performance for highly anxious students whereas for moderately anxious students, self-concept is more important.

Introduction

Statistics is one of the most widely taught academic subjects within higher education and used widely in academic research across most disciplines. However, many students have negative attitudes towards learning statistics and it thought that up to 80% of students suffer with the situation specific statistics anxiety at some level [1]. The effects of statistics anxiety are described in [3] as *"characterised by extensive worry, intrusive thoughts, mental disorganisation, tension and physiological arousal"* when encountering statistical situations. Although statistics anxiety often initially stems from an anxiety about maths, research suggests that they are different constructs possibly due to statistics in higher education requiring more verbal reasoning and software skills rather than mathematical calculations [3,4].

Whilst several studies show statistics anxiety as a negative predictor of performance [2, 3, 4] it is more likely that is an indirect effect with anxiety, attitudes and motivational beliefs impacting on learning behaviour and subsequently performance [6,7]. Given the negative psychological and physical effects of statistics anxiety, it is not surprising that anxious students have a tendency to avoid statistical situations and are less likely to employ effective learning strategies, [6,7].

The expectancy-value motivational model suggests that attitudes such as self-concept and intrinsic value of learning are interlinked with an affective (anxiety) component and performance [5,6] which is summarised in Figure 1 in the context of learning statistics. Task value relates to how important the student perceives the task to be and their level of interest. The expectancy component centres on expectations of learning and performance such as self-efficacy to learn and the belief that success is tied to effort (control of learning). Prior research suggests that students who believe they are capable of learning statistics and are intrinsically motivated have lower levels of statistics anxiety and perform better in assessment [6,7]. When applying the model in the context of learning statistics, maths background has been shown to impact on statistics self-efficacy in particular [6] so should be added to the theoretical model.

The long term goal of this research is to develop interventions to address statistics anxiety but first an understanding of the relationships between attitudes and other related concepts is needed [2]. This paper will test the expectancy-value model in the context of learning statistics for students studying Maths and Psychology and evaluate the strongest predictors of performance.

Methodology

First and second year students studying Maths or Psychology at Sheffield Hallam University and the University of Worcester were surveyed at the start of the year in 2018/19 and 2019/20. Actual performance from the end of the first year of teaching was added to the survey data which was standardised by institution and discipline. In addition to demographic questions, several existing scales were used to measure the different aspects of attitudes, anxiety and learning behaviour. The main measure of statistics anxiety was the 8 item Statistical anxiety measure which asks how anxious students feel in a range of situations on a 7 point Likert scale ranging from not at all anxious (1) to Extremely anxious (7). Other scales used a 7 point Strongly disagree – strongly agree range which included self-efficacy for maths anxiety (SEM), PISA maths confidence, Survey of attitudes to statistics (SATS) and Motivated learning strategies questionnaire (MLSQ) which was specifically designed to assess aspects of the expectancy-value model and learning strategies. Reliability for all subscales was high so the scale means were used in analysis.

Results and discussion

The 1st year 2018/19 dataset contained 41 mathematics students and 286 Psychology students from either Sheffield Hallam (199) or the University of Worcester. 62 Maths students and 181 Psychology students completed the 2nd year survey. Over 90% of the first year students had some anxiety about statistics with 42% of maths students and 76% of Psychology students having moderate to high levels of statistics task anxiety which is likely to impact substantially on learning. There were no significant discipline differences in mean statistics anxiety after controlling for either gender or having higher maths qualifications. Of these students, 72% of Maths students and 79% of Psychology students expected statistics to be difficult.

Although maths based factors such as maths anxiety and lack of confidence with maths do correlate positively with statistics anxiety, in total they only explain 43% of the variation in stats anxiety for Psychology and 20% for maths students suggesting that maths and stats anxiety are related but separate constructs.

Figure 1 contains the pre and post assessment correlations between the components of the expectancy-value model with the correlations for maths students in brackets. To simplify results, factor analysis was used to create overall scores to represent maths negativity, statistics self-concept (expectancy) and task value from relevant sub-scales.

The expectancy factor of the model has a high score for students with high self-efficacy, who believe they are capable of learning statistics if they study appropriately (control of learning) and do not expect to struggle. This component shows a strong negative relationship with statistics anxiety which increases after the first year of teaching. Self-efficacy at the start of the year does not impact on end of year performance but not surprisingly, post assessment self-efficacy is moderately related to prior grade. Maths negativity also impacts negatively on self-concept with statistics and end of year assessment scores for Psychology students.

Figure 1 Expectancy-value model correlations for Psychology

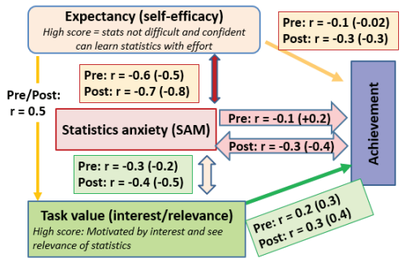

(Maths in brackets)

Task value is represented by scales for how interested the student is in learning statistics and the value they place on learning statistics. Task value at the start of the course is weakly negatively correlated with both anxiety and end of year performance but these relationships strengthen by the beginning of the second year. Although other research has shown a negative relationship between anxiety and performance, pre-course anxiety is only weakly related to end of year performance and this affect is actually positive for maths students. There is a stronger negative relationship between post assessment statistics anxiety more in line with existing literature but it is difficult to know whether high statistics anxiety impacted on grade (cognitive interference theory) or whether students are anxious because they didn't do well (deficit theory) in the 2nd year data set.

As there were differences in relationships for the different aspects of task value in particular, pre-course measures of statistics self-efficacy, control of learning, anticipated struggle, perceived interest, relevance, enjoyment and maths negativity were used in backward regression models to predict performance.

The final model for maths students contained statistics anxiety (β=5.5), control of learning (β=9.7) and perceived enjoyment and explained 43% of the variation in grade. Pre-course statistics anxiety was also a positive predictor of performance for Psychology students (β=1.7) after controlling for maths background (β=-4.6) and value of statistics (β=2.6) although the model only explained 8% of the variation. Further investigation was carried out into how these different variables interact with each other to explain the unexpected relationship between statistics anxiety and performance using subgroups of statistics anxiety. As shown in the example interaction plot for Psychology students in Figure 2, positive attitudes such as relevance have more impact on performance for the groups with the highest and lowest levels of statistics anxiety so if a student is highly statistics anxious but has intrinsic motivation to learn, they can perform as well or even better than students with lower levels of anxiety. For maths students, the belief they are capable of learning with effective study shows a similar pattern and for Psychology it is the students who are more stats than maths anxious and see the relevance of learning statistics who do well. Task value has no real impact on performance for those who are moderately anxious but for them the relationship between self-concept and performance is stronger. These findings suggest that statistics anxiety moderates the relationships between expectancy, task value and performance and subsequently, applying different strategies to students with different levels of statistics anxiety may improve attainment.

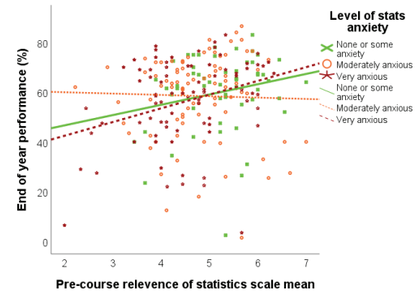

Figure 2 Interaction between post interest and statistics anxiety

Conclusions

This paper investigated whether the expectancy-value model of motivation can be applied to attitudes and anxiety about statistics before and after a first year undergraduate statistics course and whether performance can be predicted from pre-course measures. Contrary to previous research suggesting statistics anxiety is a direct and negative predictor of performance, this research found that the most anxious students can perform better when intrinsic motivation is high and moderately anxious students would benefit more from improving confidence in maths and statistics. The results of this analysis suggest introducing more relevant and interesting topics at the start of a first year course may reduce anxiety and increase attainment for anxious students with some students also needing sessions to improve maths confidence.

References

[1] Onwuegbuzie, A. J. & Wilson, V. A. (2003) Statistics anxiety: nature, etiology, antecedents, effects and treatments: a comprehensive review of the literature, Teaching in Higher Education, 8, 195–209.

[2] Chew,P.K.H. & Dillon, D.B. (2014). Statistics anxiety update: Refining the construct and recommendations for a new research agenda. Perspectives on Psychological Science. 2014; 9: 196±208.

[3] Zeidner, M. (1991) Statistics and mathematics anxiety in social science students—some interesting parallels, British Journal of Educational Psychology, 61, 319–328.

[4] Paechter, M., Macher, D., Martskvishvilli, K., Wimmer, S., & Papousek, L. (2017). Mathematics anxiety and statistics anxiety: Shared but unshared components and antagonistic contributions to performance in statistics. Frontiers in Psychology, 8, 1196.

[5] Baloglu, M., Abbassi, Amir., & Kesici, S. (2017). Multivariate Relationships between statistics anxiety and motivational beliefs. Education, Volume 137, Number 4, Summer 2017, pp. 430-444(15)

[6] Chiesi, F., & Primi, C. (2010). Cognitive and non-cognitive factors related to students' Statistics Achievement. Statistics Education Research Journal, 9(1), 6-26.

[7] González, A., Rodríguez, Y., Faílde, J.M., Carrera.M.V. (2016). Anxiety in the statistics class: Structural relations with self-concept, intrinsic value, and engagement in two samples of undergraduates. Learning and Individual Differences, 45, 214-221.

Influence of pre-wetting on the Nanolime performance for the Consolidation of Limestone Museum Objects

C. Maucourant [a,*] and F. O'Flaherty [a]

[a] Materials and Engineering Research Institute (MERI), Sheffield Hallam University, Sheffield, S1 1WB

Abstract

Nowadays, the majority of stone conservation treatments carried out in museums use incompatible products to consolidate limestone artefacts. The introduction of nanolime as a "new" consolidant in a museum context is something innovative. In collaboration with the British Museum, a nanolime-based consolidation treatment is currently being developed in the MERI laboratories. This paper introduces the research methodology followed to design the new treatment and, in particular, presents information on the influence of pre-wetting prior to the application of the nanolime.

Introduction

"Nanolime" consists of hexagonal platelet nanoparticles of Calcium Hydroxide (Ca(OH)2) dispersed in short-chain aliphatic alcohols such as Ethanol or (Iso)Propanol (Figure 1). Depending on the synthesis route, resulting dispersions contain nanolime particles with size from 20 to 400 nm [1]. Nanolime restores the cohesion of the stone matrix by regenerating mineral bridges with new calcite, where the routinely used museum treatments form a film which "wraps" the deteriorated area of the stone, consolidating it only partially (Figure 2). Introducing nanolime in a museum context requires testing its performance and limits beforehand. Nanolime performance can be affected by various factors [2]. In this paper, the impact of wetting techniques and methods of application on the penetration of nanolime and consolidation efficiency is assessed. The main disadvantage with the nanolime as a consolidation treatment is its limited penetration into low porosity substrate (f < 20%). This can be caused by a phenomenon described as back-migration of the nanoparticles towards the treated surface. Ways to tackle this issue in improving the nanolime retention will be presented too.

Experimental Method

Two types of limestone have been selected to carry out the laboratory tests: archaeological blocks from the British Museum research storage and Lavoux limestone samples coming from Canterbury Cathedral masonry elements, and replacement quarried blocks (Figure 3). First, the petro-graphical (steromicroscopy/PLM), physical (MIP), chemical (XRD / FTIR) and mechanical (DRMS / STT) properties of the samples were determined. Then, laboratory experiments were carried out on Lavoux samples, and to finish, confirmation tests were performed on the archaeological blocks from the British Museum.

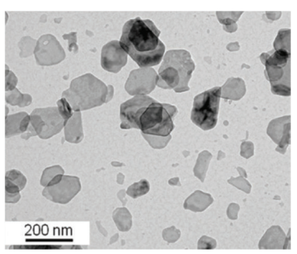

Figure 1. Micrograph of nanolime particles observed with the TEM

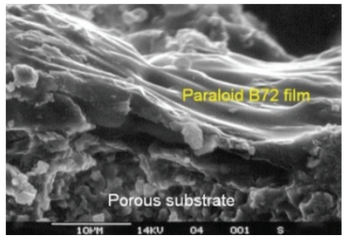

Figure 2. Deteriorated limestone consolidated with acrylic resin Paraloid ® B72

Figure 3. Examples of limestone samples used in the project

Two commercial nanolime dispersions (CaloSiL® and Nanorestore® Plus) in ethanol at three different concentrations (5g/L, 10g/L and 25g/L) were used for the experiments, however, only the results using Nanorestore® Plus are presented in this paper. Four pre-wetting techniques, namely: solvent atmosphere by means of an ultrasonic atomiser, steam cleaning, soaking/brushing, and karsten tube penetration, using de-ionised water and industrial methylated spirit have been tested (Figure 4).

Figure 4. Pre-wetting techniques used for the experiments: Ultrasonic atomiser (A); Steam cleaning (B); Karsten tube penetration (C); and soaking (D)

The nanolime dispersions were applied using conventional methods (i.e., bushing, pipetting, and spaying), injecting using a medical drip system or a syringe, or mixed in laponite/methyl cellulose gels and arbocel poultice. To improve the retention of the nanolime inside the stone matrix, the

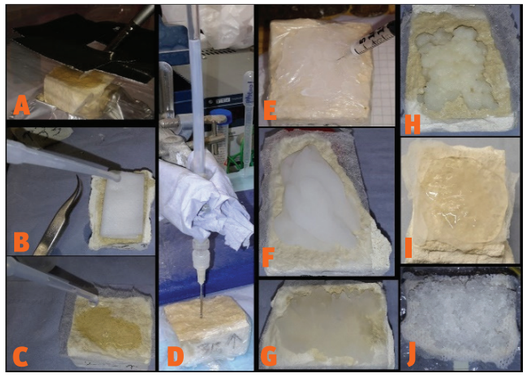

use of hydrogel and solvents (de-ionised water, butanol, and isopropanol) characterised by different evaporation rates were considered (Figure 5).

Figure 5. Application of the nanolime by brushing in an air-tight environment (A), pipetting (B & C), injecting (D & E), mixed in gels and poultice (F–I), or combined with hydrogel (J)

After the nanolime treatment, the samples were put into a curing chamber (75% ± 5% RH, 19–21°C and 0.1–0.5% CO2) for 2 months to allow the carbonation of the nanolime. The nanolime penetration was assessed 24h after application by means of a phenolphthalein indicator (1% W/V in 60% of IMS and 40% of water). The consolidation effectiveness was evaluated using a DRMS 2months after the application of the treatment.

Results and Discussion

The results of the characterisation tests of the samples used for the experiments are shown in Table 1. Phenolphthalein results showed that the nanolime penetration can be increased by 2 to 5mm when the sample is pre-wetted with a combination of techniques prior the application of the nanolime (Figure 6). DRMS results showed that applying the nanolime by using different methods can affect the consolidation performance and depending on the technique used, a superficial or an in-depth consolidation can be obtained (Figure 7).

Limestone type (PLM)	Mineral composition (XRD/FTIR)	Porosity (MIP)	Drilling Resistance (DRMS)	Superficial cohesion (STT)
Intrabiope Imicrite (Lvx) or (intra) biomicrite (BM)	Calcite/ Dolomite (Lvx) with Kaolinite/ Sepiolite (BM)	From 13% to 24% (Lvx) or from 11% to 31% (BM) with a PSD from 0.007µm to 5-10µm (Lvx) or 30-100µm (BM)	From 0.60N to 3.40N (Lvx) or 0.30N to 4.40N (BM)	Materials removed from 3.50 mg/cm² to 17mg/cm² (Lvx) or from 1.80 mg/cm2 to 34.30 mg/cm² (BM)

Table1. Characterisation results for the samples used in this project. "Lvx" stands for Lavoux; "BM" for British Museum, and "PSD" for "Pore Size Distribution".

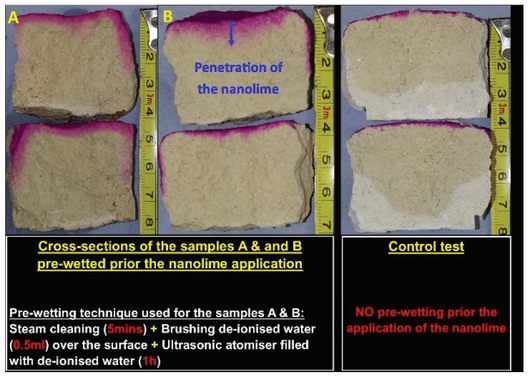

Figure 6. Comparison of phenolphthalein results for the samples pre-wetted (A & B), and sample not pre-wetted (C)

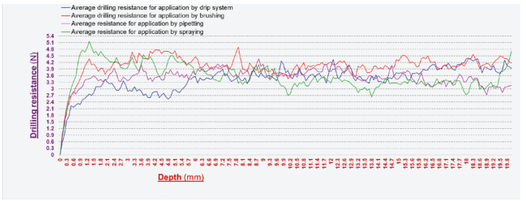

Figure 7. DRMS results of samples treated by 4 different methods of application.

Conclusions

Pre-wetting the sample with a combination of techniques seems to improve the penetration of the nanolime. DRMS graphs show that the optimal method of application would be the brushing for an in-depth consolidation, or the spraying for a superficial consolidation. However, it can be concluded that there is not one optimal method of application and the conservator should tailor the treatment methodology to the condition of the object to be consolidated. The application of the optimal treatment on different types of limestone will be the last experimental phase, before the in-situ conservation tests to be carried out at the British Museum.

References

[1] Otero, J., Starinieri, V., and Charola, A. E. (2018). Nanolime for the consolidation of lime mortars: A comparison of three available products. *Construction and Building Materials 181*, pp. 394-407.

[2] Otero, J., Starinieri, V and Charola, A. E. (2019). Influence of substrate pore structure and nanolime particle size on the effectiveness of nanolime treatments. *Construction and Building Materials 209*, pp.701-708.

List of abbreviations

PLM: Polarised Light Microscopy

TEM: Transmission Electron Microscope

XRD/XRF : X-Ray Diffraction / X-Ray Fluorescence

FTIR: Fourier-Transformed Infrared Spectroscopy

MIP: Mercury Intrusion Porosimetry

DRMS: Drilling Resistance Measurement System

STT: Scotch Tape Test

Development of a safe Human-Robot interaction and coordination model

M.R. Rahman [a,†], L. Alboul [a], L. Nisiotis [b], J. Penders [a], A.D. Nuovo [a]

[a] Centre for Automation and Robotics Research, Sheffield Hallam University, Sheffield, S1 1WB
[b] University of Central Lancashire, Cyprus, Larnaca, Pyla

Abstract

Application of co-working robots safely and comfortably in the daily process flow requires not only technical safety but also a level of comfort for the human worker. This study mostly focuses on how the working space of a collaborative robot can be controlled in order to explore various safe and personified movements and make it suitable to work alongside a human co-worker.

Introduction

The concept of human and robot co-working is considered very promising. Human-Robot Collaboration (HRC) implies that a robot enters the personal workspace and comfort zone of its human co-worker. Technical safety is largely accounted for by the robot supplier; however perceived safety and teamwork related aspects are less investigated and still remain important research topics. To address these topics, this paper offers a preliminary assessment of some design factors that have been considered on how collaborative robot arms can be manipulated to design safe and personified movements.

Manipulator robots are one of the most useful forms of robotics technology, which comprises complex design implementation. The benefits of these manipulator robots have expanded their applications to a variety of industries, including medical, environmental, food, amongst others. According to investigators [1] to [3], in order to achieve spontaneous and continuous human-robot collaborations, several methodologies have been investigated and employed. Such systems that range from robotic manipulators [4] to fully functional humanoid robots [5] are expected to help the human user in various tasks, some of which require collaborative effort for a safe, successful, and time & energy efficient execution. To establish efficient and effective human robot collaboration, mutual understanding is required. This type of communication facilitates the approach to a better task performance of the robot and task reduction for the human worker. It is essential that the robot be capable of interpreting several communication mechanisms similar to mechanisms involved in human-human interaction [6].

The main focus of this project is the development of a custom model with functionalities to design safe robot arm movements. In addition, coordination methods will be examined for their application on fluent and effective human-robot collaboration and extend views on future developments. This study could help in development and implementation of tracking and fetching algorithms for collaborative robots. Several experiments will be conducted to overcome any challenges based on external factors, such as unanticipated obstacles. The initial research has been carried out using the Fetch mobile manipulator discussed in the 'Experimental Method' section. For manipulation tasks, the exchange of objects between human and robot is a basic way to coordinate movements and jointly perform useful work [7].

Conclusive results of our experiments will help develop further design standards for robot arm manipulation and contribute to human-robot co-working quantitative models.

Experimental Method

The experiment focuses on implementing a pick and place application setup, which comprises the Fetch robot arm and the use of Robot Operating System (ROS). Python and/or MATLAB programming has been used to code the ROS packages. The idea is to achieve different variations of safe robot arm movements around a human user or any obstacles. The motion planning scenarios have been executed through the Gazebo simulator and RVIZ 3D visualisation tool [figure 1]. Based on the kinematics results, the motion formation will be designed to construct the robot arm configuration space and the robot arm workspace. When feasible results are reached, the experiment can go forward with human participant trials in a shared workspace.

The software will be designed to enable the robot arm to read its sensors' data, make itself aware of the workspace and make motion decisions, i.e., avoiding obstacles while in motion. The main task would be to complete an action, for example, a pick and place motion and move its end-effector from point 'A' to point 'B' while avoiding any human or obstacles.

The Fetch mobile manipulator is designed to be robust and of high-performance [8]. Fetch is equipped with a single 7 degree-of-freedom arm which supports up to a 6 kg payload, including the gripper. The Fetch also consists of useful sensors that will be utilised in this study. 1) Base Laser - SICK TIM571 scanning range finder. The laser has a range of 25m, 220° field of view; 15Hz update rate and angular resolution of 1/3°. The laser publishes both distance and RSSI (Received Signal Strength Indication) to the base_scan topic. 2) IMU - 6-axis inertial measurement unit (IMU). The gyroscope within the IMU is capable of measuring +/-2000 degrees per second, while the accelerometers are capable of measuring +/-2g. 3) Head Camera - Primesense Carmine 1.09 short-range RGBD sensor. This camera is best calibrated in the 0.35-1.4m range. 4) Gripper Sensors - in addition to the position and effort feedback of the gripper joint, the gripper incorporates a 6-axis inertial measurement unit (IMU) as well.

The Main tasks for this study are:

- Identification and location of obstacles.
- Application of motion planning algorithm.
- Calculate the path avoiding the obstacles.
- Based on the path, calculate robot arm joint configurations.
- Finally, evaluate the joint positions to move safely and reach the goal.

Simulation experiments have been carried out based on existing path and trajectory planning methods to distinguish between the two and we now intend to extend these experiments to implement the motion configuration.

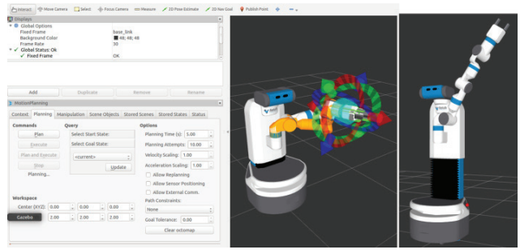

Figure 1 Fetch RVIZ Motion planning simulator.

Results and Discussion

The program at this point has only been tested and simulated for moving the robot arm from one point to another through path planning as illustrated in figure 2 and figure 3, i.e. from point 'A' to point 'B', just to test its feasibility. Further testing will be carried out to improve the robot arm dynamics and assess the safety across human co-worker and any obstacles.

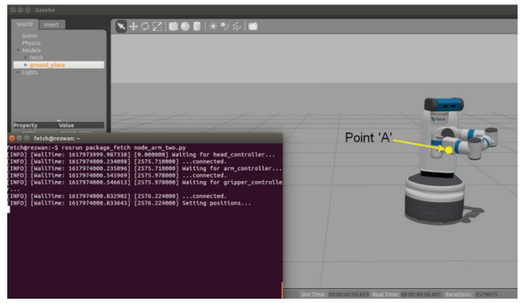

Figure 2 Gazebo Simulation of robot arm in starting position, 'Point A'.

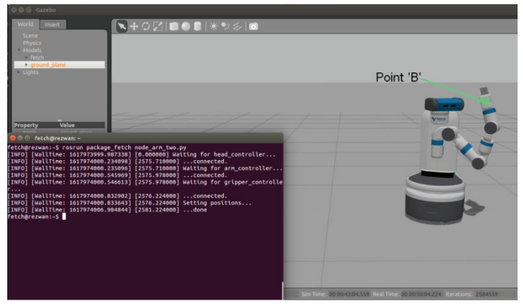

Figure 3 Gazebo Simulation of robot arm to the end position at 'Point B'.

Conclusions

Within this paper, it has been reported that an experimental study is underway to determine safe and improved human-machine interaction in a simple pick and place application. The proposed study can open an interesting opportunity for future work in refining the robot arm's gestures and effectively reaching human workspace without any hazard. Initially the pick and place experiments will be carried out in the simulation and then be implemented with a real robot in our lab. The ranges of robot movements will be determined and based on those measurements' experiments involving humans will be initiated.

References

[1] S. Robla-Gomez, V. Becerra, J.R. Llata, E. Gonzalez-Sarabia, C. Torre-Ferrero and J. Perez-Oria, "Working Together: A review on safe human-robot collaboration in Industrial Environments" IEEE Access, vol. 5, pp. 26754–26773, 2017.

[2] M Dohi, K. Okada, I. Maeda, S. Fujitani and T. Fujita, "Proposal of Collaboration Safety in a Coexistence environment of human and robots", IEEE International Conference on Robotics and Automation, 2018, pp. 1924–1930.

[3] M.J. Rosenstrauch and J. Kruger, "Safe Human Robot Collaboration – Operation Area Segmentation for Dynamic Adjustable Distance Monitoring", in 4th International Conference on Control, Automation and Robotics, 2018, pp. 17–21.

[4] A. Albu-Schaffer, S. Haddadin, C. Ott, A. Stemmer, T. Wimbock and G. Hirzinger, "The DLR light-weight robot: design and control concepts for robots in human environments", Industrial Robot: An International Journal, vol. 34(5), pp. 376–385, 2007.

[5] Tsagarakis et al., "Walk-man: A high performance humanoid platform for realistic environments", in Journal of Field robotics, 2016.

[6] B. Curuklu, G. Dodig-Crnkovic and B. Akan, "Towards Industrial Robots with Human-like Moral Responsibilities", 5th ACM/IEEE International Conference on Human-Robot Interaction, pp. 85–86, 2010.

[7] A. Edsinger and C.C. Kemp, "Human-Robot Interaction for Cooperative Manipulation: Handing Objects to One Another", in 16th IEEE International conference on Robot and Human Interactive Communication, August 26-29, 2007.

[8] M. Wise, M. Ferguson, D. King, E. Diehr and D. Dymesich, "Fetch Robotics Inc, Fetch & Freight: Standard Platforms for Service Robot Applications", USA, 2016.

Alternative reductants for vitrification of high-iron high-level radioactive waste streams

J. C. Rigby [a,†], D. Dixon [b], D. Cutforth [b], J. Marcial [b], J. Klouzek [c], R. Pokorny [c], A. Scrimshire [a], A. A. Kruger [d], A. M. T. Bell [a], P. A. Bingham [a]

[a] Materials and Engineering Research Institute, Sheffield Hallam University, Sheffield, S1 1WB
[b] Pacific Northwest National Laboratory, Richland, WA, 99352
[c] Laboratory of Inorganic Materials, University of Chemistry and Technology, 166 28 Prague 6
[d] Department of Energy, Office of River Protection, Richland, WA, 99352

Abstract

Foaming during vitrification of nuclear waste in a Joule-Heated Ceramic Melter is caused by trapping of batch gases, such as CO_2 and O_2, beneath a highly viscous reaction layer called the “cold cap”. Foaming restricts heat transfer during melting and can cause blockages of melter components. Sucrose is effective in reducing foam in wastes high in nitrates. However, for wastes high in multivalent species, such as iron, which produce O^2 by high-temperature redox reactions, other carbon-based reductants are investigated. Foaming behaviour and redox behaviour during melting is compared between a range of reductants, as well as the final glass quality. Graphite and coke both have a greater effect on the reduction of foam than sucrose at 3 wt% addition to the batch.

Introduction

The Hanford site in Washington State, US is home to ~200,000 m3 of radioactive legacy wastes stored in 177 carbon-steel tanks underground [1]. Waste Treatment Plants (WTPs) are currently under construction at the site to vitrify separately High-level Wastes (HLW) and Low Activity Wastes (LAW), in direct-feed Joule-Heated Ceramic melters (JHCM). Waste feed is mixed with glass forming chemicals (GFCs) on entry into the melter and lands on top of the melt pool creating a batch reaction layer called the “cold cap” [2].

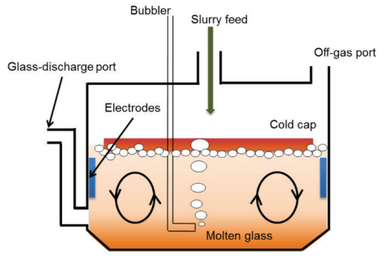

Figure 1. Schematic of the JHCM system

Foaming in the cold cap, due to trapped gases evolving beneath the viscous melt, can insulate the melt pool, reducing heat transfer to the reacting material and therefore reducing the efficiency of the process. In extreme cases foaming poses a risk of blocking melter components [3].

In this study the effect of sucrose as a reductant is compared with other carbon-based materials to determine the effects on foaming and redox behaviour during melting. Other reductants include formic acid, N-Carboxymethyl-N′-(2-hydroxyethyl)-N,N′-ethylenediglycine (HEDTA), coke dust and graphite, these are all explored in older literature of glass making [4, 5]. The aim is to determine the effect of these reductants on the foaming behaviour, particularly whether any of them affect the secondary foaming involving high temperature evolution of O_2. As well as evaluating the foaming behaviour and processability in a JHCM.

The high-iron inactive simulated feed, HLW-NG-Fe2, shown in Table 1, was developed by The Vitreous State Laboratory (VSL), DC, and is of particular interest for exploring the foaming behaviour of HLW feeds as it foams up to 10 times its original volume [6]

Raw Material	Batch/ 100 g	Raw Material	Batch/ 100 g
$Al(OH)_3$	8.61	$Ni(OH)_2$	0.59
H_3BO_3	0.56	$FePO_4.2H_2O$	1.71
$Na_2B_4O_7.10H_2O$	37.16	PbO	0.63
$CaCO_3$	0.94	Na_2SiO_3	8.03
CeO_2	0.12	Na_2SO_4	0.39
$Cr_2O_3.1.5H_2O$	0.30	SiO_2	37.33
$Fe(OH)_3$	20.54	$SrCO_3$	0.28
$La(OH)_3$	0.11	ZnO	0.03
Li_2CO_3	3.87	$Zr(OH)_4.0.654H_2O$	1.57
$Mg(OH)_2$	0.24	$NaNO_2$	0.01
MnO_2	3.98	$NaNO_3$	0.45
NaOH	0.81	$H_2C_2O_4.2H_2O$	0.06
Na_2CO_3	4.04	Total	132.36

Table 1. HLW-NG-Fe2 composition developed by the VSL to immobilise the C-106/AY-102 high-iron tank waste [7].

Experimental Method

The HLW-NG-Fe2 feed was batched as in Table 1. The second feed, named HLW-NG-Fe2-II, was batched with $FeC_2O_4.2H_2O$ replacing the Fe(OH)3 raw material on a wt% basis for the target Fe_2O_3 content. Further feeds were batched with the HLW-NG-Fe2 composition with 3 wt% additions of sucrose, formic acid, HEDTA, coke (85% C) and graphite. Feeds were batched on a 2 dp scale with >99% purity raw materials. The iron hydroxide source was a slurry with 13 wt% $Fe(OH)_3$. Chemicals were mixed with deionised water with a target glass yield was 400 gL^{-1} for HLW-NG-Fe2-II, and 290 gL-1 for HLW-NG-Fe2. Feeds were stirred continuously during batching, once mixed ~1L of feed was dried in an oven at 105°C for 24 hours and then milled for further techniques.

Feed Name	Reductant Carbon Source	Reducing Equivalents / g
HLW-NG-Fe2	-	-
HLW-NG-Fe2-II	Fe^{2+} raw material ($FeC_2O_4.2H_2O$)	
HLW-NG-Fe2-S	Sucrose ($C_{12}H_{22}O_{11}$)	0.129 [8]
HLW-NG-Fe2-G	Graphite (C)	0.333 [8]
HLW-NG-Fe2-C	Coke Dust (85% C)	
HLW-NG-Fe2-F	Formic Acid (CH_2O_2)	0.0435 [8]
HLW-NG-Fe2-H	$C_{10}H_{16}N_2O_8$	0.139 [8]

Table 2. Raw materials used for each of the feeds and the associated reducing equivalents where available.

To quantify the amount of foaming during melting, pellets of each of the dried feeds were heated at 10°C/min to 1150°C in a furnace with an observation port. Photographs were taken at regular temperature intervals. Images were analysed using photoshop for their area. Normalised volume was deduced based on the assumption that the expansion was spherically symmetric.

Results and Discussion

Feed expansion tests in Figure 3 show the range of foaming behaviours of the 7 different feeds and they are compared with the reducing equivalents per gram of compound where a value was available from the literature in Figure 4. The value for coke was taken from 85% of the value of graphite, assuming the reducing equivalents per gram is linearly correlated with carbon content per gram. While sucrose has an effect on the maximum foam volume, graphite and coke have a significantly greater effect. The iron oxalate feed, HLW-NG-Fe2-II also shows a reduction in foaming with a maximum V/V0 of ~5 compared to 8.5 in the original feed.

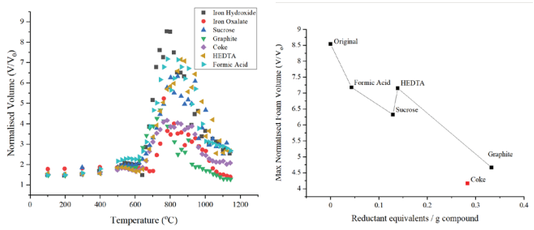

Figure 3. Normalised volume of pellets during Feed Expansion Test with different reductant and raw material feeds.

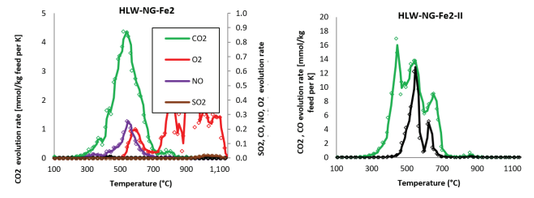

Figure 5. Evolved gas analysis of the HLW-NG-Fe2 (top) and HLW-NG-Fe2-II (bottom) feeds during heating to 1150 °C.

Evolved gas analysis of the HLW-NG-Fe2 and HLW-NG-Fe2-II feeds show a remarkable difference in the gases and quantities of gases evolved. The HLW-NG-Fe2-II feed produces ~17 mmol / kg of feed at its maximum around 400 °C, as well as ~13 mmol / kg feed of CO at its maximum.

The original feed evolves only ~4.5 mmol / kg feed at its peak, however as discussed, this feed evolves a significant amount of O_2 at high temperatures when the glass melt viscosity is high.

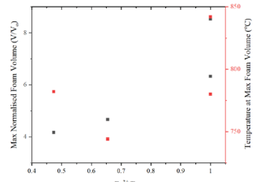

Figure 6. Iron redox Fe3+/FeT with reducing equivalents/gram of reductant added to the feed.

The final redox state of each of the glasses was estimated by Mössbauer spectroscopy and related to the maximum foam volume and temperature at maximum foam volume in Figure 6. While we are unable to detect small amounts of reduced iron in these feeds, we can observe a trend in the maximum foam volume and final glass redox state. There is no clear trend in the temperature of maximum foaming, which has direct implications on overall melting rate [2].

Conclusions

The amount of foam produced in a glass melt, observed by feed expansion tests, is related to the temperature at which gases evolve and the melt viscosity at these temperatures rather than the total gas evolution. Using a reduced raw material for iron in the HLW-NG-Fe2 feed reduced the foaming during melting to ~60% of the original by evolving more CO and CO_2 at lower temperatures before the glass melt was viscous. Furthermore, using graphite and coke additions reduced the maximum feed foaming to ~52% and ~49%.

Implications for reduced foaming include more efficient and safer melting processed, however the reduction in Fe3+/FeT and the amount of spinel crystallisation in the final glasses with graphite and coke as reductants is concerning for the long-term durability of the glass product. Tests of chemical durability and corrosivity would be required.

References

1. Xu K, Hrma P, Rice JA, Schweiger MJ, Riley BJ, Overman NR, et al. Conversion of Nuclear Waste to Molten Glass: Cold-Cap Reactions in Crucible Tests. J Am Ceram Soc. 2016;99(9):2964–70.
2. Pokorný R, Hilliard ZJ, Dixon DR, Schweiger MJ, Post Guillen D, Kruger AA, et al. One-Dimensional Cold Cap Model for Melters with Bubblers. J Am Ceram Soc. 2015;98(10):3112–8.
3. Henager SH, Hrma P, Swearingen KJ, Schweiger MJ, Marcial J, TeGrotenhuis NE. Conversion of batch to molten glass, I: Volume expansion. J Non Cryst Solids. 2011;357(3):829–35.
4. 21 Simpson, W., & Myers, D. D. (1978). Redox Number Concept and Its Use By the Glass Technologist. *Glass Technology*, 19(4), 82–85.
5. 22 Fedorov, A. G., & Pilon, L. (2002). Glass foams: Formation, transport properties, and heat, mass, and radiation transfer. *Journal of Non-Crystalline Solids*, 311(2), 154–173.
6. Matlack KS, Viragh C, Kot WK, Pegg IL, Joseph I. Effect of the Form of Iron on HLW Melt Rate VSL-15R3430-1. Washington, D. C.; 2015.
7. Ryan, J. L. (1995). Redox Reactions and Foaming in Nuclear Waste *Glass Melting*. Richland, WA, USA
8. Pokorný R, Hrma P. Model for the conversion of nuclear waste melter feed to glass. J Nucl Mater. 2014;445(1–3):190–9.

Research and Development of Liquid Cooled Racks in Data Centres

R. Sethuramalingam [a, †], A. Asthana [a, †]

[a] Materials and Engineering Research Institute, Sheffield Hallam University, Sheffield, S1 1WB.

Abstract

In 2016, global data centres consumed 416 TWh of electricity (which is more than that used by the entire UK and the demand has been growing exponentially since then, and especially during the pandemic. Data centres now account for 4% of the global greenhouse gas emissions. This electricity is eventually converted into heat which must be removed for safe operation of servers. The cooling of data centres is again energy intensive. Replacing the inefficient traditional air-cooled systems by water/liquid cooled systems offers an alternative approach with significant energy and cost savings advantages. A prototype water-cooled rack cabinet and test rig are developed here, holding 40 kW servers with rear-door cooling. Results of experimental data from the test rig are presented on cooling performance, energy efficiency and cost savings.

Introduction

Rapidly increasing global internet traffic, mobile internet users and the number of Internet of Things (IoT) connections are driving exponential growth in demand for data centre and network services, which in turn is driving their electricity demand. Also, Mobile operators are progressing 5G technology, three times more energy intensive than 4G. Increasing data centre electricity demand is a concern because most electricity today is still generated using fuels with a high carbon intensity — coal, oil, and gas. Burning fossil fuels increases carbon in the atmosphere (which contributes to climate change) and damages air quality (which has been linked to poor health and millions of deaths worldwide). A 2020 EU report projects that by 2025, data centre energy use will exceed 2018 levels by 21% [1]. The cooling of data centres is the second largest power consumer after servers. The cooling energy varies from 10% of the total energy consumption in the most efficient data centres and goes up to 45% in standard air-cooled data centres.

Air Cooling method is the traditional method of cooling the IT equipments in the data centres. Conventionally, the data centre racks hold the servers in the rows which will be divided by the aisle. These aisles have tiles for air intakes for the servers which are called hot or cold aisles as shown in the figure 1 for cold aisle [2]. The server racks are placed in the raised floor configuration where the cold air from the Computer Room Air-Conditioned Units (CRAC) will pass to the aisle tiles. Then the cold air will be picked up by the front of the server's rack by server fans and hot air will be pushed in the rear of the server racks. Finally, the hot air from the server racks is cooled by the CRAC unit. The CRAC unit operates refrigerant evaporator coils to cool the hot air from the server [3]. However, this typical air-cooled method struggles to keep up with the present server rack heat density. Modern high-power computer servers can emit up to 40kW heat per rack [4]. The air-cooled methods are not so efficient and generate hot spots which result in server down time.

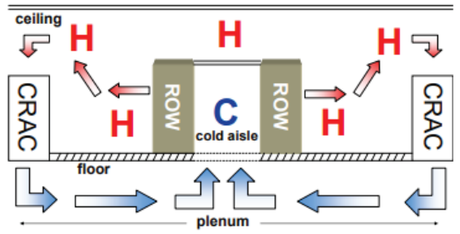

Figure 1 Hot Aisle Containment Cooling in Data Centres[2].

A recent study by the Uptime Institute stated that the average rack server heat density is increasing at a tremendous rate. In 2017, 5.6 kW per rack server heat density went up to 8.4 in 2020 and this growth is expected to go up to 12 kW per rack by 2025 [1]. Over the decades, there have been many metric systems introduced for the data centres. Jamz et al., presented more than 30 metrics systems for measuring energy efficiency of the data centres [5]. Even though there are many metrics systems introduced in the community, most common industrial metric is the PUE system introduced in 2006 by Malone and Belady [6]. The PUE energy metrics is calculated by dividing the total (IT + IT Cooling) energy into a data centre with energy used by IT equipment. In 2020 the uptime institute reported that the current average PUE of data centres is around 1.59. The aim of this research is to improve the energy efficiency of the current cooling systems in data centres to cool high heat density servers by a water-cooled experimental technique. This paper will discuss thermal, energy, cost saving and carbon emissions reduction by using the water-cooled server racks. Figure 2 illustrates the average IT heat load density increase over the years in data centre.

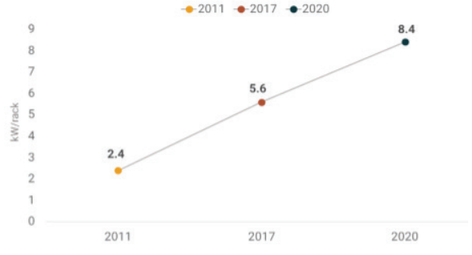

Figure 2 Uptime Institute Report (2020) data on IT heat density increase per rack in data centres [1].

Experimental Method

Analytical heat transfer and thermodynamic calculations were used to design and build a testing rig. A heat exchanger is placed in the rear door of the server cabinet along with fans. A sophisticated PLC programmed control logic is established to control the cabinet server temperature by adjusting fan and water flow rates and controlling condensation. Along with this, the PLC is also programmed to provide all the data to evaluate the thermal and energy performance of the unit. The test rig was built to represent the data centre room environment outlined by the ASHRAE [1].

Total twelve server heat dummies used along with the twelve temperature probes. Each dummy server has a maximum IT load heat capacity of 3.5kWh. Five temperature probes were evenly spread across the front of the heat exchanger to monitor the temperature rise in the server cabinet. The programme then averages these five temperature results and used the value as server setpoint reference. Server dummies were spread across the 42U height in the cabinet (U = 'U' refers to the standard to measure the vertical space in the data server racks, 1U = 1.75 inches.), the remaining gaps were covered with the blanking panels. The fluctuation of this server rack temperature is influenced by the fan speed, which, in turn, determines the energy consumption. The fan speed is controlled by a PID controller. However, it operates in the logic of the integral time setting, where the system will monitor the server temperature set point and decide whether a necessary increase or decrease of the fan speed is needed or not to achieve the server set point. The experimental results were gathered over 6 hours period. Figure 3 illustrates the schematic diagram of the test rig.

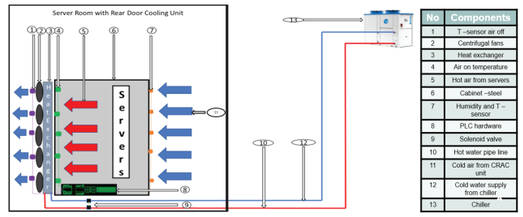

Figure 3 Schematic Diagram of the Test Rig.

Results and Discussion

This server average temperature is set to be at 47°C at 40 kWh load. The figure below shows that the server rack successfully maintains the temperature around 47°C. At 18°C water inlet temperature, the cabinet discharge temperature was around 26°C and whereas at 14°C, it was around 25°C. The ASHRAE limit suggests that server room temperature can be maintained up to 27°C. The results obtained from this prototype have illustrated that the 40 kW rack can be maintained in the server room under the recommended maximum temperature limit.

However, as water is considered unsafe for electronics, the prototype was built to avoid condensation in the unit. Figure 4 shows that the dewpoint temperature of the cabinet is always below the water inlet temperature which ensures no condensation in the rack. The average server temperature and dew point stayed stable at various water inlet temperatures. This is because the dew point is calculated by the relative humidity of the rack inlet and room temperature.

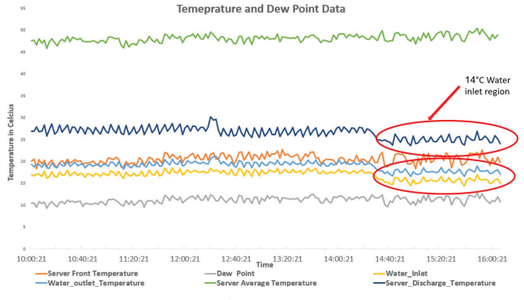

Figure 4 Temperature and Condensation control for various water inlet temperatures.

In addition to rack thermal analysis, total energy consumption metrics and cost saving analysis were conducted in this study. For this current study, two different test conditions of 14°C and 18°C water inlet temperature were chosen to analyse the effect on PUE results. The experimental results from the test rig suggested this water-cooled system to be more energy efficient (PUE 1.42) than the conventional hot and cold aisle CRAC cooling methods (PUE 1.59). Results also show that increasing the water inlet temperature from 14°C to 18°C will have carbon emission reduction and cost saving without compromising the server cabinet thermal performance. Table 1 represents the data obtained from both 14°C and 18°C water inlet results along with PUE values. The calculations are done by assuming free cooling chillers are available in the system.

Table 1 Energy Efficiency Comparison Table.

Metric and Cost Per Year	Value
PUE - Air Cooled	1.59
PUE - Water Cooled at14°C	1.49
PUE - Water Cooled at 18°C	1.42
Traditional Air-cooled Data Centre Running Cost (PUE 1.59)	£83,439 per year
Cost Saving between Air cooled and Water Cooled at 14°C	£78,183 saving £5,256 per year
Cost Saving between Air cooled and Water Cooled at 18°C	£74,635 saving £8,804 per year
Reduction in Carbon Emission between Air Cooled and Water Cooled at 14°C	22 Tons per year
Reduction in Carbon Emission between Air Cooled and Water Cooled at 18°C	36 Tons per year

Conclusions

The ambition of this experiment is to establish a working methodology to reduce the energy consumption in the data centre using water-cooled methods. This is achieved in this study by adding the rear door heat exchanger into the existing server rack. By evaluating the thermal data and energy efficiency data from the prototype, water cooled racks can be the way to lead the data centre industry into their future energy efficiency goals. Along with that, the study indicated that, increasing the water inlet temperature from 14°C to 18°C, increases the energy efficiency without compromising the cabinet thermal performance.

References

[1] Rhonada.A, and Lawrence. A, 'Uptime Institute global data centre survey 2020' UI intelligence report 38, UII-38,p. 2-32,2020.

[2] John.N, Victor.A and Brown.K,' Hot-aisle vs Cold-Aisle containment for data centres', white paper by APC Schneider Electric, no.135,p.3,2010.

[3] Geng. H, 'Data center handbook', John Wiley & Sons, 2014.

[4] National Renewable Energy Laboratory (NREL). U.S. department of energy. High-performance computing data centre: Accessed:07/05/2021.Website: https://www.nrel.gov/docs/fy12osti/55423.pdf.

[5] Jamalzadeh.M, and Behravan. N, 'An exhaustive framework for better data centers' energy efficiency and greenness by using metrics' Indian Journal of Computer Science and Engineering, no. 2(6), p. 813-822, 2012.

[6] Malone.C, and Belady.C, 'Metrics to characterize data centre & IT equipment energy use', in Proceedings of the Digital Power Forum, Richardson, TX. 2006.

Development of Nitriding Process Using State-of-The-Art HIPIMS Technology

Krishnanand Shukla [a,†], Yashodhan Purandare [a], Imran Khan [b] Papken Hovsepian [a]

[a] Materials and Engineering Research Institute, Sheffield Hallam University, Sheffield, S1 1WB
[b] Zimmer-Biomet UK Limited, Dorcan Industrial Estate, Swindon, United Kingdom

Abstract

CoCrMo alloys were plasma nitrided using both HIPIMS and DC discharge to compare the quality and productivity of the process. In this work, phase and layer composition, hardness, tribological and corrosion resistance of both samples have been investigated. Results revealed that the HIPIMS develops a mix nitrided layer (Co_4N + Co_4N-$Co_{2-3}N$) two times thicker than that of DC plasma nitrided (DCPN) (only Co_4N-$Co_{2-3}N$). Based on surface hardness analysis HIPIMS plasma nitrided (HPN) showed significant increase in hardness value (23 GPa) as compared to DCPN (20 GPa) and the untreated one (~8 GPa). Surprisingly, both specimens showed similar tribological properties. However, HPN showed superior corrosion resistance (i_{Corr}= 10_{-5} mA) as compared to DCPN, 10^{-4} mA.

Introduction

CoCrMo alloys have been utilised to develop total replacements such as Hip and Knee due to its high hardness and load bearing capacity. However, due to high amount of Co present in the matrix which is around 60 at. % makes this alloy unsuitable in long term use. Co metal ions consider to be poisonous and if released in the human body can develop carcinogenic effect. To minimize the metal ion release from the CoCrMo alloy various surface modification approach have adopted by various researchers such as low-temperature plasma nitriding, ion implantation and ceramic coatings like CrN/NbN [1]. These coatings proven to minimize the releases of such metal ions significantly and have shown superior corrosion and wear resistance. At the same time plasma nitriding provides improved fatigue and tribological properties. Unfortunately, plasma nitriding requires longer process time to obtain the desired thickness in low-temperature condition (<450° C). Recently, K. Shukla and co-workers presented that the high thickness of nitrided layer (> 4 µm in 4 hours) can be achieved by utilizing HIPIMS discharge under low pressure (8×10^{-3} mbar) and temperature condition (400° C). Further this study shows that layer composition can be varied from pure S phase (Co_4N or γ_N phase also known as expanded austenite) to compound layer (Co_4N+$Co_{2-3}N$) [2].

Later in the same year K. Shukla and co-workers found that the change in phase composition directly influences the toughness and fracture toughness of the CoCrMo alloy. Also, the crack initiation and propagation during static loading varies with change in nitriding voltage. Similar behaviour was also observed in the case of dynamic loading where the depth of the crater reduces with change in nitriding voltage from -700 V to -1100 V. The surface analysis of these crater shows that the oxidation behaviour of the surface and sub-surface cracking also affected due to the phase composition of the nitrided layer. Lower the nitriding voltage (-700 V to -900 V) showed better performance than those treated at higher voltage [3].

Recently, K. Shukla and co-workers found that the corrosion resistance and passivation behaviour of the HIPIMS nitrided CoCrMo alloy changes with the surface microstructure and layer composition. A layer with mixture of Co_4N+$Co_{2-3}N$ and 43:56 texture showed superior corrosion behaviour with much reduce corrosion current (i_{Corr}:10^{-5} mA) in simulated body fluid environment. The reason behind shift in corrosion potential and reduce current was found to be right combination of γ_N and ε_N phase. However, it was found that the γ_N phase partially dissolves during the corrosion tests whereas dissolution of ε_N phase changes with change in nitriding voltage. At higher bias voltage the some of the grains dissolves completely leaving layer like structures. Further analysis of the exposed surface showed that the pitting within the grain is one of the reasons for higher corrosion current for samples nitrided at higher nitriding voltage [4].

In this current study, HPN specimens were compared with DCPN to evaluate the process quality.

Experimental Method

Pre-polished CoCrMo alloy were obtained from Zimmer-Biomet UK to perform HPN and DCPN experiment using Industrial sized PVD machine (Hauzer Techno Coat 1000/4) and commercial DC plasma nitriding machine. Before experiment samples were cleaned and vacuum dried to remove organic contaminants from the surface. Experiment parameters are presented in table 1.

	HPN	DCPN
Temperature (°C)	400	405
Power (kW)	1-2	1
Rotation	3-fold	none
Pre-treatment Time (Hours)	0.5	3
Total Process time (Hours)	4	21
Pressure (mbar)	8×10^{-3}	5×10^{-2}

Table 1: HIPIMS PN and DCPN parameters.

Characterisations:

Phase Composition	Glancing angle XRD (2°) (Empyrean Cu kα)
Layer composition	Cross-section SEM (NOVA)
	SIMS
Nanohardness	CSM nanoindentation (5 mN applied load)
Tribology	CSM Pin-on-Disc tribometer
Corrosion analysis	In Hank's solution (ph= 7.2)

Table 2: Type of characterisation performed on HPN and DCPN.

Results and Discussion

X-ray diffraction analysis of nitrided specimens confirmed that the formation of nitrided layer. HPN found to have a mixture of both γ_N(111) and γ_N(200) phase with combination of 43:57 whereas this combination for DCPN found to be ~91 % γ_N(111) with small contribution from Cr_2N phase. Later this was confirmed by cross-sectional SEM analysis. The nitrided layer formed for HLPN had two distinct interfaces (diffusion, Co_4N and compound, Co_4N+$Co_{2-3}N$). In the case of DCPN this combination was limited to Co_4N+$Co_{2-3}N$ (absence of diffusion layer) shown in figure 1. Also, layer thickness measured for HPN was found around 2.8 µm which was twice thicker than that of DCPN.

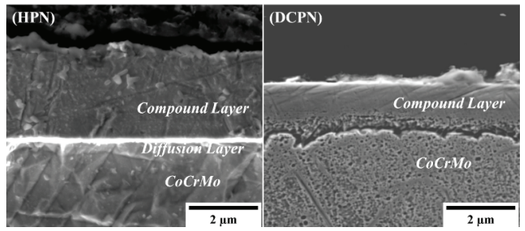

Figure 1: SEM micrograph of HPN and DCPN.

SIMS analysis revealed that the HPN contains more nitrogen almost twice the value recorded for DCPN up to the control depth of 1.5 µm (figure 2).

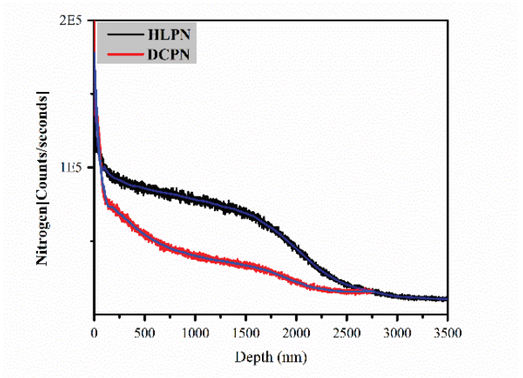

Figure 2: SIMS N2 depth spectra of HPN and DCPN.

Both nitrided specimen showed reduced µ (0.6-0.62) and improved wear resistance (Kc) value despite significant difference in thickness and phase composition. On the other hand, highest K_{Ic} value of 950 $MPamm^{1/2}$ was measured for HPN as compared to DCPN (917 $MPamm^{1/2}$) and the untreated specimen (900 $MPamm^{1/2}$).

Potentiodynamic polarisation study performed in Hank's (simulated body fluid) solution showed that the nitrided formed on HPN reduces corrosion current (i_{Corr}=5×10^{-5} mA) significantly when compared to the untreated (i_{Corr}=2×10^{-3} mA) and DCPN (i_{Corr}=1×10^{-4} mA).

Further analysis of hank's using Inductive coupled plasma mass spectrometry confirmed that the HPN treatment is more prone to minimise the release of metal ions (Co: 0.3; Cr: 0.6; Mo: 0.1) than that of DCPN (Co: 0.1; Cr: 1.6; Mo: 0.2) and untreated (Co: 0.7; Cr: 2.2; Mo: 1.3).

Conclusions

The nitriding rate of HIPIMS low pressure plasma nitriding (HLPN) was found to be factor of 4 higher than that of the industry standard DCPN treatment used as a benchmark.

Compared to DCPN, HLPN allows almost factor of two higher nitrogen concentration in the nitrided layer to be achieved at a control depth of 1.5 µm.

HLPN produced nitrided layers show higher hardness, (Hp= 23 GPa) and higher wear resistance, (lower wear coefficient Kc= 1.18 × 10-15 $m^3N^{-1}m^{-1}$) as compared to DC PN process.

The obtained high H/E and H3/E2 values are indicative of the high fracture toughness of the nitrided layers produced by the utilisation of the novel HLPN technology.

With higher corrosion potential, Ec= 160 mV and higher pitting potential, Up = 770 mV the HLPN layers showed a superior corrosion performance in Hank's solution providing reliable corrosion protection of the untreated CoCrMo (F75) alloy.

The enhanced mechanical and corrosion resistance properties and favourable Me-ion release performance combined with the significant enhancement in process productivity makes the HIPIMS enhanced plasma nitriding a powerful technique for surface treatment of medical-grade CoCrMo alloys.

References

[1] **P. Eh. Hovsepian et al.,** Development of superlattice CrN/NbN coatings for joint replacements deposited by high power impulse magnetron sputtering. J. Materials Science: Materials in Medicine, (2016) 27:147. DOI 10.1007/s10856-016-5751.

[2] **K. Shukla et al.,** "Low-pressure plasma nitrided CoCrMo alloy utilising HIPIMS discharge for biomedical applications," *J. Mech. Behav. Biomed. Mater.*, vol. 111, p. 104004, Nov. 2020, doi: 10.1016/j.jmbbm.2020.104004.

[3] **K. Shukla et al.,** "Effect of nitriding voltage on the impact load fatigue and fracture toughness behaviour of CoCrMo alloy nitrided utilising a HIPIMS discharge," *Surf. Coatings Technol.*, vol. 400, p. 126227, Oct. 2020, doi: 10.1016/j.surfcoat.2020.126227.

[4] **K. Shukla et al.,**" Correlation between the microstructure and corrosion performance of the HIPIMS nitrided bio-grade CoCrMo alloy", https://doi.org/10.1016/j.jallcom.2021.160429

Chromodynamic Multi-Component Lattice Boltzmann Method for Biomedical Applications

J. Spendlove [a,†], X. Xu[a,b] T. Schenkel[a,b] and I. Halliday [c]

[a] Materials and Engineering Research Institute, Sheffield Hallam University, Sheffield, S1 1WB
[b] Department of Engineering and Mathematics, Sheffield Hallam University, Sheffield, S1 1WB
[c] Department of Infection, Immunity and Cardiovascular Disease, The Medical School, University of Sheffield, Sheffield, S10 2RX

Abstract

This work discusses the recently developed single framework three-dimensional chromodynamic multi-component lattice Boltzmann method for simulating vesicle hydrodynamics. The novelty of this work is a new model which has applications within the biomedical field, where a more transparent, accurate approach to simulating vesicles (such as red blood cells) would be advantageous. The benefits of the developed method are its: (i) single framework approach (making it transparent); (ii) capability for scaling to the simulation of many vesicles; (iii) robustness in that its stable and accurate far from mechanical equilibrium; (iv) applicability; it is not restricted to specific flow regimes i.e., Stokes flow. Following on from its development, this short work briefly outlines the method and discusses future directions for this work, which are split into three parts (a) Computational advancement – *improving model computational efficiency* (b) Theoretical advancement - *furthering the understanding of parameters leading to a minimal but more accurate model for simulating RBCs* (c) Application - *the simulation of biological flows involving single RBCs, such as in narrow passages within the body*.

Introduction

The simulation of fluid-filled vesicles (i.e., red blood cells (RBCs)) has obvious applications within biomedical science. The model one uses must be computationally capable of simulating time and length scales characteristic of that of the desired application, currently, the simulation of human RBCs. Mesoscale simulation methods, such as lattice Boltzmann method (LBM), provide an attractive option for simulating RBCs due to their computational efficiency, appropriate length and time scales, capability to include physics that is characteristic of smaller length scales and also the ability to interface with the continuum description of fluids. Current, more mature, mesoscale approaches using single component LBM (SCLBM) for modelling fluid and a separate modelling approach for the deformable body, either focus on scalability to dense suspensions with fading accuracy, the simulation of single vesicles with high accuracy, or aim to tackle both but are encapsulated in more complex multi-framework approaches. The model presented in [1] is a single framework approach (in that it uses only one modelling technique) which is transparent, robust and has the future ability to be scaled to the simulation of many vesicles using previous methodologies [2].

Methodology Overview

The developed chromodynamic multi-component lattice Boltzmann method (cMCLBM) is a single framework approach, that treats the exterior as one fluid (Blue), the interior of the vesicle as another fluid (Red) and the interface between the two as a quasi-diffused interface where a central contour is taken to represent vesicle surface (see Figure 1 for a schematic highlighting this).

Akin to that of SCLBM, fluid is simulated by tracking the time evolution of fictitious particle distributions over a Eulerian lattice using a distribution function f , where i is the lattice link index. For two component cMCLBM, the distribution function is split for the two fluids $f_i=R_i+B_i$, denoted Red (R_i) and Blue (B_i). Macroscopic fluid quantities, density and velocity, are computed locally at lattice sites by utilising simple lattice properties. In order to enforce behaviour consistent with vesicles such as RBCs, immersed boundary forces are applied in the interfacial region which are derived from vesicle physics (e.g., area conservation) and known boundary physics (e.g., surface tension). The three immersed boundary force contributions for this work are the: area conserving $\underline{f}^{(a)}$, surface tension $\underline{f}^{(l)}$ and bending rigidity $\underline{f}^{(b)}$ forces [1],[3]:

$$\underline{F}^{(a)} = \alpha H \left(A - A_0 \right) A \hat{n},$$

$$\underline{F}^{(l)} = 2 \sigma H \hat{n},$$

$$\underline{F}^{(b)} = -\kappa_B \left(\frac{3}{2} \Delta_s H + H^3 - KH \right) \hat{n},$$

References [1],[2] and [3] provide further explanation of the methodology and above equations.

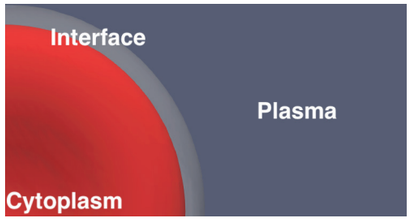

Figure 1: Schematic of two-component cMCLBM fluid definitions with relation to colour. Cytoplasm is one fluid (Red), Plasma another (Blue) and the interfacial region (Grey).

Results

Here, steady state and dynamical data from the model, focusing on the simulation of the biologically significant bicuspid vesicle, will be presented. Due to length restrictions, minimal explanation is attached to these other than within the caption (please see references for a more detailed understanding of the data/ tests).

Figure. 2 panel (A) shows a steady state bicuspid vesicle produced by the method – showing the method qualitatively meets the steady state zero flow requirements of desired RBC vesicle profile (with further quantification of accurate profile in [1]). Figure. 2 panel (B) shows the result of the vesicle in (A) being sheared in opposing directions (highlighted by the arrows) - where the data from such shears has been compared favourably against experimental data of [4] in [1].

Figure. 3 shows the time evolution of a single vesicle pushed parallel to its axis of rotation down a passage with a square cross-section from two different views (A) and (B). Note, this result is not representative of that of in passages in the human body, due to square cross-section and also the boundary conditions applied in simulation. The data however in Figure. 3 is a test of model stability, showing appropriate and physically understandable deformation, with area of the vesicle being conserved throughout simulation. Providing a good conformation of stability under flow induced deformation.

Figure. 4 shows an interaction between two vesicles which are being pushed in opposing directions towards each other by an applied buoyancy force. The result shows that the simulation remained stable, even for quite a harsh collision with large stresses, and that the vesicles moved past each other as expected without coalescing.

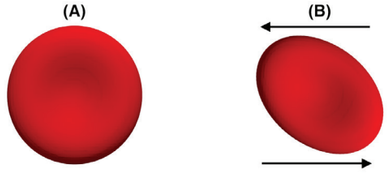

Figure 2: Views looking down the axis of rotation in relation to the vesicle in panel (A). (A) Steady state bicuspid profile. (B) Profile of a sheared bicuspid in opposing directions (highlighted by the arrows).

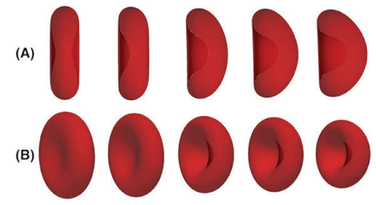

Figure 3: Data of increasing time evolution (left to right) of a single bicuspid vesicle being pushed by a buoyancy force parallel to the axis of rotation down a passage with a square cross-section. (A) shows a 2D view looking down an axis perpendicular to the direction the buoyancy force is being applied. (B) shows a 3D view of the vesicle evolution.

Figure 4: Data of two vesicles moving past each other in flow, where frames show increased time evolution left to right. Here, the red vesicle moves in the positive x direction, and green vesicle in the negative x direction due to an applied buoyancy force to the vesicles. View looking down the axis perpendicular to the axis of rotation in relation to the initial bicuspid vesicle shown in the far-left frame.

Discussion and Future Direction

Simulation data from the model has been displayed and briefly explained, with the presented data focused around the biologically significant bicuspid vesicle which is representative of that of a human RBC. The data highlighted the bicuspid vesicle: (a) in steady state within zero physical flow; (b) under flow induced deformation; (c) interacting with another vesicle. Work in [1] encapsulates the development and analysis of the method in much more thorough detail, including comparison of the models in-silico data from the shear test in Figure. 2 panel (B) with experimental data, as well as further quantitative review of vesicle shape. Through this validation, this work introduces a new model for simulating three dimensional bicuspid vesicles, that is encapsulated in a single framework, transparent, accurate and robust methodology - providing a novel contribution to the field.

Future directions for this work can be split into three main areas:

(a) Computational advancement: looking at code-based improvements to make the model more efficient, an essential requirement when looking at extending to the simulation of many vesicles where computational cost will increase.

(b) Theoretical advancement of the method: looking at further tailoring the model towards biological applications through surveying the parameter space to find the most appropriate parameterisation for simulations aiming to replicate human RBC behaviour. This may include examining the impact of using non-zero preferred curvature values within the membrane bending force.

(c) Application of the current method: seeking areas where the simulation of a single RBC within flow is of interest. For instance, looking at a single RBC flowing in a small slit between endothelial cells [5] or asymmetric RBC profiles which have been seen in symmetric passages when studying blood microcirculation [6].

References

[1] J. Spendlove, X. Xu, T. Schenkel, M. Seaton, I. Halliday and J. Gunn. ‘Three-dimensional single framework multi-component lattice Boltzmann equation method for vesicle hydrodynamics’, *under review at Physics of Fluids*

[2] T. Spencer, I. Halliday and, C. Care, ‘A local lattice Boltzmann method for multiple immiscible fluids and dense suspensions of drops’’, In: *Philosophical transactions. Series A, Mathematical, physical, and engineering sciences* 369 (June 2011), pp. 2255–63.

[3] A. Guckenberger, S. Gekle, 'Theory and algorithms to compute helfrich bending forces: a review',Journal of Physics: Condensed Matter,29(20), 30, (2017)

[4] W. Yao, Z. Wen, Z. Yan, D. Sun, W. Ka, L. Xie, et al. 'Low viscosity Ektacytometry and its validation tested by flow chamber'. J. Biomech. 34, 1501–1509. doi: 10.1016/S0021-9290(01)00109-9. (2001)

[5] J. Freund, 'The flow of red blood cells through a narrow spleen-like slit’, Phys. Fluids 25, 110807 (2013)

[6] T.W. Secomb, R. Skalak,‘ A two-dimensional model for capillary flow of an asymmetric cell’, Microvascular Research, Volume 24, Issue 2, 1982, Pages 194-203

On the Control of Emissions from Intermediate Level Radioactive Waste Melting

A.H. Stone [a,†], P.A. Bingham [a], A. Holloway [a], A. Nabok [a], D. McKendrick [b], S. Morgan [c]

[a] Materials and Engineering Research Institute, Sheffield Hallam University, Sheffield, S1 1WB
[b] National Nuclear Laboratory, Sellafield, CA20 1PG
[c] Sellafield Ltd, Sellafield, Cumbria CA20 1PG

Abstract

This project aims to control and understand the vaporisation of radionuclides and other pollutants from the vitrification of intermediate level radioactive wastes (ILWs) and develop a real-time gas analysis system to collect data. A test rig has been developed to enable understanding of the evaporation mechanics from waste glass melts and waste compositions have been formulated to simulate ILW waste streams from UK nuclear sites representative of simulant 'site Ion exchange effluent plant' (SIXEP) sand/clinoptilolite, Magnox sludge and plutonium contaminated material (PCM). To date, simulant glasses have been run with XRD, XRF and TG-MS and are soon to be trialled on the completed off-gas system.

Introduction

Managing radioactive waste presents potential issues with leaching and environmental contamination whilst storing and treating. This is especially pertinent when considering intermediate level waste (ILW) which (in the UK) is a heterogenous mix of materials which do not generate heat but do exceed 12 GBq of beta/gamma activity[1]. Currently ILW in the UK is stored in steel drums or man-made ponds which can be wet or dry[2] however this is not a long term solution as the casings of these ponds could crack and leak, and the drums could corrode. The waste in question needs in some cases thousands of years to radioactively decay to a safe level3 and therefore we must consider a waste management technique that retains the contaminants for these long periods of time. One such technique is vitrification4 which uses high temperatures and additives to form a glass of the waste. Some glasses are known to exist for thousands of years without corroding or undergoing significant chemical degradation which makes it a good material for containing radionuclides. High level waste in the UK is already treated by this method and vitrification is also being considered for ILW although there are challenges given the heterogeneity of the materials.

Figure 1 ILW drums (plutonium contaminated material) in storage at Sellafield

One main concern with vitrification is the high temperatures the waste material must be exposed to which could vaporise some of the components and expose the environment to toxic, radioactive or greenhouse gases if released. A step towards understanding these emissions is to quantify and monitor them. Currently this is done by filtration where the components are captured on a filter and analysed after the run has cooled. This has problems because the monitoring is not in real time and any volatile components with a lower boiling point could pass through the filters. Another way of capturing these toxic gases would be to use capture solutions which absorb the gases by bubbling the fumes through. On a large scale would be difficult to implement, however for investigations in the lab this is possible. This technique is a reliable way to capture certain gases and has been used by the environmental monitoring industry for years[5] so can be adapted in the lab to understand gaseous emissions. However, this only gives a total emitted gas so emissions will be averaged over the whole period.

Another technique would be to install a real time analysis system which can analyse the gases as they are being produced. This would be the preferred method as monitoring is completed as the gas is produced and any variations in emissions during melting of the waste can be recorded.

Experimental Methods

Glass-making raw materials are added to waste materials, either as batch or in its raw form (i.e. wood, cement, steel). These are then heated in a furnace to process temperatures that are likely to produce a glass (generally around 1150 – 1400 °C) and then poured into a steel mould. The glass is subsequently annealed near the glass transition temperature of the material (usually 400-600°C).

For off-gas analysis the test rig has been set up to capture gas from a top loading furnace by passing the gas through a minimum of 4 x 250ml Drechsel glass impingers which contain solutions depending on the analyte (see Table 1). These can be changed mid melting to gain an insight of the times maximum emissions occur.

	Capture Solution			
Analyte	**1**	**2**	**3**	**4**
Cs, Na, Cr, other metals	0.53M HNO_3 + 0.44M H_2O_2	0.53M HNO_3 + 0.44M H_2O_2	Empty	Silica Gel
Halides (Cl,I,Br)	0.1M Sulphuric Acid	0.1M NaOH	Empty	Silica Gel
NOx, SOx	0.25M KMnO4	0.25M KMnO4	Empty	Silica Gel

Table 1 Capture solutions and sampling train for relevant analytes[5,6].

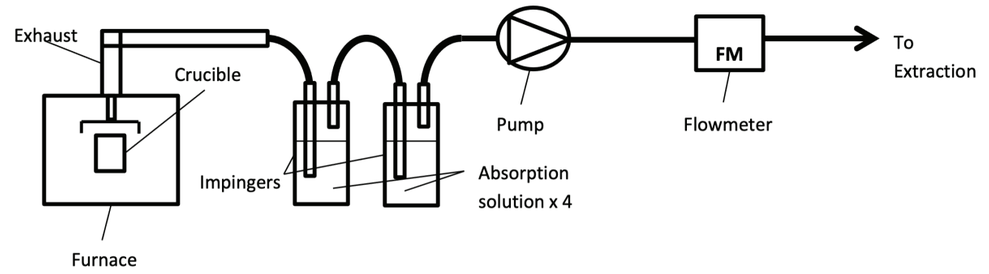

Figure 2 Diagram of the sampling train from furnace to pump

The Drechsel bottles are connected with Tygon tubing and kept in an ice bath to condense the analyte in solution. The tubing will then go to a flowmeter and suction applied at a known rate.

Analysis of solutions will be completed predominantly by inductively coupled plasma mass spectrometry (ICP-MS) for elemental breakdown of analytes however NOx and SOx will be analysed by spectrophotometer. Solid products (glass and particulate matter) will be analysed by X-Ray diffraction (XRD), X-Ray fluorescence (XRF) and Raman spectroscopy.

Results and Discussion

Batches for analysis have been prepared based on known commercial glasses and mixed with various wastes then processed in the furnaces at high temperature. Three ILWs have been considered in this study, Sand/Clinoptilolite, Magnox Sludge and Plutonium Contaminated Material (PCM): all common ILWs that occur in the UK. These have each been waste loaded into batch glass materials based on the following glasses: borosilicate, calcium aluminosilicate, Mixture Windscale (MW) and soda-lime-silica. These have been melted successfully and are shown to be amorphous by XRD with no crystallisation in the glass structure.

XRF has been completed for the base glasses and waste loaded glasses without Cs,Cl dopants. However, CeO_2, which was added as a uranium oxide surrogate, did show an average of 16% weight reduction in the Magnox sludge glasses which could represent a potential for toxic volatiles from uranium containing waste. The error with XRF measurement has been shown to be fairly high[7] especially within boron & lithium containing glasses so this could be within the range of error of the instrument.

Off-gas trials have begun with 1wt% and 2wt% Cs_2O doped final composition in Mixture Windscale (MW) type glass. These have been heated to 1150°C and held at temperature for 2 hours under a suction of 2L/min flowrate and will be analysed by ICP-MS. Chloride doped glasses were also attempted although blockages did occur during the test invalidating the run. After inspection of the equipment the tubing seemed in good condition so the blockage could have occurred due to expansion of particulates on the inside of the tube or liquid condensing in the tubing putting too much strain of the pump.

Conclusions

Waste loaded glasses have been successfully formulated and analysed ready for off-gas trials to be completed. Sand/clinoptilolite and Magnox sludge were investigated for their glass melting properties when added with glass forming agents. After some modification Mixture Windscale, borosilicate, calcium aluminosilicate and soda lime silicate XRD amorphous glasses were melted and poured with the waste additions of up to 77% waste loading sand/clinoptilolite mixtures or 15% waste loading Magnox sludge. XRF has shown losses of CeO_2, SiO_2 and Na_2O in all glasses.

Off-gas system trials have begun with basic MW type glasses with caesium and chloride additives using the impingement setup. These capture solutions are currently being analysed by ICP-MS. In addition, real time gas systems were selected for installation into the off-gas system, the most promising system being fibre enhanced Raman gas spectroscopy[8] which allows for unknown compounds to be measured and multiple analytes to be quantified at once. Other systems were considered such as Fourier transform infrared spectroscopy (FTIR), mass spectrometry and gas chromatography mass spectrometry (GCMS) but these were either too delicate to be placed in an industrial setting or did not measure a wide enough range of gases.

References

1. NDA. UK Radioactive Waste Inventory. Published online 2019. https://ukinventory.nda.gov.uk/?action=export_pdf&tid=90299adf9b76a9c0d448a1bbc39b1b6f&display_format=100&summary=Showing all unfiltered results.
2. Hyatt NC, Schwarz RR, Bingham PA, et al. Thermal treatment of simulant plutonium contaminated materials from the Sellafield site by vitrification in a blast-furnace slag. *J Nucl Mater*. 2014;444(1-3):186-199. doi:10.1016/j.jnucmat.2013.08.019
3. Caurant D. *Glasses, Glass-Ceramics and Ceramics for Immobilization of Highly Radioactive Nuclear Wastes*. Nova Science Publishers, Inc.; 2009.
4. Gin S, Jollivet P, Tribet M, Peuget S, Schuller S. Radionuclides containment in nuclear glasses: An overview. *Radiochim Acta*. 2017;105(11):927-959. doi:10.1515/ract-2016-2658
5. Environmental Agency. M2 Monitoring of stack emissions to air. *Environ Agency*. 2017;(August). https://assets.publishing.service.gov.uk/government/uploads/system/uploads/attachment_data/file/635235/LIT_6405.pdf
6. Levaggi DA, Zerrudo R, Karels G, Oyung W, Feldstein M. An Integrated Manual Impinger Method for The Simultaneous Determination of NOx and SOx in Source Effluents. *J Air Pollut Control Assoc*. 1976;26(8):783-786. doi:10.1080/00022470.1976.10470314
7. Rainer S. *X-Ray Fluorescence Analysis: Practical and Easy*.; 2002.
8. Hodgkinson J, Tatam RP. Optical gas sensing : a review. Published online 2013. doi:10.1088/0957-0233/24/1/012004

Activation foil neutron spectrum unfolding: algorithm and system design

O. Wong[a,b], R. Smith[a], C. R. Nobs[b], A. M. Bruce[c]

[a] Materials and Engineering Research Institute, Sheffield Hallam University, Sheffield, S1 1WB
[b] UK Atomic Energy Authority
[c] The University of Brighton

Abstract

Activation foil neutron spectrum unfolding has to be applied in future nuclear fusion reactors in order to monitor the neutron spectrum. However it is an ill-conditioned[1] mathematical problem and many different algorithms exist to perform this unfolding. Additionally, no previous study has attempted to optimize the selection of foils used in unfolding[2][3][4]. Hence, in this study we address these issues by creating an unfoldingsuite program which combines old and new algorithms written in a modern programming language, and developing a program which aids the optimization of foil selection.

Introduction

Typically neutron spectrum measurement is done through active methods, i.e. using detectors that relay measurements back to the experimenter in real time, such as Bonner Spheres detectors[6] or Single crystal Diamond Detectors (which can withstand up to pulses of up to 10^{14} neutrons in the Joint European Torus[5]).

However, in a high neutron flux, high temperature or strong magnetic field environment, such as the inside of a fusion reactor, these detectors cannot be deployed. For example, the next generation experimental fusion reactor, ITER, is expected to produce up to 10^{21} neutrons per second, far beyond the limit of diamond detectors. Instead, the inactive neutron spectrometry technique of activation foil neutron spectrum unfolding must be used[9]. This technique infers the neutron spectrum present by using the neutron spectrum of interest to activate foils of known compositions, measuring the radioactive isotope populations present in the foil, and then using these populations to infer the neutron spectrum. This avoids exposing any sensitive electronics to the harsh environment of the fusion reactor[3], at the cost of not being able to perform real-time measurement, and requiring a more complex experiment design.

The mathematics which performs the inference from radioisotope populations back to the neutron spectrum is complex, and no unfolding algorithm has been universally recognized as correct or adopted as the standard. Instead, a plethora of competing algorithms exists[10]. Some of these programs are written in outdated Fortran[7] which underperforms modern Python in terms of user-friendliness and readability; while others implement algorithms of limited mathematical rigor[8], leading to poorer unfolding accuracy.

Moreover, the accuracy of the inferred neutron spectrum is highly dependent on the choice of foils used. However, no systematic foil selection methods have been demonstrated in the literature for neutron spectrum unfolding to account for this critical dependency.[2][3][4]

To address the issues above, several more mathematically rigorous algorithms were designed and implemented as Python libraries. A foil selector tool was also developed to help with designing unfolding systems.

Algorithm design

To increase the accuracy of the unfolding algorithms, several new algorithms were derived. All of them start from an a priori (guess) spectrum input to reduce the dependence on experimental data and maximize accuracy.

One variant, known as the PseudoInverse algorithm, applies the Moore–Penrose inverse to modify the user-provided *a priori* spectrum into one which fits the measurement data. Two other variants, IMAXED and AMAXED, improve upon the renowned existing algorithm MAXED by recognizing that MAXED's loss function is convex. This allows Newton's method to be applied, leading to faster and more accurate convergence to the solution. The last variant, known as Regularization, applies the principle of Tikhonov Regularization[11] to perform unfolding.

To increase the ease of unfolding, the aforementioned algorithms, along with some of the more renowned unfolding algorithms (MAXED, GRAVEL, etc.), were implemented into the Python library "unfolding-suite". This was done to create a user-friendly interface with a more readable, modernized source code. Users of the unfolding-suite can input their experimental data to obtain the results for every unfolding algorithm, and compare them against each other, before selecting their desired result.

Using the unfolding-suite, the accuracy of each algorithm was tested using simulated data: provided with a list of *a priori* that differs from the true spectrum, the two traditional MAXED and GRAVEL gave unfolded spectra that have average cross-entropy = 0.0996 nat and 0.0806 nat respectively, where nat is the natural unit for information. A higher number of nats indicate a larger deviation from the desired distribution. Meanwhile most of the other novel algorithms (Regularization, PseudoInverse, and AMAXED) outperformed these traditional algorithms with average cross-entropy of 0.0328 nat, 0.0661 nat, and 0.0686 nat respectively. Only IMAXED underperformed MAXED and GRAVEL, with an average cross-entropy of 0.100 nat.

System design

The effectiveness of unfolding is limited by the number and variety of radioisotopes, and how easily they can be quantified. Currently, they are quantified by gamma spectroscopy using High Purity Germanium detectors (HPGe). This allows us to infer the number of radioisotopes present by measuring the brightness of characteristic gamma peaks emitted by the corresponding isotopes.

To perform gamma spectroscopy, the activity of the foil must be low enough that they do not saturate the detector beyond its operational limit, but still high enough to minimize the fractional error of each peak.

A foil selector tool program was created to rank the effectiveness of foils available; and generate the expected radioisotopes and therefore gamma spectra, of these foils. Users of this program can then select foils according to the supplier's availability and cost, and ease of handling the materials.

Experimental verification

An experiment was conducted using the ChipIr beamline in the ISIS neutron and muon source. A beam of high energy neutrons were used to irradiate a set of foils chosen with the aid of the foil selector tool. The resulting neutron spectrum will be unfolded using the activities of those foils, which were measured with a HPGe detector.

The foil was suspended in the irradiation area using a polyethylene bag in the setup shown in figure 1. The thickness of the bag (<50 gsm) was determined to be thin enough to have no observable effect on the neutron spectrum.

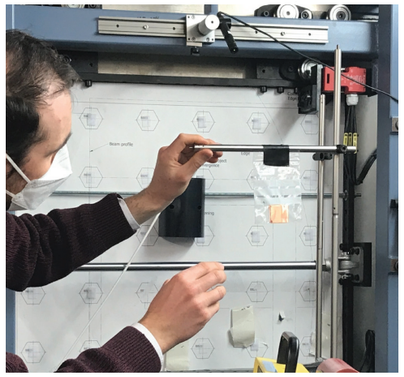

Figure 1 Foils are irradiated in the beamline, suspended in a thin polyethylene bag. The bag has minimal disturbance to the flux.

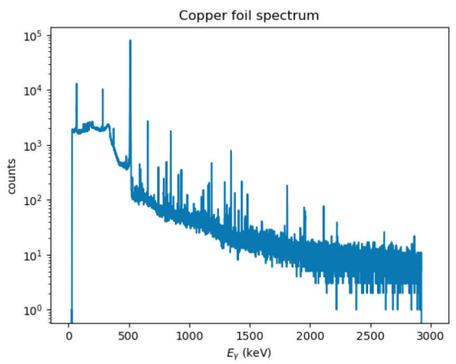

Figure 2 The gamma spectrum of the copper foil after irradiation. Each radioisotope's decay is associated with one or more peak on the spectrum

Conclusions

Activation foil neutron spectrum unfolding is a potentially promising tool for measuring the neutron spectrum in future fusion reactors. This research takes some of the necessary steps to maximize its efficiency and ease of use. This involved designing new algorithms, developing a program that implements those algorithms, and developing tools which aids the design of unfolding systems.

Four new algorithms named IMAXED, AMXED, PseudoInverse, and Regularization were derived. They are implemented as a python library "unfolding-suite" along with several popular existing unfolding algorithms; the benchmarking result shows that all of them, with the exception of IMAXED, outperformed the existing algorithms MAXED and GRAVEL.

A foil selector tool was created to aid the selection of foils so that future designers of unfolding systems can utilise it to pick out their list of foils. Its functionality was validated through our neutron spectrum unfolding experiment in the ChipIr neutron beamline, where it aided the foil selection process.

References

[1] Matzke, Manfred. "Propagation of uncertainties in unfolding procedures." Nuclear Instruments and Methods in Physics Research, vol. 476, 2002, pp. 230-241.

[2] Prasoon Raj, Steven C. Bradnam, Bethany Colling, Axel Klix, Mitja Majerle, Chantal R. Nobs, Lee W. Packer, Mario Pillon, and Milan Stefnik. Evaluation of the spectrum unfolding methodology for neutron activation system of fusion devices. Fusion Engineering and Design, 146:1272–1275, 2019.

[3] Bethany Colling, P. Batistoni, S.C. Bradnam, Z. Ghani, M.R. Gilbert, C.R. Nobs, L.W. Packer, M. Pillon, and S. Popovichev. Testing of tritium breeder blanket activation foil spectrometer during jet operations. Fusion Engineering and Design, 136:258–264, 2018.

[4] L.W. Packer, P. Batistoni, S.C. Bradnam, B. Colling, Sean Conroy, Z. Ghani, M.R. Gilbert, S. Jednorog, E Laszyńska, D Leichtle, et al. Activation of iter materials in jet: nuclear characterisation experiments for the long-term irradiation station. Nuclear Fusion, 58(9):096013, 2018.

[5] Pillon, M., et al. "Neutron detection at jet using artificial diamond detectors." Fusion Engineering and Design, vol. 82, no. 1, 2007, pp. 1174-1178.

[6] Thomas, D. J., and A. V. Alevra. "Bonner sphere spectrometers - critical review." Nuclear Instruments and Methods in Physics Research A, vol. 476, no. 1, 2002, pp. 12–20.

[7] M. Reginatto and P. Goldhagen. Maxed, a computer code for maximum entropy deconvolution of multisphere neutron spectrometer data. Health Phys., 77(5):579– 83, 1999.

[8] WN McElroy, S Berg, T Crockett, and RG Hawkins. A computer-automated iterative method for neutron flux spectra determination by foil activation. volume 1. a study of the iterative method. Technical report, ATOMICS INTERNATIONAL CANOGA PARK CA, 1967.

[9] Weller, Arthur. "Diagnostics for magnetic confinement fusion research." Nuclear Instruments and Methods in Physics Research A, vol. 623, no. 1, 2010, pp. 801–805.

[10] Jiří CVACHOVEC. Algorithms for processing experimental data from radiation measurements. PhD thesis, Masarykova univerzita, Fakulta informatiky, 2011.

[11] Hansen, Christian. "Numerical tools for analysis and solution of Fredholm integral equations of the first kind." Inverse Problems, vol. 8, no. 6, 1992, p. 849.

[12] Chiesa, Davide, et al. "Measurement of the neutron flux at spallation sources using multi-foil." Nuclear Inst. and Methods in Physics Research, A, vol. 902, no. 1, 2018, pp. 14–24.

Sheffield Hallam University | Materials and Engineering Research Institute

Sheffield Hallam University
Faculty of Science, Technology and Arts
Materials & Engineering Research Institute (MERI)
Howard Street
Sheffield S1 1WB UK

Tel: +44 (0)114 225 3500
Fax: +44 (0)114 225 3501
email: meri@shu.ac.uk

www.shu.ac.uk/meri